A direct measurement of the W decay width

August 2008

Troy William Vine
University College London

A thesis submitted to the University of London for the degree
of Doctor of Philosophy

I, Troy William Vine, confirm that the work presented in this thesis is
my own. Where information has been derived from other sources, I confirm
that this has been indicated in the thesis

UMI Number: U591350

UMI

Dissertation Publishing

ProQuest

Abstract

A direct measurement of the W boson total decay width is presented in proton-antiproton collisions at $\sqrt{s} = 1.96$ TeV using data collected by the CDF II detector. The measurement is made by fitting a simulated signal to the tail of the transverse mass distribution in the electron and muon decay channels. An integrated luminosity of 350 pb^{-1} is used, collected between February 2002 and August 2004. Combining the results from the separate decay channels gives the decay width as 2.038 ± 0.072 GeV in agreement with the theoretical prediction of 2.093 ± 0.002 GeV.

A system is presented for the management of detector calibrations using a relational database schema. A description of the implementation and monitoring of a procedure to provide general users with a simple interface to the complete set of calibrations is also given.

Acknowledgements

Contents

List of Figures

12

13

List of Tables

Chapter 1

Introduction

The theory describing the interactions of fundamental particles is the standard model. It is a quantum gauge field theory comprising the Glashow-Weinberg-Salam model [1, 2, 3] of electroweak (EWK) interactions, unifying the weak and electromagnetic interactions, and quantum chromodynamics (QCD) [4] describing the strong interaction. The electromagnetic force is carried by a massless photon, the weak force by massive W and Z particles, and the strong force by 8 massless gluons. Direct evidence for the gluon was first observed by the TASSO experiment using the PETRA accelerator at DESY in 1979 [5]. This was followed by the discovery of the W [6, 7] and Z [8, 9] bosons by the UA1 and UA2 experiments at CERN in 1983. This provided strong evidence in support of the standard model. The only subsequent experimental evidence indicating that the standard model is not complete is the observation of neutrino oscillation [10]. The unified electroweak theory predicts the existence of the Higgs field [11] to break the symmetry between the electromagnetic and weak interaction resulting in massive bosons for the weak interaction. The associated Higgs boson has not been directly

observed and is the next crucial test for the standard model. Since the standard model is only consistent with special relativity and not general relativity, it is not a complete theory of fundamental particles and does not include gravitational interactions.

Since the number of possible experimental measurements is greater than the number of free parameters, the standard model is an 'over-constrained' theory and precise experimental measurements provide stringent tests of the consistency of standard model predictions. One example, and the subject of this thesis, is the W boson decay width which is predicted at tree-level by the W boson mass and the Fermi constant, described in section 1.3.1. A high precision direct measurement of these quantities provides a crucial test of EWK predictions. Currently, the largest uncertainty on this constraint is due to the uncertainty on the W boson decay width measurement.

The distribution of virtual W bosons is sensitive to new physics. For example, the distribution of the W boson transverse mass, defined in equation 1.21, has been measured up to 950 GeV [12] at the Collider Detector at Fermilab (CDF) experiment, described in chapter 2. The agreement with the standard model prediction, shown in figure 1.1 together with the signal of a 800 GeV hypothetical W′ boson, excludes the existence of an additional boson with a mass below 800 GeV and the same decay channels as the W boson [13]. Additional decay channels for the W boson, such as an additional neutrino flavour, are not constrained by this test.

This thesis presents a precision measurement of the W boson decay width at the CDF experiment. This is compared with the standard model prediction of the W boson decay width, described in section 1.3.1, using the latest measurement

Figure 1.1: *The W boson transverse mass distribution (DATA) measured at CDF in* W → eν *decays, together with the prediction for an 800 GeV W′ boson (signal prediction) and the standard model background (background prediction) [13].*

of the W boson mass and the measured Fermi constant. Since the prediction of the decay width is insensitive to new physics, see section 1.3.1, this measurement provides a test of the consistency of the standard model.

This chapter describes the relevant theory for W and Z boson production in hadron collisions, and their subsequent decay.

1.1   Standard model

The standard model describes the interaction of structureless fermions, which have half-integer intrinsic angular momentum or 'spin', and their interaction via integer spin bosons.

1.1.1 Standard model particles

The propagation of a fermion field is described by the free Dirac equation, with Lagrangian

$$\mathcal{L}_{\text{Dirac}} = \overline{\psi}(i\gamma^{\mu}\partial_{\mu} - m)\psi \qquad (1.1)$$

where ψ are the Dirac spinors, which are four component column vectors, and m is the mass of the associated field quantum.

There are four independent solutions to the above equation, two with positive energy and two with negative energy. These are interpreted as particle and antiparticle components respectively, which are identical except the sign of the quantum numbers is reversed. Unless explicitly stated, antiparticles are implied in the following discussion. The Dirac spinors can also be decomposed into 'right handed' and 'left handed' components, which have positive and negative helicity respectively, where the helicity is the component of spin along the direction of motion.

The fermions undergo electromagnetic, weak and strong interactions due to an electric charge, a weak isospin charge and a colour charge respectively. This is described further below.

Only weak interactions can change the fermion type or 'flavour', and flavour changing interactions only occur between left-handed fermions. The fermions are therefore grouped into left-handed isospin doublets, with components that interchange under flavour changing weak interactions, and right-handed singlets. The lepton doublet consists of an electrically charged lepton with charge $q = -1$, and a neutral neutrino. The lepton has only one singlet, the right-handed charged lepton, since the right-handed neutrino cannot be observed (in the massless neu-

trino hypothesis). The electric and weak isospin charge are combined to create the weak hypercharge, described by the electroweak theory of the unified weak and electromagnetic interactions.

Three 'generations' of fermions exist, shown in table 1.1, with the leptons comprising the electron (e) with a mass of 0.511 MeV, the muon (μ) with a mass of 106 MeV and the tau lepton (τ) with mass 1.7 GeV and their associated neutrinos.

The three generations of quarks comprise up-type and down-type quarks with electric charge $+2/3$ and $-1/3$ respectively. Quarks additionally carry a colour charge, enabling QCD interactions described in section 1.1.3, and only the most massive quark, the top quark, is observed in an unbound state with mass 172.4 ± 1.4 GeV [14]. The other quark masses lie between the 1 MeV and 4.5 GeV.

$$\text{Leptons:} \quad \begin{pmatrix} \nu_e \\ e^- \end{pmatrix}_L, e_R^- \quad \begin{pmatrix} \nu_\mu \\ \mu^- \end{pmatrix}_L, \mu_R^- \quad \begin{pmatrix} \nu_\tau \\ \tau^- \end{pmatrix}_L, \tau_R^-$$

$$\text{Quarks:} \quad \begin{pmatrix} u \\ d \end{pmatrix}_L, u_R, d_R \quad \begin{pmatrix} c \\ s \end{pmatrix}_L, c_R, s_R \quad \begin{pmatrix} t \\ b \end{pmatrix}_L, t_R, b_R$$

Table 1.1: *Standard model fermions grouped into left-handed weak isospin doublets and right-handed weak isospin singlets.*

1.1.2   Quantum electrodynamics

The quantum field theory of electromagnetic interactions is quantum electrodymanics (QED) which describes the interaction of electrically charged fermions via the exchange of a photon [15]. As energy is not conserved at the photon vertex, the photon (γ^*) is 'virtual' and reabsorbed at a second vertex to conserve

energy overall. The momentum transfer is limited by the Heisenberg uncertainty principle.

As the phase of the fermion field is not observable, the field is required to be invariant under a local phase transformation, described by the U(1) symmetry group. This introduces a vector gauge field A_μ, whose associated quantum is the photon. The QED Lagrangian is

$$\mathcal{L}_{QED} = \overline{\psi}(i\gamma^\mu D_\mu - m)\psi - \frac{1}{4}F_{\mu\nu}F^{\mu\nu} \tag{1.2}$$

where the covariant derivative (D_μ) is given by

$$D_\mu = \partial_\mu - ie\,Q A_\mu \tag{1.3}$$

and eQ is the electric charge that couples to the photon field. The last term in the Lagrangian, the photon field tensor

$$F_{\mu\nu} = \partial_\nu A_\nu - \partial_\mu A_\mu \tag{1.4}$$

gives the photon field kinetic energy. A photon mass term is not allowed as it would break the gauge invariance.

1.1.3   Quantum chromodynamics

QCD, the quantum field theory of colour charge interactions [4], describes the interaction of quarks and gluons, which carry a colour charge. The colour charge exists in three possible 'colours', red, green and blue (antired, antigreen and antiblue for antiquarks). By requiring the quark field to be invariant under local

colour transformations, described by the SU(3) symmetry group, eight gluon vector fields G^a_μ are introduced, where $a = 1, ..., 8$. The eight gluons carry a colour charge which consists of a 'non-colourless' combination of a colour and an anticolour (the colour singlet $R\overline{R} + G\overline{G} + B\overline{B}$ is not allowed). The QCD Lagrangian is

$$\mathcal{L}_{QCD} = \overline{q}(i\gamma^\mu D_\mu - m)q - \frac{1}{4}G^a_{\mu\nu}G^{\mu\nu}_a \qquad (1.5)$$

where the covariant derivative (D_μ) is given by

$$D_\mu = \partial_\mu + ig_s T_a G^a_\mu \qquad (1.6)$$

and g_s is the gluon coupling strength to the colour charge and T_a are the eight matrix generators of the SU(3) group of colour transformations. Again local gauge invariance requires the gluons to be massless. The last term in the Lagrangian gives the gluon field kinetic energy and the gluon field tensor $G^a_{\mu\nu}$ is

$$G^a_{\mu\nu} = \partial_\mu G^a_\nu - \partial_\nu G^a_\mu - g_s f_{abc} G^b_\mu G^c_\nu \qquad (1.7)$$

where f_{abc} are the SU(3) group structure constants. The last term in the gluon field tensor is the result of the non-Abelian nature of SU(3) and represents gluon self-interactions.

1.1.4   Electroweak interaction

Weak interactions [15] consist of 'flavour changing' charged current (CC) interactions and neutral current (NC) interactions. The charged current interactions, mediated via the W boson, couple to the weak isospin doublet which has a weak

isospin charge of $T = 1/2$. The neutral current interactions, mediated via the Z boson, couple to both the weak isospin doublet and singlet. Since the singlet has $T = 0$, the neutral current is split into two components, one that couples to weak isospin and the other that couples to weak hypercharge $Y = 2(Q - T_3)$, where Q is the electric charge and T_3 is the third component of weak isospin. Hence the neutral current is a combination of weak and electromagnetic interactions.

The weak eigenstates (d′, s′, b′) of the quarks are linear combinations of the mass eigenstates (d, s, b) related by the Cabibbo-Kobayashi-Maskawa (CKM) matrix below.

$$
\begin{pmatrix} d' \\ s' \\ b' \end{pmatrix} = \begin{pmatrix} V_{ud} & V_{us} & V_{ub} \\ V_{cd} & V_{cs} & V_{cb} \\ V_{td} & V_{ts} & V_{tb} \end{pmatrix} \begin{pmatrix} d \\ s \\ b \end{pmatrix}
\tag{1.8}
$$

Experimental measurements of the matrix elements give diagonal elements close to unity and small off diagonal elements, resulting in 'Cabibbo' suppressed interactions between different quark generations. The CKM matrix is a unitary matrix in the standard model, with the constraints $\sum_i V_{ij} V_{ik}^* = \delta_{jk}$ and $\sum_j V_{ij} V_{kj}^* = \delta_{ik}$ where $\delta_{i(j)k}$ is the Kronecker delta.

Weak and electromagnetic interactions can be described together by the $SU(2)_L \otimes U(1)_Y$ symmetry group, where $SU(2)_L$ is the symmetry of left-handed weak isospin, and $U(1)_Y$ is the symmetry of weak hypercharge. The requirement of gauge invariance gives three vector gauge fields W_μ^i, where $i = 1, 2, 3$, and a single vector gauge field B_μ. The W_μ^i fields couple to weak isospin with strength g, and the B_μ field couples to weak hypercharge with strength g'. The covariant

derivative for left handed fermions is (for right-handed fermions $g = 0$ as $T = 0$)

$$D = \partial_\mu + ig\, T_i W^i_\mu + ig' \frac{Y}{2} B_\mu \tag{1.9}$$

where T_i are the matrix generators of the $SU(2)_L$ group of weak isospin transformations. The mass eigenstate fields, associated with the observed massive W and Z bosons, are mixtures of the W^i_μ and B_μ fields. The charged current fields are

$$W^\pm_\mu = \frac{1}{\sqrt{2}}(W^1_\mu \mp iW^2_\mu) \tag{1.10}$$

and the neutral current fields are

$$\begin{pmatrix} Z_\mu \\ A_\mu \end{pmatrix} = \begin{pmatrix} -sin\,\theta_W & \cos\,\theta_W \\ \cos\,\theta_W & \sin\,\theta_W \end{pmatrix} \begin{pmatrix} B_\mu \\ W^3_\mu \end{pmatrix} \tag{1.11}$$

where the Weinberg angle $\theta_W \approx 28°$ is found experimentally. The weak and electromagnetic coupling constants are related by

$$e = g\,\sin\,\theta_W = g'\,\cos\,\theta_W \tag{1.12}$$

since A_μ is the electromagnetic field.

The interaction terms of the Lagrangian for the charged current W^+_μ field (the interaction term for the W^-_μ field is the Hermitian conjugate) are

$$\mathcal{L}_{CC} = \frac{g}{2\sqrt{2}} W^+_\mu (\overline{q}_u \gamma^\mu (1 - \gamma_5) q_d + \overline{\nu}_l \gamma^\mu (1 - \gamma_5) l^-) \tag{1.13}$$

and the interaction terms of the Lagrangian for the neutral current are

$$\mathcal{L}_{NC} = eA_\mu \bar{\psi}\gamma^\mu Q\psi + \frac{g}{2\cos\theta_W} Z_\mu \bar{\psi}\gamma^\mu (g_V - g_A\gamma_5)\psi \qquad (1.14)$$

where the vector coupling $g_V = T_3 - 2Q\sin^2\theta_W$ and the axial-vector coupling $g_A = T_3$. As a result, neutral current interactions, such a fermion annihilation, have a Z boson and photon component. However, when the centre-of-mass energy is similar to the Z boson mass, a resonant condition occurs and the Z boson exchange dominates.

The weak vector bosons have observed masses, but mass terms of the form $\frac{1}{2}m^2 W^\mu W_\mu$ cannot be added to the Lagrangian, as it will break the Lorentz invariance. Instead, terms that preserve the SU(2) gauge symmetry are added. The 'spontaneous symmetry breaking' Higgs mechanism introduces a complex doublet of scalar fields ϕ that couple to the W^i_μ and B_μ fields. This adds a potential term $V(\phi) = \mu^2\phi^\dagger\phi - \lambda(\phi^\dagger\phi)^2$. By choosing $\mu^2, \lambda < 0$ there is a non-zero minimum at $|\phi| = \mu/\sqrt{2|\lambda|}$. Expanding about the minimum gives mass terms to the electroweak fields with

$$\frac{M_W}{M_Z} = \cos\theta_W \qquad (1.15)$$

and introduces the massive scalar Higgs boson. The mass of the Higgs boson is not predicted a priori by the theory, although its mass can be constrained from EWK measurements, particularly the mass of the W boson and top quark. The observation and direct mass measurement of the Higgs boson are the subject of continuing research.

28

1.1.5 Feynman diagrams

A scattering process can be expressed as a perturbative expansion of the Hamiltonian [16]. The terms in the expansion are multiplied by a power of the coupling constant α, referred to as the order. Each term may be represented by a Feynman diagram. In the Feynman diagram, incoming and outgoing lines represent fermions before and after scattering respectively. Internal lines and loops represent intermediate bosons, and boson radiation is represented by a boson line. Each vertex introduce a factor of $\sqrt{\alpha}$ in the matrix element, and hence a factor of α in the cross-section. Leading-order diagrams, such as W and Z boson production and decay shown in figure 1.2, contain two vertices and represent the first term of the perturbative expansion.
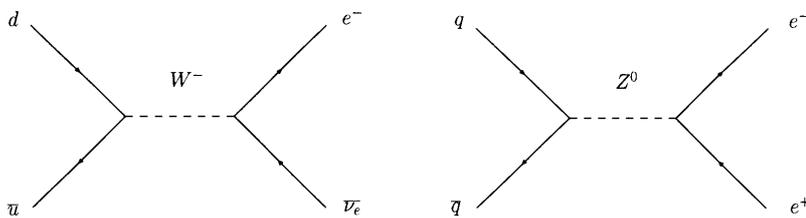
Figure 1.2: *Feynman diagram of leading-order boson production and decay.*

The additional perturbative terms provide corrections to the leading-order term, and become increasingly suppressed with higher-order.
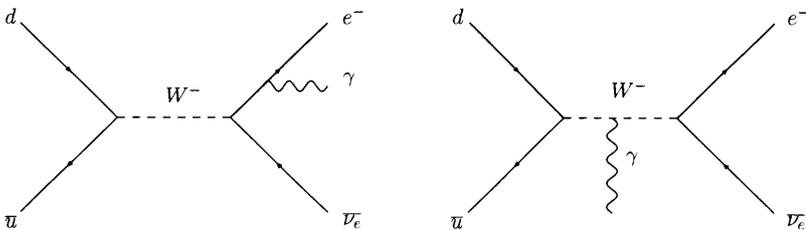
Figure 1.3: *Feynman diagram of W boson decay with a radiated photon.*

Radiative corrections, such as photon radiation from the boson or final state electron in W boson decay shown in figure 1.3, contribute additional particles to the final state. Virtual corrections, such as those shown in figure 1.4 for W and Z boson decay, do not contribute any additional final state particles.
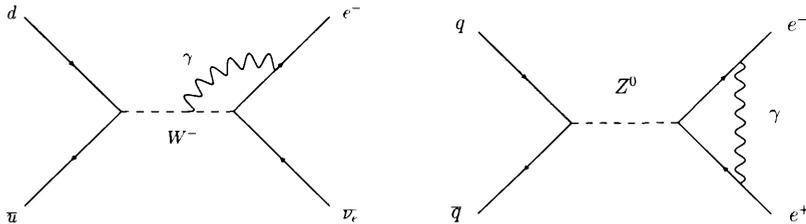
Figure 1.4: *Feynman diagram of boson decay with a virtual photon.*

Terms with an additional factor of α compared to leading-order terms, such as single photon radiation, are referred to as 'next-to-leading-order' (NLO) corrections. Similarly 'next-to-next-to-leading-order' (NNLO) corrections, such as two photon radiation, contain an additional factor of α compared to NLO.

1.1.6 Coupling

The measured coupling of a charge to its associated field is the sum of the perturbation series. As the sum of the series is divergent, the sum must have a scale-dependent cut-off. The 'renormalisation' of the Hamiltonian provides a measurable, scale-dependent coupling [16]. The coupling of QED interactions increases with the square of the momentum transfer (Q^2), while the coupling of QCD interactions (α_s) decreases with Q^2 due to gluon self-interactions. Quarks are therefore 'asymptotically free' at high energies and can be treated as free particles. At larger distances, α_s increases and quarks are confined into 'colourless' combinations of quarks, known as hadrons. Bound quarks may be quark-

antiquark pairs, which have a colour and anti-colour charge respectively (eg red and anti-red), or three quark combinations with have equal amounts of red, green and blue, such as a proton comprising the uud quark combination.

1.2 Drell-Yan process in hadron collisions

W and Z bosons are produced at hadron colliders by the Drell-Yan process where, at tree-level, individual constituents (partons) within the colliding hadrons annihilate to produce the boson. This parton model of 'hard' collisions is shown in figure 1.5 for the leading-order Drell-Yan W boson production at a proton-antiproton (pp̄) collider. The other 'spectator' partons, shown as double lines, form final state hadrons.
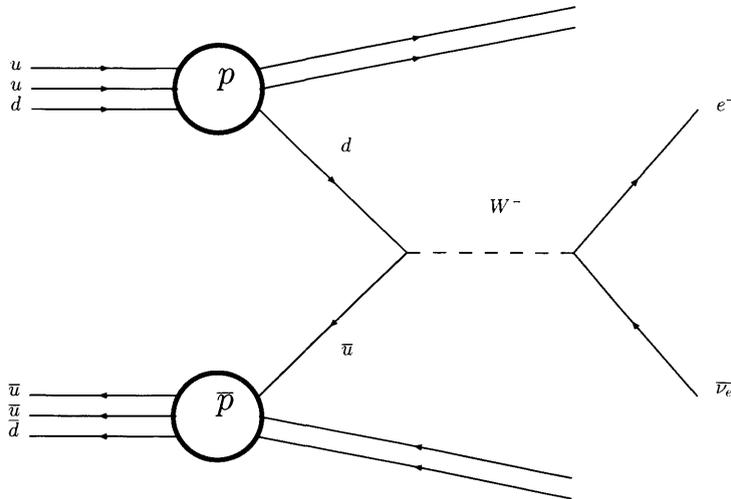
Figure 1.5: *Parton model of Drell-Yan W boson production.*

For a colliding proton and anti-proton with 4-momentum P_p and $P_\mathrm{\bar{p}}$ respectively, the Mandelstam variable $s \equiv (P_\mathrm{p} + P_\mathrm{\bar{p}})^2$ is Lorentz invariant and equal to the square of the centre-of-mass energy. Neglecting the proton rest mass, $s \approx 2P_\mathrm{p}\,P_\mathrm{\bar{p}}$.

31

The centre-of-mass energy of the two interacting partons ($\hat{s}$) is related to the $p\bar{p}$ centre-of-mass energy by $\hat{s} = x_1 x_2 s$, where $x_{1,2}$ are the momentum fractions carried by the two interacting partons. For leading-order boson production, the boson 4-momentum q is given by $q^2 = \hat{s}$.

The structure of the proton is described by the parton distribution functions (f_q) which satisfy

$$\sum^{\text{all partons}} \int_0^1 x f_q(x, Q^2) dx = 1 \qquad (1.16)$$

where Q is the scale. The parton distribution functions (PDFs) cannot be determined theoretically as the partons are in a bound state, and are measured experimentally using global fits to hadronic data [17]. The CTEQ6M PDFs corresponding to a scale $Q = m_W$ are shown in figure 1.6.
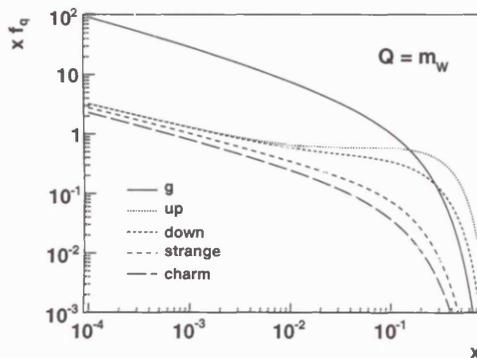
Figure 1.6: *The proton $x f_q$ distributions at $Q = m_W$ for the* CTEQ6M *PDFs.*

Since the Tevatron, described in section 2.2.1, has a centre-of-mass energy $\sqrt{s} = 1.96$ TeV, a W boson produced at rest with $q^2 = m_W^2$ results from both partons carrying momentum fraction $x \approx 0.04$. At this value of x, a considerable amount of the momentum is carried by the 'valence' quarks which make up the quantum numbers of the proton. At a hadron collider such as the Large Hadron Collider

32

(LHC), with a centre-of-mass energy $\sqrt{s} = 14$ TeV, the associated momentum fraction is $x \approx 5 \times 10^{-3}$ and the gluon is the most prevalent parton at this value of x.

In addition to $u\bar{d}$ interactions creating W^+ bosons (henceforth antiparticle equivalents will be implied), $c\bar{s}$, $u\bar{s}$ and $c\bar{d}$ interactions also occur, although with less frequency. This is because the charm and strange quarks have a lower probability density in the proton structure and $u\bar{s}$ and $c\bar{d}$ interactions are suppressed due to the small off diagonal elements of the CKM matrix. Gluon interactions, such as dg and gg shown in figure 1.7, also occur in W boson production although these interactions are suppressed due to the coupling of the additional gluon vertex.
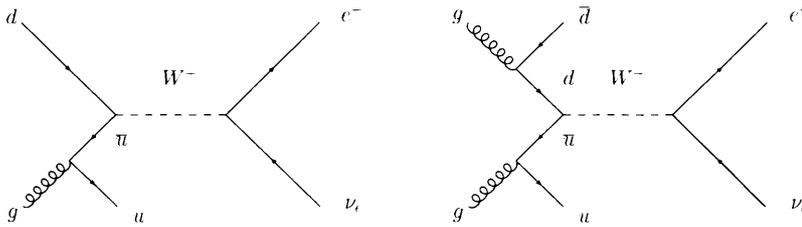
Figure 1.7: *Feynman diagram of W boson production from gluons.*

As the momentum fractions of the two partons are not necessarily equal, the boson can have a non-zero momentum component (p_z) in the proton direction. The rapidity (Y) of the boson is given by

$$Y = \frac{1}{2} \ln \frac{E + p_z}{E - p_z} \tag{1.17}$$

where E is the boson energy. The rapidity between two particles is invariant under a Lorentz transformation parallel to the proton direction. The parton

momentum fractions are related to the boson rapidity by

$$x_{1,2} = \sqrt{\frac{\hat{s}}{s}}\, e^{\pm Y} \tag{1.18}$$

shown in figure 1.8 for $\sqrt{\hat{s}} = m_W$ at the Tevatron. Events selected with a 'minimum bias' are produced uniformly in rapidity and are the most frequently occurring interactions at hadron colliders.
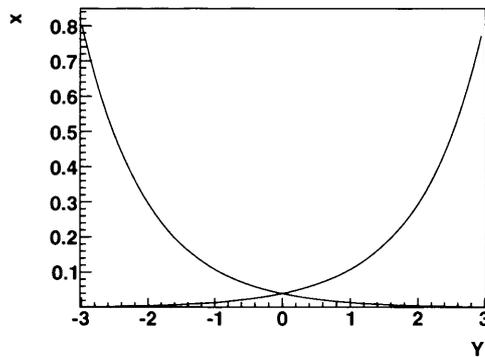
Figure 1.8: *Parton momentum fractions as a function of rapidity.*

For a massless particle, the rapidity is equal to the pseudorapidity (η) given by

$$\eta = -\ln\left(\tan\frac{\theta}{2}\right) \tag{1.19}$$

where θ is the angle between the particle and the proton direction.

The invariant mass of two particles produced by the decay of a massive particle is equal to the rest mass of the latter, given by $m = \sqrt{(P_a + P_b)^2}$ where $P_{a,b}$ is the 4-momentum of the decay products. This can be expressed as

$$m = \sqrt{(E_a + E_b)^2 - (\vec{p}_a + \vec{p}_b)^2} \tag{1.20}$$

34

where $E_{a,b}$ and $\vec{p}_{a,b}$ are the energy and momentum vector respectively of the final state particles a and b.

Although the Z boson's invariant mass is reconstructed at hadron colliders, this is not possible for W bosons as the neutrino, and hadron remnants at large rapidity, are not detected. Instead the transverse mass of the W boson is reconstructed. W bosons produced at rest in the detector decay with the charged lepton p_T equal and opposite to the neutrino p_T.

The boson mass in the transverse plane (m_T) is calculated from the transverse momentum $p_T = p \sin\theta$ of the decay products. From equation 1.20, the transverse mass of two particles with transverse momentum p_T^a and p_T^b and azimuthal angle $\Delta\phi$ between them is given by

$$m_T = \sqrt{2\, p_T^a\, p_T^b [1 - \cos(\Delta\phi)]} \qquad (1.21)$$

neglecting the rest mass of the final state particles.

Higher-order Drell-Yan production processes result in 'initial-state' radiation from the interacting partons or the W boson, giving the latter a transverse momentum component. Photon, quark and gluon radiation from the colliding partons is shown in figure 1.7 and 1.9. Photon radiation from the W boson is shown in figure 1.3 (right).

1.3   W boson production and decay

The Drell-Yan cross-section can be expressed as a 'hard' parton-level subprocess convoluted with the PDFs f_q and $f_{\bar{q}}$ of the proton and anti-proton respectively.
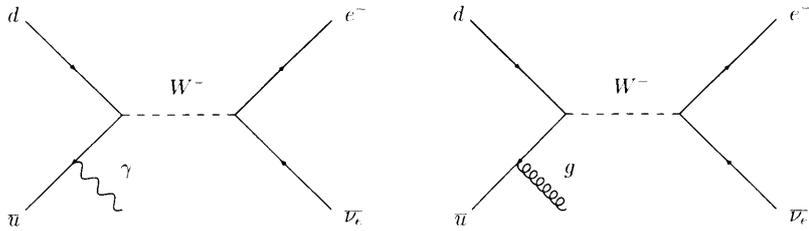
Figure 1.9: *W boson production with initial state (left) photon and (right) gluon radiation.*

At leading-order, this can be expressed as

$$\sigma = \sum_{}^{\text{all partons}} \int_0^1 \hat{\sigma} f_{\text{q}}(x_1, Q^2) f_{\bar{\text{q}}}(x_2, Q^2) dx_1 dx_2 \tag{1.22}$$

where $\hat{\sigma}$ is the cross-section of the parton-level subprocess describing the production and subsequent decay of the boson.

To describe the parton level cross-section for a boson of mass m, the relativistic propagator $q^2 - m^2$ must be modified to describe the boson decay. The finite boson lifetime results in an uncertainty in the boson mass (Γ_{W}). This is related to the proper lifetime τ by

$$\Gamma = \frac{\hbar}{\tau} \tag{1.23}$$

where $\hbar$ is the reduced Plank constant.

While it is sufficient to use the propagator $q^2 - m^2 + im\Gamma$ near the pole at $q^2 = m_{\text{W}}$, the effects of higher-order corrections to highly virtual bosons are properly included by using $q^2 - m^2 + iq^2\Gamma/m$ [18]. The denominator of $\hat{\sigma}$ contains the square of the propagator factor and, using $q^2 = \hat{s}$, the $\hat{s}$-dependent Breit-

36

Wigner cross-section can be expressed as

$$\hat{\sigma} = 12\pi \frac{\Gamma_{q\bar{q}}\Gamma_f}{m_W^2} \frac{\hat{s}}{(\hat{s} - m_W^2)^2 + (\hat{s}\Gamma_W/m_W)^2} \qquad (1.24)$$

where $\Gamma_{q\bar{q}}$ and Γ_f are the partial decay widths into the initial state and final state respectively. The cross-section as a function of $\sqrt{\hat{s}}$ is shown in figure 1.10 for $u\bar{d} \to W^+ \to e^+ + \nu_e$.
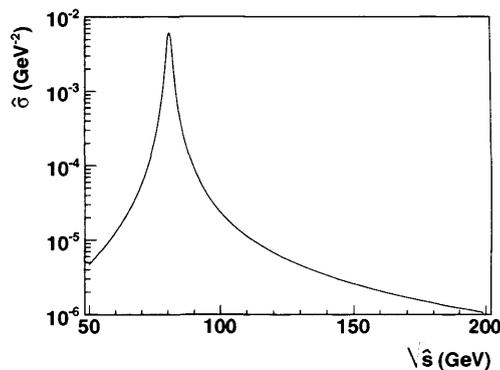
Figure 1.10: *The $\hat{s}$ differential parton level cross-section for $u\bar{d} \to W^+ \to e + \nu_e$.*

Real W bosons are produced near the pole at $\sqrt{\hat{s}} = m_W$, and have a cross-section that is independent of Γ_W, as $\Gamma_{q\bar{q}}\Gamma_f \propto \Gamma_W^2$. Conversely, virtual W bosons produced at $\sqrt{\hat{s}} \gg m_W$ have a cross-section that is approximately proportional to Γ_W^2. Hence a comparison of $\hat{\sigma}$ for real and virtual W boson production gives a measurement of Γ_W. It is not possible to measure $\hat{\sigma}$ or $\hat{s}$ directly at hadron colliders, rendering this approach impossible, but the related variables σ and m_T are well measured, and σ as a function of m_T, shown in figure 1.11 simulated for different values of Γ_W, is sensitive to the value of Γ_W. The cross-section is affected by higher-order corrections, PDFs, detector acceptance and resolution, and event contamination from other processes. Hence Γ_W cannot be extracted

from the data analytically, and a Monte Carlo simulation of the cross-section as a function of m_T is used instead. The value of Γ_W is obtained by comparing the simulated cross-section as a function of m_T with data.
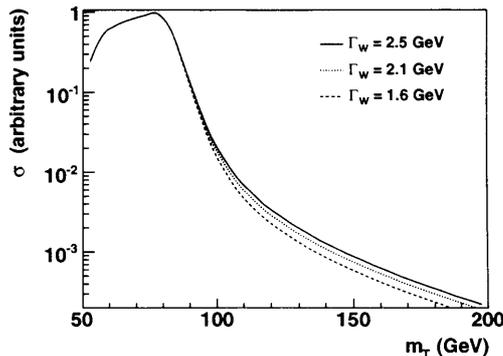
Figure 1.11: *The simulated W boson production cross-section as a function of m_T for different Γ_W values.*

1.3.1 W boson decay width prediction

In the standard model, the W boson decay width is theoretically predicted from the measured W boson mass and the measured Fermi constant. Any corrections to the decay width due to new physics can be absorbed into the renormalisation of the W boson mass and the Fermi constant. As a result their impact on the measurement of Γ_W is less than 1 MeV [19]. The W boson decay width is evaluated below using the latest world average of the W boson mass.

At leading-order, the standard model partial decay width for $W^+ \rightarrow e^+ \nu_e$ is given by

$$\Gamma^0_W = \frac{g^2 m_W}{48\pi} = \frac{G_F m_W^3}{6\pi\sqrt{2}} \tag{1.25}$$

where G_F is the Fermi constant. Using $G_F = 1.16637 \times 10^{-5}$ GeV^{-2}, measured

in muon decay [20], and the latest world average $m_W = 80.399 \pm 0.025$ GeV [21], the partial decay width is given by

$$\Gamma(W^+ \rightarrow e^+ \nu_e) = (1 + \delta^{\text{ewk}})\Gamma_W^0 = 226.47 \pm 0.25 \text{ MeV} \qquad (1.26)$$

including higher order electroweak corrections of $\delta^{\text{ewk}} = -0.4\%$ [19]. This correction is very small as most of the standard model electroweak corrections are included in m_W and G_F.

The W boson can decay via three leptonic channels and two quark doublet channels. W boson decay to the top quark, for $\hat{s} \sim m_W$, has a negligible cross-section due to the large mass of the top quark. The hadronic decay channels $q_i \overline{q_j}$ for W^+ decay, where the quark mass eigenstates $q_i = $ u,c and $\overline{q_j} = \overline{\text{d}}$, $\overline{\text{s}}$, $\overline{\text{b}}$, have partial widths

$$\Gamma(W^+ \rightarrow q_i \overline{q_j}) = 3|V_{ij}|^2(1 + \delta^{\text{QCD}} + \delta^{\text{ewk}})\Gamma_W^0 = (707.11 \pm 0.92)|V_{ij}|^2 \qquad (1.27)$$

where the factor 3 is the number of possible colour combinations and V_{ij} are the CKM matrix elements. The QCD correction (δ^{QCD}) to third order in α_s is

$$\delta^{\text{QCD}} = \frac{\alpha_s}{\pi} + 1.409\frac{\alpha_s^2}{\pi^2} - 12.77\frac{\alpha_s^3}{\pi^3} = 0.0410 \pm 0.0007 \qquad (1.28)$$

using $\alpha_s(M_W) = 0.120 \pm 0.002$ evaluated from the world average of $\alpha_s(M_Z) = 0.1176 \pm 0.002$, and evaluated at $Q = m_W$ using the NNLO renormalisation group equation [20].

Adding the two quark doublet and the three leptonic decay channels gives the

39

prediction of

$$\Gamma_W = 2.093 \pm 0.002 \text{ GeV} \tag{1.29}$$

with an uncertainty dominated by the uncertainty on m_W. This is in agreement with the prediction of $\Gamma_W = 2.0910 \pm 0.0015$ GeV using a value of m_W determined indirectly from EWK data [20].

1.3.2 W boson decay width measurements

Direct measurements of the W boson width have been made at the Super Proton Synchrotron (SPS), the Large Electron Positron Collider (LEP) and the Tevatron accelerators, and are shown in figure 1.12 and presented in table 1.3.2.
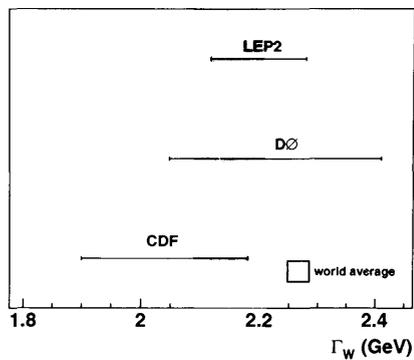
Figure 1.12: *Summary of direct W boson decay width measurements with the shaded region showing the world average with the measurement presented in this thesis exlcuded (UA1 is not shown).*

In addition to the direct method to measure the W boson decay width described above, indirect measurements can be made from the cross-section ratio of

$$R = \frac{\sigma(p\bar{p} \to W \to l\nu)}{\sigma(p\bar{p} \to Z \to l^+l^-)} = \frac{\sigma(p\bar{p} \to W)}{\sigma(p\bar{p} \to Z)} \frac{Br(W \to l\nu)}{Br(Z \to l^+l^-)} \tag{1.30}$$

Experiment	Year	Value/GeV	Uncertainty/GeV
UA1 [22]	1989	2.8	2.0
CDF [23]	2000	2.04	0.14
DØ [24]	2002	2.23	0.18
LEP2 [25]	2007	2.20	0.08
World average [25]	2007	2.15	0.06

Table 1.2: *Summary of direct W boson decay width measurements, with the measurement presented in this thesis excluded from the world average.*

where $Br(W \to l\nu) = \Gamma(W \to l\nu)/\Gamma(W)$ and $Br(Z \to l^+l^-) = \Gamma(Z \to l^+l^-)/\Gamma(Z)$. Using the value of R measured at CDF, together with the theoretical prediction of the total cross-section ratio and partial width $\Gamma(W \to l\nu)$ and the measured value of $Br(Z \to l^+l^-)$, the W boson decay width has been indirectly measured as $\Gamma_W = 2.08 \pm 0.04$ GeV [26]. While this provides the most precise measurement of Γ_W to date, it is not strictly a measurement of the total W boson decay width. Hence does not offer independent verification of the standard model.

Chapter 2

Experimental apparatus

The data used in this analysis has been collected at the Collider Detector at Fermi National Accelerator Laboratory (CDF) near Batavia, Illinois. CDF is located on the Tevatron, a superconducting proton-antiproton accelerator. This experiment has made many important discoveries and measurements in high energy physics, including the discovery of the top quark using data collected between 1992-1996 [14]. The Tevatron has since undergone a major upgrade to increase the centre-of-mass energy from 1.8 TeV to 1.96 TeV and to achieve a thirty fold increase in luminosity. The CDF detector has also undergone a major upgrade [27] and has continued to make important measurements and discoveries including the observation of time-dependent B_S^0-$\bar{B}_S^0$ oscillations in data collected between 2002-2006 [28]. This chapter contains an overview of the CDF detector and a detailed description of the subsystems used in this analysis.

2.1 Particle interaction and detection

2.1.1 Particle interaction

High energy particles are detected and tracked via their interaction with a medium. Energy transferred via interactions with the medium leave it in an excited or ionised atomic state, allowing detection. Energy loss mechanisms relevant to the simulation, described in section 6.2, and particle detection techniques relevant to the CDF analysis are briefly described below and can be found in more detail elsewhere [29].

Ionisation

Virtual photon exchange between a fast charged particle and an atom in the medium may result in the ionisation of the atom. The energy loss of the charged particle as it travels through the medium is parameterised by the Bethe-Bloch equation

$$-\frac{dE}{dx} = \frac{K}{\beta^2}\left[\frac{1}{2}\ln\frac{2m_{\mathrm{e}}c^2\beta^2\gamma^2 T_{\max}}{I^2} - \beta^2 - \frac{\delta}{2}\right] \tag{2.1}$$

where m_{e} and c are the electron rest mass and speed of light *in vacuo* respectively, $\beta = v/c$ where v is the particle speed and $\gamma = 1/\sqrt{1-\beta^2}$. The constant factor K, the ionisation potential I and the density effect correction δ are dependent on the material traversed. Ionisation is the dominant energy loss mechanism for high energy muons, and has a maximum kinetic energy transfer of

$$T_{\max} = \frac{2m_e c^2 \beta^2 \gamma^2}{1 + 2\gamma \frac{m_e}{m_\mu} + \left(\frac{m_e}{m_\mu}\right)^2} \qquad (2.2)$$

where m_μ is the muon rest mass.

Bremsstrahlung

A charged particle may emit a high energy (hard) photon to conserve momentum when scattered from the strong localised electric field of an atom. Bremsstrahlung is the dominant energy loss mechanism for relativistic electrons. The probability for radiation in a layer of material with fractional radiation length dX_0 is

$$P_\gamma = dX_0 \times \frac{4}{3}\left[\ln(y_{\max}/y_{\min}) - (y_{\max} - y_{\min}) + \frac{3}{8}(y_{\max} - y_{\min})^2\right] \qquad (2.3)$$

where $y_{\min}$ and $y_{\max}$ are the minimum and maximum fraction of the electron's energy transferred to the radiated photon.

Pair production

At high energy, photons in a medium can be converted into an electron-positron pair providing the photon has energy $E_\gamma \geq 2m_e + E_N$ where E_N is the kinetic energy gain of the recoiling atomic nucleus due to the transfer of the photon momentum. The photon conversion probability is

$$P_{\gamma \to e^+ e^-} = \frac{7}{9}dX_0 \qquad (2.4)$$

in the high energy limit [20].

Electromagnetic showers

Electrons traversing a medium with energy greater than about 10 MeV predominantly interact via bremsstrahlung radiation. As a radiated photon may then convert to an e^+e^- pair, a cascade of electrons, positrons and photons ensues. This electromagnetic shower will develop until the radiated photons are below the electron pair production threshold. Electromagnetic showers in the calorimeters, described in section 2.1.2, enable a measurement of the electron energy.

Hadronic showers

Hadrons interact with the atomic nucleus via the strong interaction. Hence the resultant shower contains hadrons in addition to electrons, positrons and photons. The composition of hadronic showers varies considerably due to the many different interactions that can occur. As the rate of energy deposition is particle dependent, the fluctuation in the energy measurement is greater for hadronic showers than for electromagnetic showers of the same energy. Hadronic showers are used to determine the energy of hadrons in the hadronic calorimeters described in section 2.5.2. They are used in this analysis, together with electromagnetic showers, to measure the event recoil, described in section 4.3 and the missing energy described in section 4.4.1.

2.1.2 Particle detection

Gas ionisation detectors

If the medium is normally a poor electrical conductor and the charge is able to move freely, the ionisation due to the charged particle can be detected. Gases such as Argon fall into this category. The gas is placed in a high electric potential and the ions will drift towards the cathode where they are detected. Gas ionisation detectors are best suited for tracking charged particles over large distances as the rate of energy loss of the fast particle is small due to the low density of the medium. The gas ionisation detectors at CDF are central to this analysis. They are used to measure the momentum of electrons and muons in the central outer tracker described in section 2.4.2 and to identify muons in the muon detectors described in section 2.6.

Solid state ionisation detectors

Carefully chosen impurities added to silicon can act as an electron donor (n-type silicon) providing an excess of electrons in the conduction band, or as an electron acceptor (p-type silicon) creating an excess of positively charged mobile 'holes'. A junction between these two silicon types will be traversed by electrons flowing into the p-type region and by 'holes' flowing in the opposite direction until the resultant potential across the junction blocks further charge migration. The region at the junction will then be depleted in charge carriers and any charge released in this area by ionising particles will migrate away from the depletion area giving a detectable current across the junction. The size of the depletion layer is increased by applying an external 'reverse-bias' electric potential across

the junction. Solid state detectors at CDF are the silicon detectors, described in section 2.4.1 and used in this analysis to determine the beam position.

Scintillation detectors

Molecules in an excited molecular state due to a virtual photon exchange may decay to the ground state via radiative de-excitation, where the energy is carried off by an emitted photon. Scintillating materials are transparent to the emitted scintillation light, allowing subsequent detection. Scintillating detectors are used to detect charged particles in the calorimeter, described in section 2.5, and muons in the muon chambers described in section 2.6.

Sampling calorimeters

To determine the total energy of the particle it must be brought to rest in the detector medium. As the rate of energy loss increases with atomic number, a compact detector medium is obtained by alternating a scintillator with an absorber. The shower evolution is then determined from the sampling scintillator layers by comparing them to test beam data and simulation. The calorimeters at CDF are sampling calorimeters.

2.2   Fermi National Accelerator Laboratory

The Fermi National Accelerator Laboratory (FNAL) has many experiments using the proton source at the heart of the laboratory, shown in figure 2.1. Protons and antiprotons are provided for the Tevatron, described in section 2.2.1, where they

47

are accelerated before being collided in the CDF and DØ detectors. The protons are also used to produce neutrinos for the Main Injector Neutrino Oscillation Search (MINOS) and the Booster Neutrino Experiment (BooNE), and fixed target experiments. The production and acceleration of protons and antiprotons for the Tevatron is briefly described below.

FERMILAB'S ACCELERATOR CHAIN
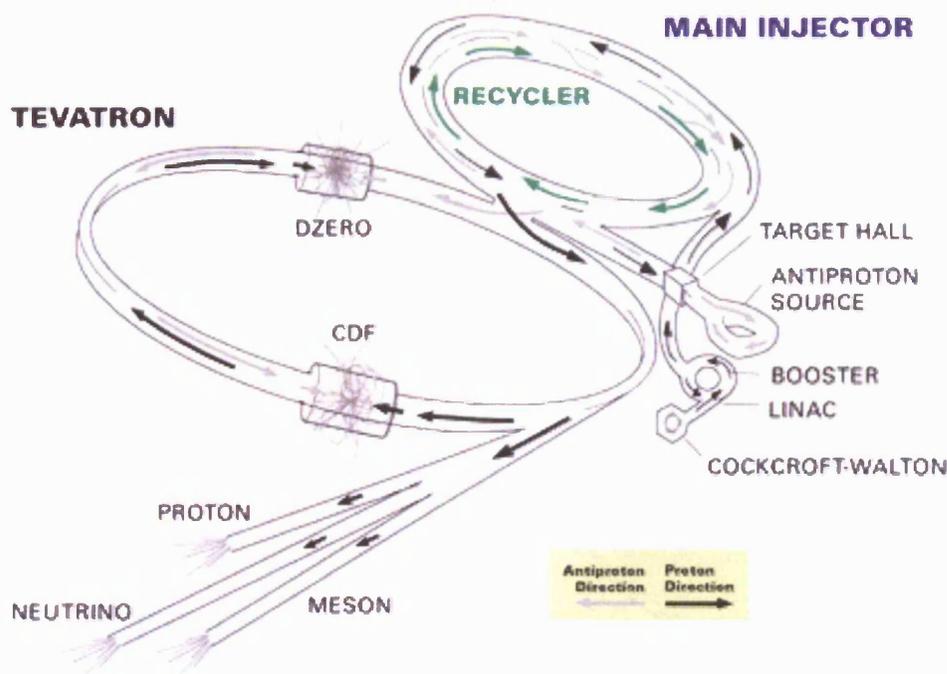
Figure 2.1: *The Fermi National Accelerator Laboratory.*

Proton production starts by ionising hydrogen gas to H^- ions which are accelerated to 750 KeV in the Cockcroft-Walton preaccelerator. Further acceleration to 400 MeV takes place in transit through the Linac to the 150 m diameter Booster synchrotron where the H^- ions are stripped of their electrons and accelerated to 8 GeV. The protons then go to the 1 km diameter Main Injector.

48

Antiprotons produced by colliding 120 GeV protons from the Main Injector onto a nickel target are captured and stored in the Debuncher and Accumulator respectively, in the triangular Antiproton Source tunnel. They then pass to the Recycler ring for storage before passing into the Main Injector. For a Tevatron injection, protons and antiprotons are further accelerated to 150 GeV.
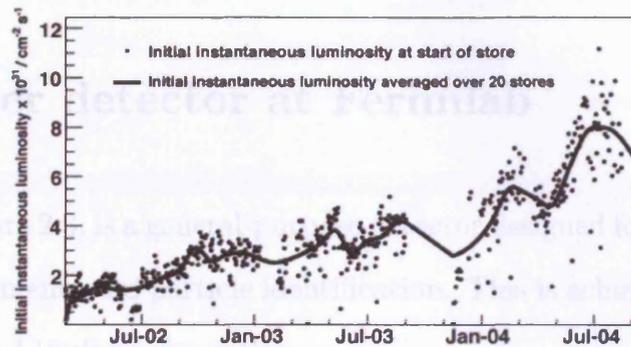
Figure 2.2: *Initial instantaneous luminosity delivered for data used in this analysis.*

2.2.1 Tevatron

The Tevatron accelerates protons and antiprotons in a 6 km circular orbit to a centre-of-mass energy of 1.96 TeV. The protons are kept on a circular orbit by 774 superconducting dipole magnets and focused by 216 superconducting quadrapole magnets. Eight radio frequency cavities accelerate the particles longitudinally along the beampipe. The protons and antiprotons are in 36 bunches initially containing approximately 300×10^9 and 50×10^9 particles respectively. These bunches cross every 396 ns and initially deliver an instantaneous luminosity of approximately 5×10^{31} cm^{-2}s^{-1}, providing around 2 interactions per bunch-crossing [27].

The luminosity decreases as the number of antiprotons decreases and, typically after a day, the collisions are stopped to begin a new 'store', replacing the proton and antiprotons with those produced during the previous store. The instantaneous luminosity at the beginning of the stores used in this analysis is shown in figure 2.2.

2.3 Collider detector at Fermilab

CDF, shown in figure 2.3, is a general-purpose detector designed for high-resolution kinematic measurements and particle identification. This is achieved using tracking, calorimetry and timing information.

The tracking subdetectors, described in section 2.4, provide vertex reconstruction and momentum measurements for ionising particles using silicon and gas drift chamber detectors embedded in a 1.4 Tesla magnetic field. Tracking is used in this analysis for lepton identification and W boson transverse mass reconstruction, both described in chapter 4. The calorimeter subdetectors, described in section 2.5, provide an energy measurement of particles that lose energy via electromagnetic and strong interactions. The calorimeter energy measurement is used in this analysis for lepton identification and W boson transverse mass reconstruction in the electron decay channel, both described in chapter 4. Muons pass through the calorimeters depositing only a small fraction of their total energy, and are detected in the muon tracking chambers described in section 2.6. The muon chambers are used in this analysis for muon identification described in section 4.2. Additional timing information is provided by the Time-of-Flight detector placed between the solenoid and the tracking volume to improve dis-
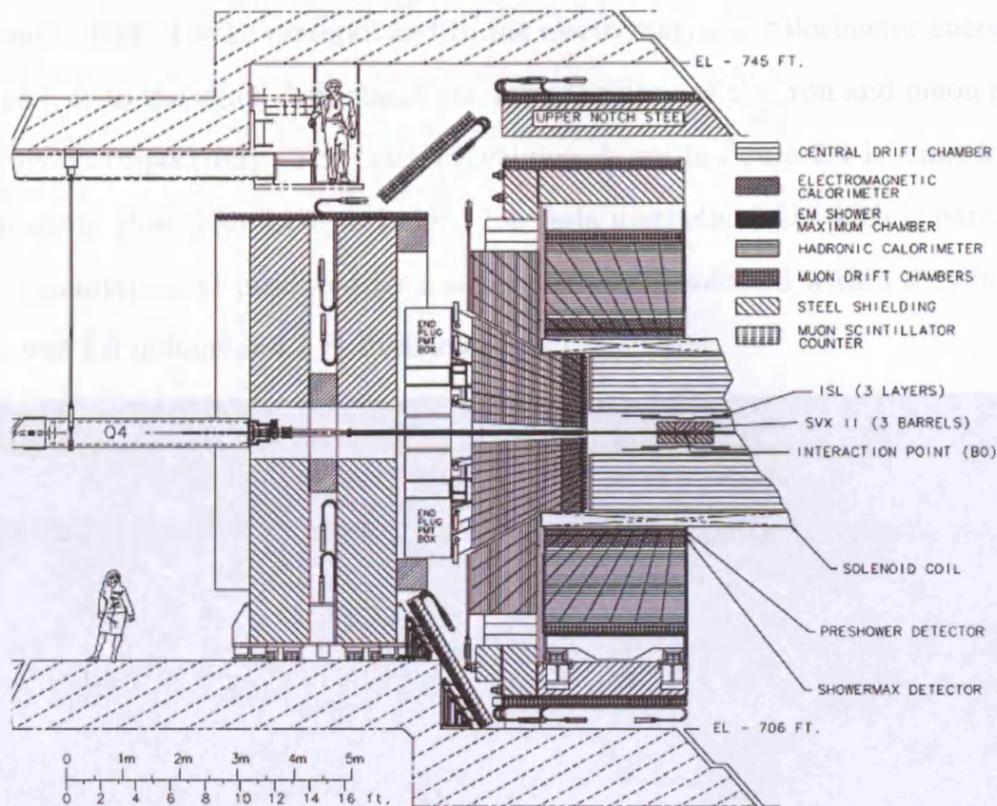
Figure 2.3: *Elevation view of half of the CDF detector.*

crimination between low momentum hadrons[30]. The luminosity is measured by gaseous Cherenkov detectors located close to the beampipe by measuring particles from inelastic collisions [31]. The miniplug calorimeters located at $3.6 < |\eta| < 5.1$ provide information for diffractive physics [32].

2.4 Tracking

Tracking is essential for charged particle identification and reconstruction. It provides the momentum measurement from the track curvature, which is then combined with information from regions near the extrapolated track in other

subdetectors. Tracks extrapolated to the electromagnetic calorimeter energy deposits, or to the muon drift chambers, form the basis of electron and muon reconstruction respectively. The tracking volume shown in figure 2.4 is embedded in a uniform (less than 0.1% variation) 1.4 Tesla magnetic field which is parallel to the beampipe and produced by a superconducting solenoid within a cylindrical volume 4.8 m long and 3 m in diameter.
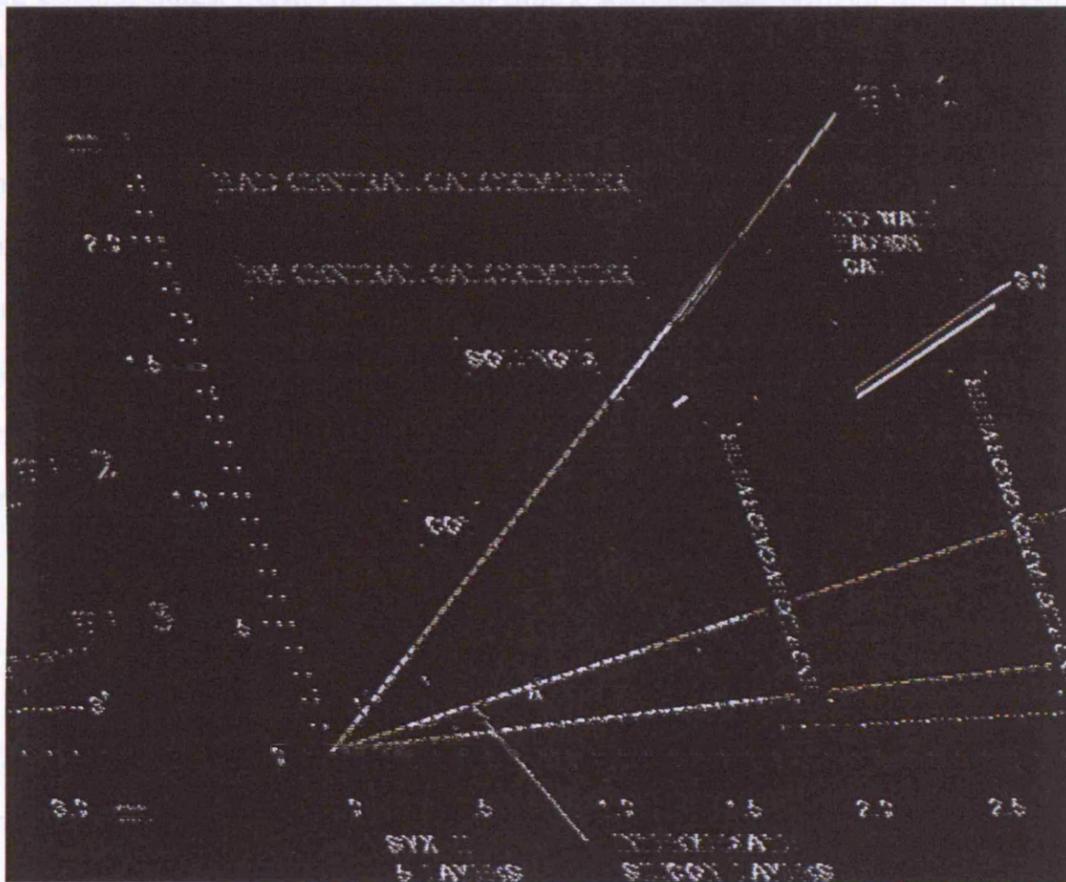
Figure 2.4: *Tracking volume of the CDF detector.*

2.4.1 Silicon tracking

The silicon tracking (SVX) detector [33] allows very fine granularity tracking close to the interaction point in the region $| \eta | \leq 2.0$. It comprises three cylindrical sections 29 cm long. These extend radially from 2.5 cm to 11 cm, providing high resolution 3-dimensional tracking to reconstruct secondary vertices, including bottom quark decays used in top quark searches and bottom quark physics. Although not required by this analysis, when the SVX is operational it is used to provide a measurement of the track impact parameter to improve the background rejection for muon candidate events described in section 4.2. The SVX is also used to provide data for the beam position measurement used in electron and muon track reconstruction, described in section 3.1. Additional silicon, not used in this analysis, is added between the beampipe and the SVX (Layer 00) to improve vertex reconstruction, and between the SVX and the central outer tracker (ISL) to improve tracking resolution in the forward regions.

2.4.2 Central outer tracker

The central outer tracker (COT) [34] is a large cylindrical drift chamber used to track charged particles with $| \eta | \leq 1.0$. The p_T measurement used in this analysis is made using a track reconstructed from COT hits and the beam-position. The beam-position is measured using SVX hits, if available, or else COT hits. The COT is located between the SVX and the central calorimeter between 40 cm and 137 cm radially. It extends 155 cm in both directions parallel to the beam pipe with a spacer to support the field sheets between the two halves at $z = 0$ [35]. The gas mixture and cell arrangement provide a maximum drift time of 100 ns,

considerably less than the bunch crossing time of 396 ns.

The COT is constructed from cells 310 cm long, containing 12 wires with an 8 mm separation. The electrostatic field around the sense wires is maintained and shaped by potential wires, shaper wires and field panels, shown in figure 2.5.
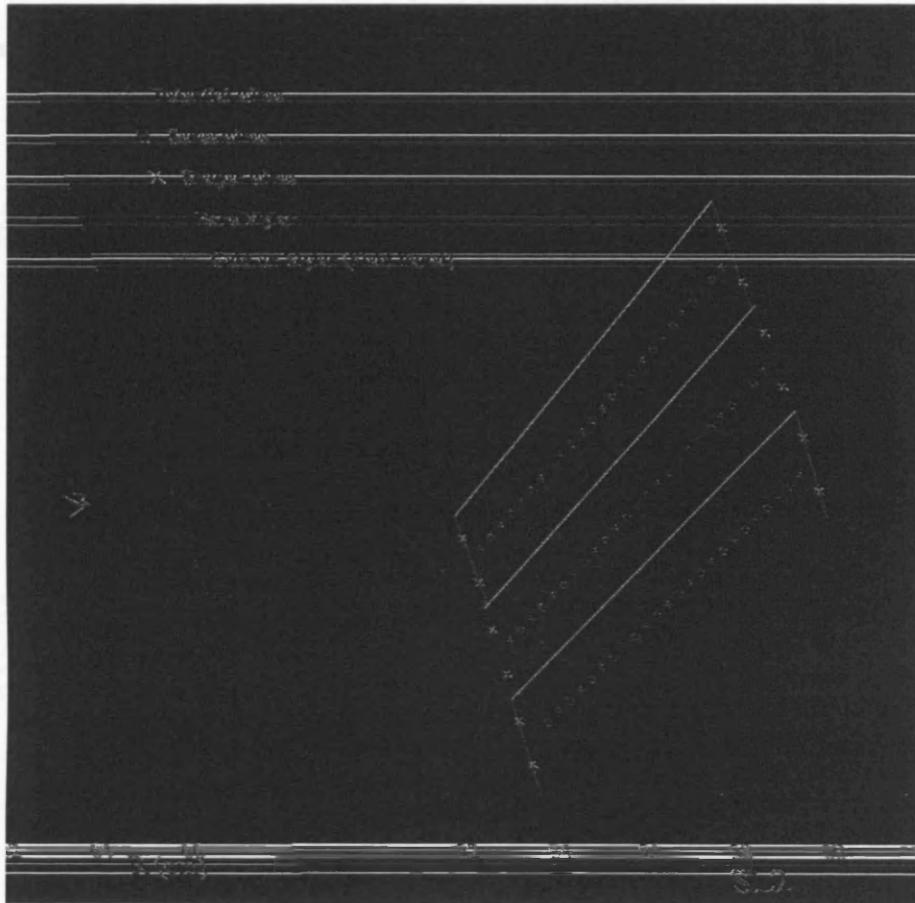
Figure 2.5: *The central outer tracker cell layout in superlayer (SL) 2.*

The cells are arranged into 8 superlayers (SL) shown in figure 2.6. The superlayers alternate between the stereo configuration, where the wires make a 3° angle to the magnetic field, and an axial configuration where the wires are parallel with the field, providing a position measurement in the z direction.

Amplifier-Shaper-Discriminator (ASD) chips are mounted on the cell end-plate and perform analogue processing on the signal from the sense wire. The signal is then converted into a digital signal by Time to Digital Converter (TDC) modules. Information is fed into the Extra Fast Tracker (XFT), described in section 2.8.1, and the L1 Storage Pipeline, the first stage of the data acquisition system described in section 2.7.
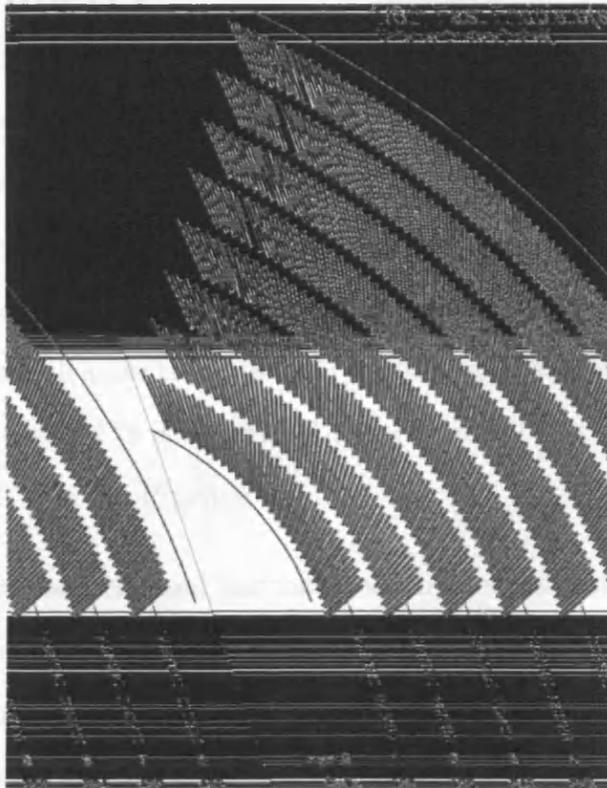
Figure 2.6: *Central outer tracker superlayers. Even numbered layers are axial, odd are stereo.*

The COT has over 6,000 associated calibration values. Many of these are regularly updated to maintain high precision data, providing a higher p_T-resolution for leptons used in this analysis. The calibration values include the individual readout times of the 30240 channels. The readout times are regularly measured by sending

a charge pulse to all ASDs simultaneously and comparing the TDC readouts. This provides each channel with a time offset (t_0) from the average time. Also fits are performed whilst data are being taken in order to determine the drift velocity and the global timing offset.

2.5 Calorimetry

CDF has two types of calorimeter, electromagnetic and hadronic, measuring the energy of particles that interact via the electromagnetic and strong force respectively. Sampling calorimeters are used, and the photons in the scintillation layers are reflected to the read-out edge where they traverse a wavelength-shifting light guide to the photomultiplier tubes (PMT) located on the outer calorimeter edge. The charge from the PMTs is integrated and converted to a digital signal which is stored in the L1 Storage Pipeline.

The central electromagnetic and hadronic calorimeter subsystems are embedded in wedges covering 15° in azimuth and arranged in two cylinders, with a small gap between them at $z = 0$, to provide complete azimuthal coverage for $|\eta| < 1$. The radial location is between the COT and the muon chambers. Each wedge is divided along its length, in z, into 10 towers that project from the origin and, except for the last wedge, have equal coverage in pseudorapidity as shown in figure 2.7.
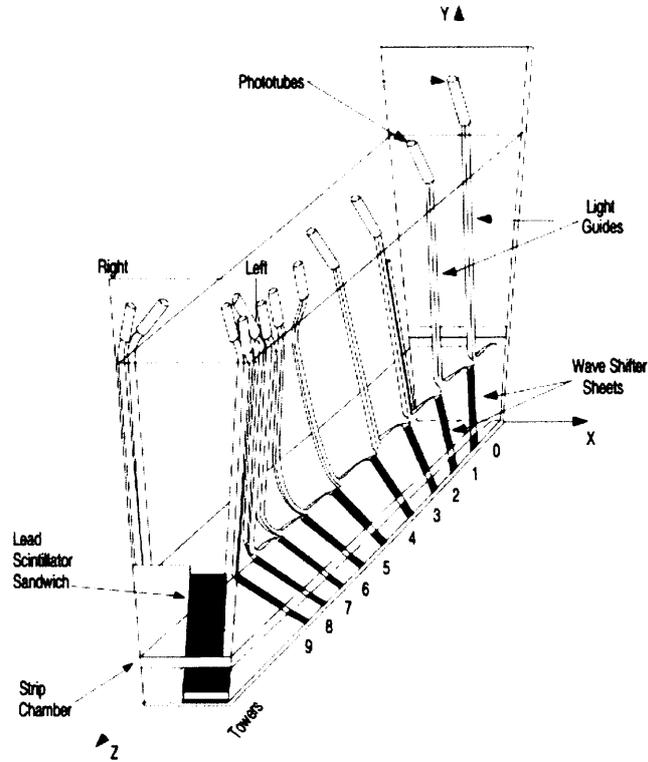
Figure 2.7: *Central calorimeter wedge showing the electromagnetic calorimeter towers.*

2.5.1 Central electromagnetic calorimeter

The central electromagnetic (CEM) calorimeter [36] is used in the identification and energy measurement of electrons and photons. It has 31 layers of scintillator separated by lead absorbers. Each tower subtends 15° in azimuth and 0.1 units of pseudorapidity. The measured energy of the high energy electrons and photons used in this analysis fluctuates about their true energy. The detector resolution, defined here as the mean fluctuation as a fraction of the measured energy, has a stochastic component, determined from test beam data as $13.5\%/\sqrt{E_T}$, and a constant component $\kappa = 1.5\%$ which are added in quadrature [37]. The detector response, defined as the ratio between the measured and true energy, together

with the resolution are calibrated initially using test beam data and during accelerator shutdowns using a radioactive source. Additionally, a laser system is regularly used to calibrate changes in response across towers (tower-to-tower corrections). High p_T electron tracks also provide time-dependent corrections to the response. The measurement of the constant term (κ) and additional corrections to the response is described in section 6.4.3.

Additional detectors measuring the 2-dimensional charge distribution are located at the front of the calorimeter, the central pre-radiator (CPR) detector, and after the eighth lead layer, the central shower-maximum (CES) detector, where the shower is at a depth where its transverse size is typically at a maximum.

The CPR and CES consist of gas-based detectors to measure the charge deposition on orthogonal strips, in the ϕ direction, and wires in the z direction. The charge is integrated and converted to a digital signal which is stored in the L1 Storage Pipeline. Energy deposited in the CES is clustered to determine the location of the shower centre, in the plane of the CES detector, which is used in this analysis to select electrons that traverse the central region of the calorimeter wedge, described in section 4.1.

2.5.2 Central hadronic calorimeter

The central hadronic (CHA) calorimeter [38] has alternating iron and scintillator layers. The response and resolution of the detector is calibrated using pion test beams and *in situ* using isolated tracks. The resolution (σ_H) for charged pions is found to be $\sigma_H/E_T = 50\%/\sqrt{E_T} \oplus 3\%$ [37]. The CHA is used in this analysis to reject events with energy deposits inconsistent with electrons or muons.
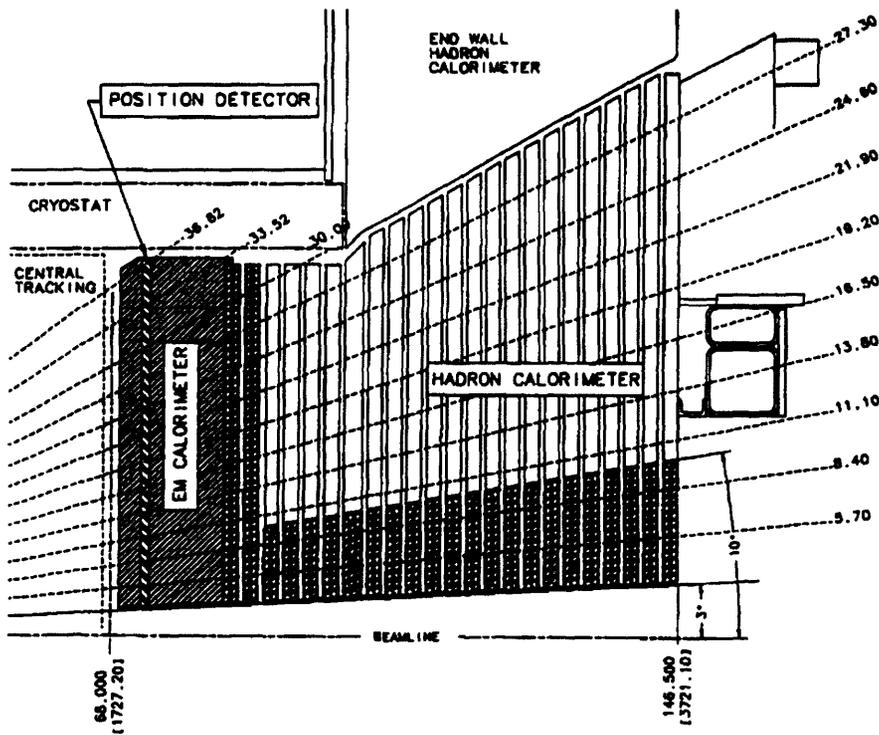
Figure 2.8: *Plug calorimeters.*

2.5.3 Plug calorimeters

The 'plug' electromagnetic (PEM) and hadronic (PHA) calorimeters, shown in figure 2.8, cover a range of $1.1 < |\eta| < 3.6$ and are constructed in a similar fashion to the central calorimeters with lead absorber between the scintillation layers in the PEM and steel absorber in the PHA. Located to provide coverage in the gap between the CHA and the PHA, the 'end-wall' (WHA) hadronic calorimeter has the same structure as the CHA. These detectors are used in this analysis in the recoil measurement, described in section 4.3, and the missing transverse energy ($\slashed{E}_T$) measurement described in section 4.4.1.

2.6 Muon chambers

The large rest mass of the muon suppresses interaction with matter via bremsstrahlung radiation compared to the electron. The muon therefore predominantly interacts via ionisation, passing through the calorimeters depositing only a small fraction of its total energy. Muon identification is made using drift chambers and scintillation counters located behind the calorimeters. A muon signature, referred to as a muon 'stub', has hits in multiple drift chambers with scintillation counter hits synchronous with the beam crossing. In addition to a stub, a muon candidate has a matching COT track used to measure the muon candidate momentum. The complete identification requirements for muon candidates are described in section 4.2.

Electrons and the majority of hadrons are absorbed in the electromagnetic and hadronic calorimeters and do not reach the muon chambers. However some pions do make it through the hadronic calorimeter and provide a source of background in the central muon detector referred to as 'punch through'. Tau leptons have an insufficient lifetime to reach the muon chambers. The coverage of the muon chambers is shown in figure 2.9.

A drift chamber contains a sense wire lying on the same plane as the beampipe, and is filled with an Argon-Ethane mixture. The chamber is maintained at a high electrostatic potential by the central wire and the trail of ionisation produced by a charged particle traversing the gas will drift at a constant speed to the sense wire. The resultant pulse is then converted into a digital signal by TDCs.

In addition to the three muon subsystems described in more detail below, the barrel muon detector extends coverage to forward regions, covering $1.0 < |\eta| < 1.5$,
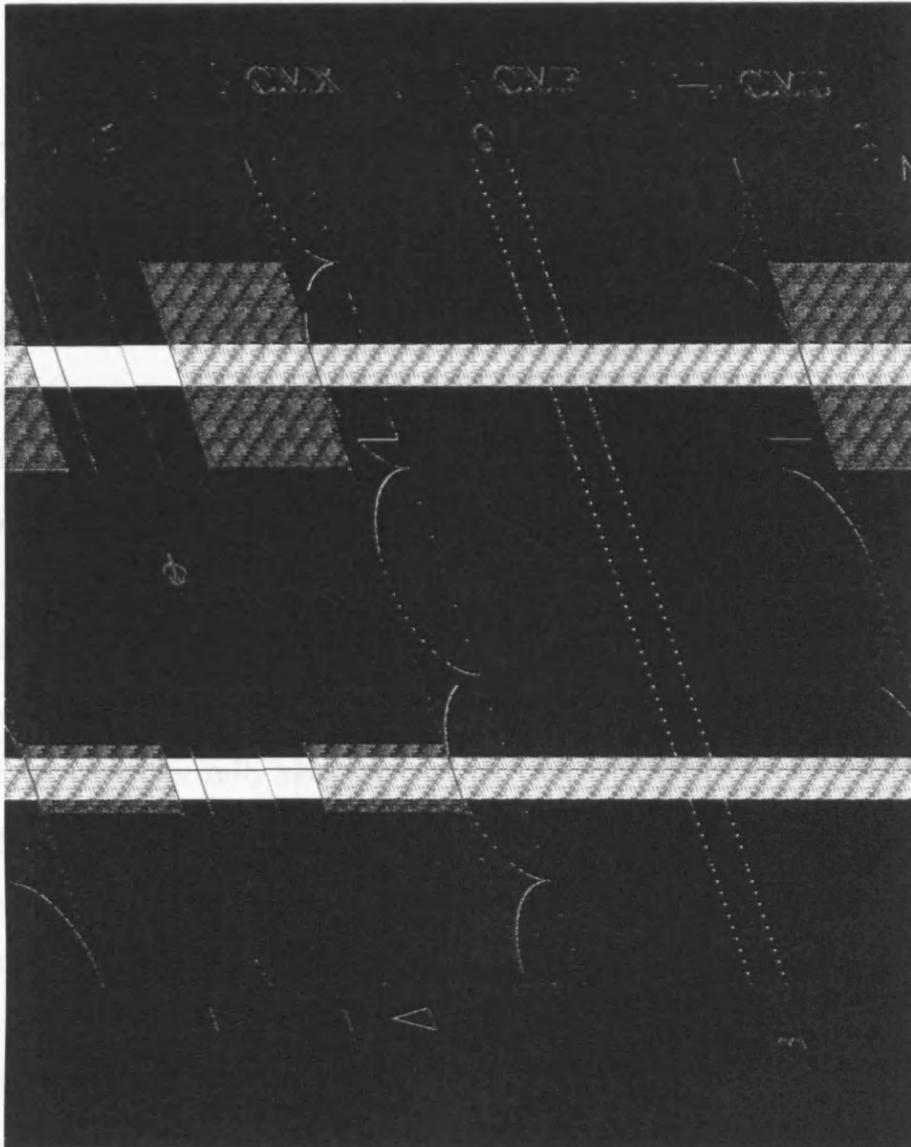
Figure 2.9: *Muon subdetector coverage in the η-φ plane (shaded areas). The acceptance of the central muon (CMU) and central muon upgrade (CMP) subdetectors, located in the region |η| ≤ 0.65, and the central muon extension (CMX) subdetector, located in the region 0.65 ≤ |η| ≤ 1.0, are shown. In this analysis, muons with tracks in the CMU subdetector must also have tracks in the CMP subdetector, and the combined acceptance is determined by the CMP acceptance (shaded), which covers a smaller area in the η-φ plane than the CMU.*

and is not used in this analysis.

2.6.1 Central muon detector

The central muon (CMU) detector is cylindrical about the beampipe and located behind the central calorimeter. It consists of 3 modules 226 cm long arranged directly behind the calorimeter tower to cover 12.6° in azimuth with a 2.4° gap between wedges. This provides a coverage of $|\eta| \leq 0.65$ with a gap of 18 cm between the two halves for the detector support structure. Each module contains 16 cells shown in figure 2.10. Each cell is 6.5 x 2.5 x 226 cm and has a 50 μm stainless steel wire at the centre. The wires of the first and third cells are slightly offset from the second and fourth and have their wires connected to reduce the number of channels read out by the TDCs. Similarly, the second and fourth wires are also connected before being read. The separate pulses traversing the connected wires are fully resolvable so no loss of information results from this arrangement. A comparison of drift times across radially aligned wires gives a crude momentum measurement used for low level triggering. Additionally each wire has an ADC on each end to determine the z location of the hit.
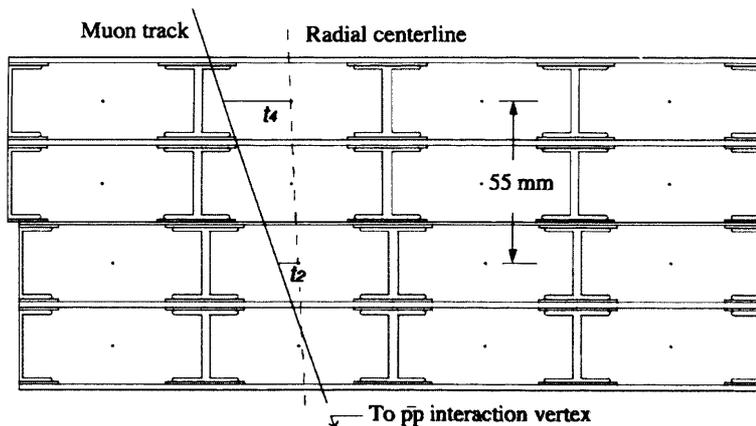
Figure 2.10: *Transverse view of a CMU wedge.*

2.6.2 Central muon upgrade

The central muon upgrade (CMP) detector comprises drift chambers with a 2.5 x 15 cm cross-section and typically 640 cm in length arranged in a rectangular geometry around the CMU, providing approximately the same coverage. It is placed behind 60 cm of steel greatly reducing charged pion 'punch through'. Again the chambers are arranged 4 deep and alternating layers are offset. Additionally, there is a layer of scintillation counters on the outside of the drift chambers to provide additional timing information. Muon candidates are required to have both CMU and CMP hits in addition to scintillation hits that are in time with the beam crossing.

2.6.3 Central muon extension

The central muon extension (CMX) detector consists of a conical arrangement of drift chambers about the beampipe in the region $0.65 \leq |\eta| \leq 1.0$. It covers 240° in azimuthal angle with a 30° gap at the top for the refrigeration system and a 90° gap at the bottom where it meets the floor of the collision hall. The drift chambers differ only in length to those used in the CMP. The trajectory of a particle to the CMX traverses many more radiation lengths than to the CMU so additional absorbing material between the drift chambers and the interaction point is not necessary. A layer of four scintillation counters (CSX) on both the inside and outside surface of the drift chamber arrangement provides high resolution timing to reject hits not in time with the collision.

Additional detectors in the 'keystone' and 'miniskirt' regions were added to fill the gaps in the original CMX coverage, and cover the top two wedges on the

negative z side and the area around the collision hall floor respectively. These subdetectors are not used in this analysis.

2.7 Data acquisition

Information from collisions is reduced from a rate of 2.5 MHz, the bunch-crossing rate, to 75 Hz before being written to tape. A modular system is used to select events containing signatures of interesting physics, which are subsequently written to tape based on an analysis using the fully reconstructed event. This system, shown schematically in figure 2.11, is described below with reference to the triggers used to select high p_{T} electrons and muons in this analysis.

Physics of interest will have particular signatures that are searched for in three stages using increasing levels of information and sophistication. The triggering is split into stages since there is insufficient time for full event reconstruction, which does not happen unless the third level is reached. Triggers in these stages have an associated selection efficiency described in section 6.5. Each level has a set of criteria the data must meet to be written to tape, and the trigger path is the full set of requirements. About 170 different trigger paths are used at CDF to cover a broad range of interesting physics. The trigger paths and associated algorithms used in this analysis are described in section 2.8.

2.7.1 Level 1 trigger

The level 1 trigger (L1) is a synchronous hardware trigger providing a decision for every event. This is facilitated by having all of the front-end electronics fully

Figure 2.11: *Trigger dataflow.*

pipelined with onboard buffering for 42 beam crossings. The high decision rate is achieved by fast and simple algorithms that consider low-level objects such as COT and muon chamber hits and individual calorimeter energy deposits. Hits in axial COT superlayers are linked together to determine the p_T and extrapolated to other detector regions. Tracks matching a calorimeter tower energy deposit or hits in the muon chambers are considered for electron and muon candidates respectively. Also calorimeter energy is summed to indicate the presence of high E_T 'jets' of hadrons, and to obtain the $\not{E}_T$ measurement, defined in section 4.4.1,

65

used to indicate the presence of a neutrino.

2.7.2   Level 2 trigger

The level 2 trigger (L2) receives events from L1 at a rate of 20 kHz and provides an asynchronous decision based on objects built from combining information written to a buffer as the result of the L1 accept decision. Calorimeter towers are clustered at this stage and rematched with COT tracks.

2.7.3   Level 3 trigger

The level 3 trigger (L3) receives events from L2 at a rate of 300 Hz. Event data in the different buffers are collected by the event builder [39] and sent to a farm of Linux PCs where the events are fully reconstructed. Events take approximately one second to be processed and those passing the L3 requirements are subsequently written to robotic tape storage as raw data.

2.7.4   Offline reconstruction

Raw data written to tape are processed again offline, using calibration and alignment parameters obtained from the data, before being used for analyses [40]. Offline event reconstruction is done using a farm of Linux PCs, and reconstructed events are written to tape. The detector calibration and alignment parameters used for the offline reconstruction are described in chapter 3.

2.8 Lepton trigger paths and algorithms

The full set of requirements and the associated algorithms for the selection of events containing high p_T leptons are described below, with a detailed description of the relevant quantities given in chapter 4.

2.8.1 Extra fast tracker and extrapolation unit

The extra fast tracker (XFT) is used to determine the trajectory and momentum of tracks in the COT. It is used for online event selection in the L1 and L2 triggers as there is insufficient time for full track reconstruction. The first stage, the finder, takes information from the four axial superlayers and searches for high p_T segments by comparing hit configurations with pre-programmed look-up tables. The linker then performs a parallel search on all the segments to find the highest p_T track made from all four axial superlayer segments in a phi-slice of $\Delta\phi = 1.25°$. It has recently been upgraded to accommodate the effect of the increased chamber occupancy due to the increase in luminosity [41]. Information then passes to the extrapolation unit (XTRP) and tracks are extrapolated to other subdetectors.

2.8.2 Electron clustering

At L1, only energy deposits in individual towers are considered. At L2, the central calorimeter towers are grouped into a 24 × 24 grid in the η-ϕ plane. Clusters are then formed recursively by adding adjacent towers that contain sufficient E_T deposits to the seed tower. At L3, the central calorimeter clusters are formed by

recursively taking the highest E_T tower and adding unclustered adjacent towers from the same wedge that contain sufficient E_T deposits.

2.8.3 Electron trigger paths

An electron candidate passing the electron trigger path is required to have a COT track that extrapolates to energy deposited in the CEM calorimeter (E_{em}) with minimal energy flow (E_{had}) into the hadronic calorimeter behind. The latter requirement is met if the quantity E_{had}/E_{em} is small. At L3 tracks are fully reconstructed while L1 and L2 use the XFT and XTRP, described in section 2.8.1, to determine the track p_T and the extrapolated calorimeter position respectively. The trigger path for high p_T electrons used in this analysis is ELECTRON_CENTRAL_18.

The requirements of the ELECTRON_CENTRAL_18 trigger path are:

L1_CEM8_PT8 at L1 which requires two CEM towers within the same wedge with a combined E_T greater than 8 GeV and E_{had}/E_{em} less than 0.125 and an XFT track that extrapolates to the tower. The XFT track must have at least 10 (11) hits in at least 3 (4) superlayers with p_T greater than 8.34 GeV.

L2_CEM16_PT8 at L2 which requires a central EM cluster with E_T greater than 16 GeV and E_{had}/E_{em} less than 0.125 and an XFT track with p_T greater than 8.34 GeV that extrapolates to the cluster seed tower.

L3_ELECTRON_CENTRAL_18 at L3 which requires a reconstructed cluster with E_T greater than 18 GeV and E_{had}/E_{em} less than 0.125 and a COT track with

p_T greater than 9 GeV that extrapolates to the cluster. In addition, from January 2003 the following four requirements are made: Firstly, the comparison of the energy profile of the towers in a cluster with that predicted from test beam data, defined in equation 4.1, is required to be less than 0.4. Secondly, the distance in the z direction between the track CES position and the matched cluster position in the CES is required to be less than 8 cm. Thirdly, the E_T is calculated using the origin of the extrapolated track instead of the nominal interaction point and lastly the number of hadronic towers used in the calculation of $E_\mathrm{had}/E_\mathrm{em}$ is increased from two to three.

The W_NOTRACK trigger path selects electron candidates from W boson decays without any track requirements. The presence of the W boson is inferred from large $\not{E}_\mathrm{T}$ carried away by the neutrino. This trigger path is used to measure the efficiencies of the XFT requirements in the ELECTRON_CENTRAL_18 trigger path.

The requirements of the W_NOTRACK trigger path are:

L1_EM8_&_MET15 at L1 which requires, in addition to the calorimeter requirements in L1_CEM8_PT8, a $\not{E}_\mathrm{T}$ greater than 15 GeV. From January 2003, the plug calorimeter is included in the $\not{E}_\mathrm{T}$ sum.

L2_CEM16_L1_MET15 at L2 which requires, in addition to only the calorimeter requirements of L2_CEM16_PT8, the L1 $\not{E}_\mathrm{T}$ requirement.

L3_W_NOTRACK_MET25 at L3 which requires, in addition to the calorimeter requirements of L3_ELECTRON_CENTRAL_18, a $\not{E}_\mathrm{T}$ greater than 25 GeV.

2.8.4 Muon trigger paths

A muon candidate passing the muon trigger is required to have a stub in the muon drift chambers with a matching COT track. A stub requires multiple matching hits in either the CMU and CMP chambers, or the CMX chambers and the CSX scintillators. For L1 and L2, the track p_T and extrapolated position in the muon chamber is determined by the XFT and the XTRP respectively. At L3 the COT track is fully reconstructed and extrapolated to the muon chambers to calculate the distance (Δx_{cmu}, Δx_{cmp} and Δx_{cmx}) between the extrapolated track and the stub in the CMU, CMP and CMX chamber respectively.

The trigger paths for high p_T muons used in this analysis are MUON_CMUP18 and MUON_CMX18. An increasingly stringent L2 trigger requirement was required to keep the rate of other 'fake' muon events low as the luminosity increases.

The requirements of the MUON_CMUP18 trigger path are:

L1_CMUP6_PT4 at L1 which requires hits on both CMU wire pairs within 124 ns of each other. These hits must have a matching XFT track with p_T greater than 4.09 GeV. The CMP must have hits in 3 of 4 layers in the projected direction of the CMU hits.

L2_AUTO_L1_CMUP6_PT4 at L2 which requires the corresponding L1 trigger. This trigger was used until October 2002.

L2_TRK8_L1_CMUP6_PT4 at L2 which requires an XFT track with p_T greater than 8.34 GeV. This trigger was used between October 2002 and April 2004.

L2_CMUP6_PT8 at L2 which requires an XFT track with p_T greater than 8.34

GeV extrapolating to hits in the CMU and CMP. This trigger was used after April 2004.

L3_MUON_CMUP18 at L3 which requires a reconstructed muon candidate with a track p_T greater than 18 GeV. The reconstructed track must extrapolate to a stub in the CMU and CMP with $|\Delta x_{cmu}|$ less than 10 cm and $|\Delta x_{cmp}|$ less than 20 cm.

The requirements of the MUON_CMX18 trigger are

L1_CMX6_PT8 at L1 which requires hits on both CMX wire pairs within 124 ns of each other. The hits must have a matching XFT track with p_T greater than 8.34 GeV. This trigger was used until October 2002.

L1_CMX6_PT8_CSX at L1 which requires, in addition to the above trigger requirements, a CSX scintillator hit. This trigger was used after October 2002.

L2_AUTO_L1_CMX6_PT8 and L2_AUTO_L1_CMX6_PT8_CSX at L2 which requires the corresponding L1 trigger. This trigger was used until April 2004.

L2_CMX6_PT10 at L2 which requires an XFT track with a p_T greater than 10.1 GeV extrapolating to hits in the CMX. This trigger was used after April 2004.

L3_MUON_CMX18 at L3 which requires a reconstructed muon with a track p_T of at least 18 GeV. The reconstructed track must link with the CMX stub with $|\Delta x_{cmx}|$ less than 10 cm.

2.9 Datasets

Data written to tape is catalogued into different datasets depending on the type of event, as determined by the associated trigger paths described in section 2.8. Events of interest for this analysis will contain high p_T electrons or muons.

The high p_T electron dataset containing electrons from the ELECTRON_CENTRAL_18 and W_NOTRACK trigger path is used in this analysis. The W_NOTRACK trigger path is used to estimate the efficiency of the ELECTRON_CENTRAL_18 trigger path in section 6.5.1 and the ELECTRON_CENTRAL_18 trigger path is used for all other electrons. The high p_T muon dataset containing muons from the MUON_CMUP18 and MUON_CMX18 trigger paths is used for muons. Only data collected when the necessary subdetectors are fully operational are used in this analysis, and are selected according to the standard 'good run' criteria [42], but without requiring the silicon subdetector to be functional. This gives an integrated luminosity of 370 ± 18 pb^{-1} for electrons and 330 ± 16 pb^{-1} for muons.

Chapter 3

Calibration management

Each sub-system of the CDF detector described in chapter 2 has components that are calibrated, often regularly. The calibration values, such as those produced during CEM calibrations described in section 2.5.1 and values describing the status of the detector, are stored in a relational database for retrieval at a later date. These individual values, henceforth referred to as calibrations, are collected into a single table and accessed when reconstructing events offline for subsequent use in analyses. This chapter describes the process in detail with reference to the central electromagnetic calorimeters and COT calibrations, described in section 2.5.1 and 2.4.2 respectively, as these are vital in obtaining a good resolution for the energy and momentum measurement, described in section 6.4 and 6.3 respectively, and used in the fit described in chapter 8 to determine the W boson decay width.

The author's contribution to this area is the creation of a set of tools that bring the individual calibrations together into a single complete set, described in section 3.3, and the monitoring and validation of this process, described in section 3.4.

3.1 Types of calibrations

The calibrations fall into three broad groups based on the method of production and the timescale over which they change. Data written to tape are grouped into sections called 'runs', typically lasting a few hours, which represent a collection of data for which the detector hardware and software configurations remained unchanged. This is the shortest timescale over which calibrations change.

Online calibrations depend on the exact running conditions that prevail whilst data are being collected. These are written to the database for each run whilst the run is in progress. Examples include the COT drift model fits and general detector parameters such as the operating voltage and list of bad channels.

Offline calibrations change over longer time scales and are made by performing special detector calibrations typically every few months. Examples include the CEM time dependent gain calibrations described in section 2.5.1.

Post reconstruction calibrations are produced from the analysis of fully reconstructed events. These are made before the production of the full offline reconstruction of the events used for analyses. Examples include the beam position produced from reconstructed vertices, that are used in this analysis to provide an extra point when fitting to track hits, described in section 4.1.

3.2 Database structure

Each run is associated with a complete set of calibrations comprising over 150,000 individual values used for the offline reconstruction of events. As the detector system is inherently modular, with each subdetector producing its own set of calibrations either online or later offline, many intermediate calibration sets are created before the final set. Also by the time the CDF detector stops taking data, the number of runs is likely to be in excess of 100,000 so minimising the database size is an essential consideration of database design. Additionally some of the calibrations are unchanged over multiple runs and final calibration sets for each run contain many identical elements. Database size is kept to a minimum by using a relational database structure where each individual calibration only has a single entry.

Simple access to the complete set of 'official' calibrations is necessary for offline reconstruction and other uses. Also a record of all database activity is necessary to eliminate possible data loss and to allow complete access to all past conditions. This is achieved by disallowing an entry to be changed once written. Another important consideration is the ability to merge two sets of calibrations that both contain instances of the same calibration, taking only the latest. The schema used, based on these considerations, is described below. An Oracle database is used, and is interfaced to using the Structured Query Language (SQL) [43].

3.2.1 Calibration retrieval

Simple access to a set of calibrations for a range of runs (defined as a 'pass') must be possible without a detailed knowledge of the database structure. A simple
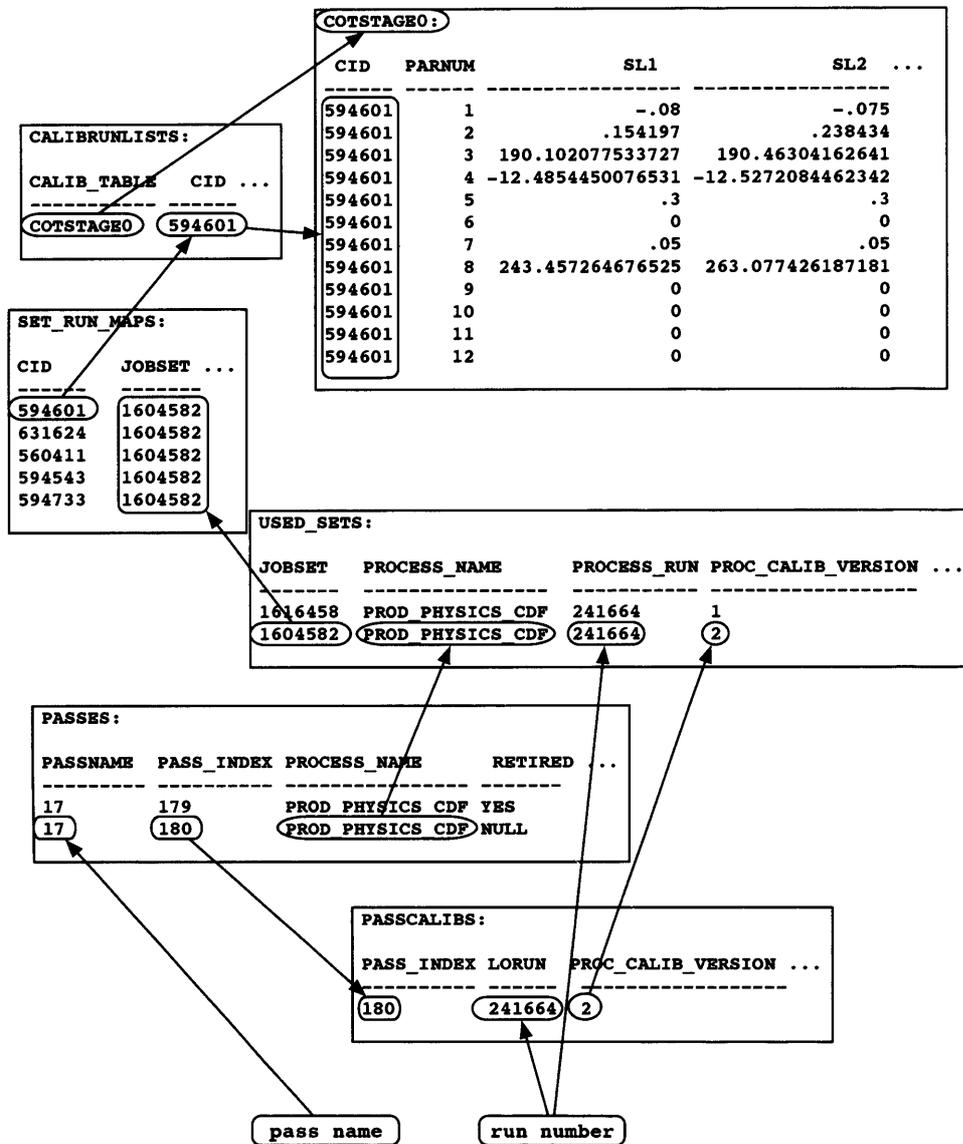
Figure 3.1: *Calibration database schema showing the relevant tables to retrieve the calibrations from the* COTSTAGE0 *table as an example.*

interface to a set of calibrations for a given run is provided, with the user only specifying the run number and the pass name of the required calibration set. The database schema linking a run number and pass name to a unique set of calibrations is shown in figure 3.1, using the COTSTAGEO table, which contains the drift fit values for the COT calibrations described in section 2.4.2, as an example. Only table fields relevant to the schema structure are shown. The five intermediate tables used for the retrieval of the COTSTAGEO calibration table, one of the 104 calibration tables identified by a given pass name, are described below.

PASSES associates a given PASSNAME with a PROCESS_NAME (PROD_PHYSICS_CDF) and a pass number, the PASS_INDEX. Each PASSNAME defines a pass and, as it may be associated with more than one PASS_INDEX value, has a RETIRED field set to 'YES' for all passes except the current pass, which has the default 'NULL' value. The PASSNAME requested by the general user (in this example '17') uniquely identifies the PASS_INDEX (180) for the current pass. It is sometimes necessary to update the calibrations in a pass and a new PASS_INDEX for a given PASSNAME is created by updating the RETIRED field to 'YES' in the current row and creating a new row.

PASSCALIBS associates a given run number (241664), the LORUN, with a version number (2), the PROC_CALIB_VERSION, for the PASS_INDEX specified by the PASSES table.

USED_SETS associates a JOBSET number (1604582) with the PROCESS_NAME given by the PASSES table, and the LORUN and PROC_CALIB_VERSION given by the PASSCALIBS table.

SET_RUN_MAPS associates the JOBSET with a set of CID numbers, each identify-

ing an individual calibration table. This allows the grouping of individual calibration tables by using a common JOBSET number.

CALIBRUNLISTS associates the CID (594601) with the table name (COTSTAGE0), in the CALIB_TABLE field. It is often necessary to combine two sets of calibration tables, both grouped by a common JOBSET number in the SET_RUN_MAPS table, into a new grouping with a new common JOBSET number. The CREATE_DATE field (not shown), allows the most recent instance of two identical CALIB_TABLE names to be included in the new combined set.

COTSTAGE0 and all the other tables containing calibration values are identified by the CALIB_TABLE name. The CID specifies a specific instance of the type of calibrations stored in the table. For COTSTAGE0, each row contains one of the 12 parameters associated with the drift model for each of the 8 COT superlayers described in section 2.4.2.

3.3   Offline procedure for calibration

For each run the calibration CIDs are grouped by a common JOBSET number in the SET_RUN_MAPS table, with the PROCESS_NAME of PROD_PHYSICS_CDF, in the USED_SETS table. As the production of reconstructed events for analyses rely on these calibrations, a robust procedure that is automated where possible is essential to ensure efficient availability of reconstructed data. The calibrations are merged at different stages into intermediate passes of PROD_PHYSICS_CDF. The pass evolution, with the calibrations relevant to this analysis, are shown in figure 3.2.
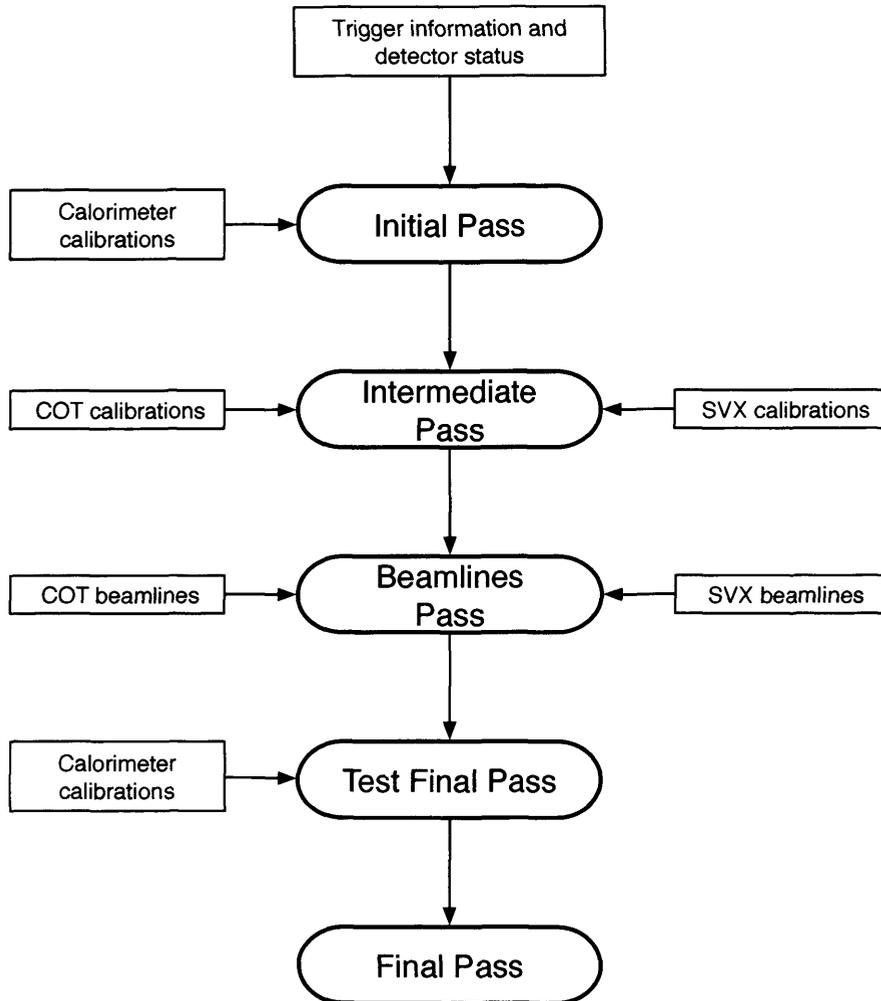
Figure 3.2: *Pass evolution with calibrations used in this analysis.*

A key aspect of a robust system is a modular approach and the availability of software tools. Automated and helper tools for creating and monitoring calibrations are built from generic modular functions that interface with the database.

This provides an interface that is easily adapted to changing database schema and procedures, and greatly reduces software based errors, and testing and validation time.

Due to the different types of calibrations described in section 3.1 and their production timescale, several intermediate passes are made before the set is complete. To ensure efficient availability, the intermediate stages are created automatically when the necessary tables become available, independent of the status of other runs.

The first version of **PROD_PHYSICS_CDF** is made from merging all available calibrations, such as those from the trigger system, when the run ends. This is put into the 'initial pass' which is used for preliminary studies.

The calibrations for the tracking subdetectors described in section 2.4 are produced using multiple runs. They are merged and put into the 'intermediate pass' when they become available, typically within 24 hours of the run ending. The beam positions, described in section 3.1, are produced once the intermediate pass is available. They are merged and put into the 'beamlines pass', typically within 36 hours of the run ending.

The 'final pass' is used for the full offline production of data for analyses. The tables added at this stage are made from analysing reconstructed data collected over the previous few months such as the CEM calorimeter calibrations described in section 2.5.1. Before the final pass is created, a 'test pass' is created and checked extensively over a period of a few weeks.

3.4 Monitoring and validating calibrations

Monitoring the status of calibrations is an essential aspect of calibration production. This is done automatically until the final pass is available. For passes not available within the specified timescales, the presence of the necessary tables is checked and the relevant expert emailed.

For manual validation of calibrations, a tool to compare channels in different JOBSETs is used. Details of channels common to both JOBSETs with different CID numbers are provided, optionally including channels present in only one JOBSET. In addition to individual JOBSETs, comparisons between a pass and either another pass or the latest version are also possible. This will quickly confirm whether a newly created pass contains the most recent calibrations or whether certain calibrations have been successfully updated leaving the others unchanged. As the pass is unavailable whilst values are being changed, this tool allows the down time to be kept to a minimum whilst providing rigorous validation.

Chapter 4

Event selection and

reconstruction

This measurement of Γ_W is made in the W $\rightarrow$ eν and W $\rightarrow$ $\mu\nu$ decay channels using data with an integrated luminosity of 370 pb^{-1} and 330 pb^{-1} respectively, collected at CDF between February 2002 and August 2004. The Z $\rightarrow$ ee and Z $\rightarrow$ $\mu\mu$ decay channels, where the opposite charge of the lepton pair is implied, provide a high-purity event sample and are used extensively to calibrate the simulation. The large W and Z boson masses result in decay products with large transverse momenta. The presence of a neutrino, whose direct detection at CDF is not possible, is inferred from missing transverse energy. W boson candidate events contain a high p_T electron or muon and large missing transverse energy, and Z boson candidate events contain two high p_T electrons or muons with opposite charge. Electron and muon candidates with tracks traversing the COT are required to extrapolate to the CEM energy deposits and muon chamber hits respectively.

Events at CDF are fully reconstructed offline from raw data using the latest calibrations described in chapter 3. The selection and reconstruction of objects used in this analysis is described below.

4.1 Electron selection

Electrons are identified by matching COT tracks with energy deposited in the CEM using the position provided by the CES. The requirements met by an electron candidate are detailed below.

Energy reconstruction

Energy deposited by an electron traversing the CEM is not always contained in a single tower. Similar to the L3 electron clustering, described in section 2.8.2, CEM energy deposits are recursively grouped by adding the unclustered tower with highest E_T to the unclustered neighbouring tower in the same wedge with the highest E_T. Energy deposited in the CES, described in section 2.5.1, is also clustered to provide the shower position measurement.

Calorimeter requirements

To ensure the electromagnetic shower is contained in a well instrumented region of the calorimeter, the shower is required to be in a 'fiducial' region. Candidate electrons with shower leakage into the gap at $|z| < 4.2$ cm, where the two halves of the calorimeter meet, are excluded by requiring the distance (z_{ces}) in the z direction between the CES shower position and $z = 0$ to be greater than 12 cm.

Additionally, the distance (x_{ces}) from the wedge center, perpendicular to the z direction in the CES plane, is required to be less than 18 cm to minimise shower leakage into the gap where the calorimeter wedges meet 23.1 cm from the wedge centre.

Since electrons deposit most of their energy in the electromagnetic calorimeter, E_{had}/E_{em} of electron candidates is required to be less than 0.07. Electron candidates are required to be in the first 9 towers (towers 0 to 8) from $z = 0$ as those furthest from the centre on either side have greater energy leakage into the hadronic calorimeter.

In addition to energy deposited in the tower containing the candidate electron, energy is also deposited in the two neighbouring towers in the same wedge. This 'energy profile' of candidate electrons can be compared to that of electrons from test beams using the parameterisation [44]

$$L_{shr} = 0.14 \sum^{\text{cluster towers } i} \frac{E_i - E_i^{\text{expected}}}{\sqrt{(0.14\sqrt{E_i})^2 + (\Delta E_i^{\text{expected}})^2}} \tag{4.1}$$

where E_i is the measured tower energy in the neighbouring tower, E_i^{expected} is the expected energy in that tower, measured from test beam data, and $\Delta E_i^{\text{expected}}$ is the measured fluctuation of the latter. Electromagnetic clusters with L_{shr} less than 0.3 are considered consistent with electrons and therefore required for electron candidates.

Track requirements

Individual COT hits and the beam position, obtained from reconstructed vertices, are fitted with a helix to provide a 'beam constrained' track. The number of axial and stereo COT superlayers with at least 7 hits (N^{axial} and N^{stereo} respectively) is required to be at least 3. The p_{T} of the beam constrained track is calculated from the helix curvature and the magnetic field strength, and is required to be greater than 9 GeV. The track impact parameter in the z direction (z_0) is required to be less than 60 cm from the detector center. Neglecting the electron rest mass, the true p_{T} and E_{T} are equal, so electron candidates are required to have a cluster E_{T} between 0.8 and 1.3 times the track p_{T}, although this requirement is relaxed in studies to measure parameters for the detector simulation described in chapter 6.

Tracks are extrapolated to the plane of the CES to match a track with a cluster. The CES track position is required to be less than 8 cm from the CES cluster position in the z direction (Δz), and less than 10 cm in the perpendicular direction in the CES plane (Δx).

The full requirements of electron candidates are summarised in table 4.1.

4.2 Muon selection

An event containing a muon is identified by a track in the muon drift chamber matching a track in the COT, and energy deposits in the calorimeter consistent with a muon.

E_T	> 25 GeV
p_T	> 9 GeV
$|z_0|$	< 60 cm
$|x_{ces}|$	< 18 cm
$|z_{ces}|$	> 12 cm
E_T/p_T	> 0.8 and < 1.3
E_{had}/E_{em}	< 0.07
L_{shr}	< 0.3
$|\Delta z|$	< 8 cm
$|\Delta x|$	< 10 cm
N^{axial}	≥ 3 SL with ≥ 7 hits/SL
N^{stereo}	≥ 3 SL with ≥ 7 hits/SL

Table 4.1: *Requirements for electron candidates.*

Track requirements

The total energy of the muon cannot be measured as the muon passes through the entire detector without coming to rest. The muon p_T is determined from the curvature of the helix fit to the COT hits and the beam position. Each muon candidate track is required to have at least 7 hits in 3 axial and 3 stereo COT superlayers. To allow an accurate measurement of the track impact parameter in the xy plane (d_0), hits are required in the silicon detector when operational otherwise the number of hits in the first COT superlayer ($N_{sl=1}^{hits}$) is required to be at least 5. To ensure the track traverses all 8 superlayers, the radius at which the track crosses the COT end-plate (r_{cot}) is required to be greater than 137 cm, the outer radius of the COT. The track impact parameter in the z direction is required to be less than 60 cm from the detector center and the track d_0 is required to be less than 0.04 cm from the detector center for tracks with silicon hits and less then 0.2 cm for those without. Candidate muon track are required to have a good helix fit by demanding the χ^2_{track}/ndf to be less than 3 for tracks with silicon and less than 2 for tracks without, where ndf $= N_{cot}^{hits} - 5$ where 5 is

the number of free parameters in the helix fit.

Cosmic muon rejection

High energy 'cosmic' muons from space are constantly passing through the CDF detector, and are excluded from candidate muon events. Many of these cosmic muons meet the muon selection requirements, and can either mimic a Z boson event if both the incoming and outgoing tracks are reconstructed or a W boson event if only the incoming or outgoing track is reconstructed. The cosmic muon tagging algorithm performs a helix fit to the track hits with a floating global time offset for all hits included. The hits are fitted twice, with an outgoing and an incoming (time reversed) hypothesis. The fit with the lowest $\chi^2_{\text{track}}/\text{ndf}$ determines the track direction. Hits in the opposite side of the detector in the region extrapolated to by the first refitted track are also fitted in the same way and are included in a single helix fit to both tracks, again with a global time offset. The colinearity of the two fits is ensured by requiring the azimuthal angle ($\Delta\phi_{\mu\mu}$) between the tracks to be greater than 3.13 and the sum of the track rapidity values ($\sum \eta_{\mu\mu}$) to be less than 0.03. Events with individual fits consistent with a colinear incoming-outgoing hypothesis and a combined fit with χ^2 less then 300 are tagged as cosmic muons and rejected from the candidate events.

Calorimeter requirements

To ensure the calorimeter deposits are consistent with a muon, the wedge traversed by the extrapolated track is required to have less than 2 GeV deposited in the electromagnetic calorimeter and less than $5.6 + 0.014 \times p_{\text{T}}$ GeV in the

hadronic calorimeter. The latter requirement ensures a p_T independent selection efficiency, described in section 6.5.4.

The track and calorimeter requirements for muon candidates are summarised in table 4.2.

p_T^{bc}	> 25 GeV
$|z_0|$	< 60 cm
silicon hits	when silicon is 'good'
N^{axial}	≥ 3 with ≥ 7 hits/SL
N^{stereo}	≥ 3 with ≥ 7 hits/SL
$N^{hits}_{sl=1}$	≥ 5 (no silicon tracks only)
r_{cot}	> 137 cm
d_0	$< 0.04(0.2)$ cm for silicon(no silicon)
E_{em}	< 2 GeV
E_{had}	$< 5.6 + 0.014 \times p_T$ GeV
$\chi^2_{track}/\text{ndf}$	$< 3(2)$ for silicon(no silicon)
cosmic	not true

Table 4.2: *Track and calorimeter requirements for muon candidates.*

Muon chamber requirements

In addition to the track and calorimeter requirements described above and listed in table 4.2, candidate muons have the stub requirements described below. To ensure the muon passes through a fiducial region of the muon chamber, the helix of the COT fit is propagated through a simulation of the muon chamber geometry. This determines the minimum distance from the cell boundaries in the x and z directions in local chamber coordinates, which correspond to the perpendicular and parallel directions to the drift wire in the chamber plane respectively. The muon chamber hits and the extrapolated COT track are in a fiducial region if they are within the chamber in the local x direction and more than 3 cm within the chamber in the local z direction. The distance between the COT

track extrapolated to the muon chambers and the reconstructed muon chamber track is required to be within 3, 6 or 5 cm in the local x direction for the CMU, CMP and CMX chamber respectively (Δx_{cmu}, Δx_{cmp} and Δx_{cmx} respectively). These requirements are listed in table 4.3, where a CMUP stub has hits in both the CMU and CMP chambers.

CMUP or CMX stub	present
$|\Delta x_{\mathrm{cmp}}|$	< 6 cm
$|\Delta x_{\mathrm{cmu}}|$	< 3 cm
$|\Delta x_{\mathrm{cmx}}|$	< 5 cm
fiducial	true

Table 4.3: *Stub requirements for muon candidates.*

4.3 Recoil reconstruction

In addition to energy deposited by high p_{T} leptons, there are three other sources of calorimeter activity in candidate W and Z boson events at CDF:

Initial state QCD radiation, where quarks and gluons are radiated from the two partons participating in the hard scatter, described in section 1.2. This results in calorimeter activity that is strongly correlated with boson $\vec{p_{\mathrm{T}}}$.

Spectator parton radiation, where remnant partons from the broken interacting p$\bar{\mathrm{p}}$ undergo QCD interactions to produce hadrons. Most of the energy flow is at low angle and subsequently undetected, and the detected energy is largely uncorrelated with luminosity and boson $\vec{p_{\mathrm{T}}}$.

Additional proton-antiproton (minimum bias) interactions, where energy from interactions between other p$\bar{\mathrm{p}}$s in the beam is deposited in the

calorimeters. This results in calorimeter activity that is strongly correlated with luminosity and uniformly distributed in azimuthal angle.

All calorimeter activity not associated with the lepton is collectively referred to as the recoil, with a 'hard' component from QCD radiation from the boson production, and a 'soft' component from the spectator parton interactions and minimum bias events.

The towers surrounding the lepton tower contain energy from final state photon radiation and lepton bremsstrahlung radiation, as well as leakage of the electromagnetic shower. To exclude energy associated with the lepton from the recoil, a 'knockout region' of towers surrounding the lepton is removed from the recoil sum. The knockout region is chosen to maximises both the inclusion of energy associated with the lepton and the exclusion of energy associated with the recoil.

Although the tower with the lepton CES shower position contains most of the deposited lepton energy, there is considerable leakage of the electromagnetic shower into the adjacent tower in the same wedge nearest the CES shower position. For electrons, these two towers are identified by the electron clustering algorithm and used in the electron energy reconstruction. However, there is additional shower leakage into the other neighbouring towers, predominantly into the tower in the adjacent wedge nearest the shower CES position. The knockout region is therefore defined relative to the direction of the two neighbouring towers nearest the shower CES position, defined as the ϕ_{ces} and η_{ces} directions.

The knockout region, centered on the highest energy tower, is shown in figure 4.1 for candidate electrons and muons, together with the average energy deposited in each neighbouring tower in the electromagnetic and hadronic calorimeter.
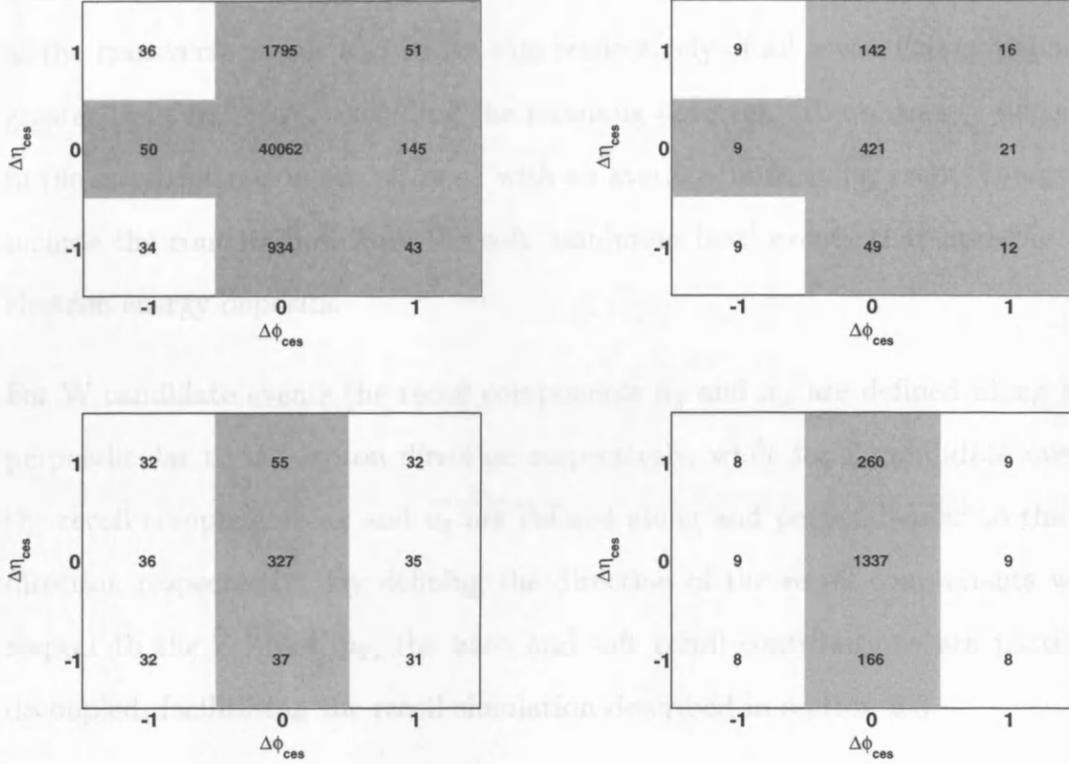
Figure 4.1: *The average energy deposited in MeV in the tower containing the CES shower position and the neighbouring towers for the (left) electromagnetic and (right) hadronic calorimeter for (top) electron candidates in* $W \to e\nu$ *events and (bottom) muon candidates in* $W \to \mu\nu$ *events.* $\Delta\eta_{ces} = +1$ *and* $\Delta\phi_{ces} = +1$ *denote the nearest tower to the shower CES position in the same wedge and the adjacent wedge respectively. The shaded region is the knockout region.*

Since both adjacent towers in the same wedge contain significant energy leakage they are included in the knockout region. Additionally, for electrons, the three towers in the adjacent wedge nearest the CES shower position as well as the neighbouring tower in the opposite adjacent wedge also contain significant leakage energy, together with wide angle photons radiated by the electron, and are also included in the electron knockout region.

91

The recoil energy vector ($\vec{u}$) and total transverse energy sum (ΣE_T) are defined as the transverse vector and scalar sum respectively of all tower energy deposits greater than 100 MeV, excluding the miniplug detector. Tower energy deposits in the knockout region are replaced with an average 'underlying event' energy to include the contribution from the soft 'minimum bias' events that underlie the electron energy deposits.

For W candidate events the recoil components $u_\parallel$ and $u_\perp$ are defined along and perpendicular to the lepton direction respectively, while for Z candidate events the recoil components u_1 and u_2 are defined along and perpendicular to the p_T^Z direction respectively. By defining the direction of the recoil components with respect to the Z boson p_T, the hard and soft recoil contributions are partially decoupled, facilitating the recoil simulation described in section 6.6.

The underlying event energy is estimated by sampling a 7 tower region at the same η and with $\Delta\phi = 90°$ from the lepton knockout region in W $\rightarrow$ eν candidate events. For consistency with the recoil definition, only towers with energy deposits greater than 100 MeV are included in the average. The average tower energy is found to be 33 MeV for the electromagnetic calorimeter and 9 MeV for the hadronic calorimeter for both electron and muon candidates.

The underlying event energy has a hard and a soft contribution. The hard contribution has the dependence on $u_\parallel$ shown in figure 4.2 (left), being largest when $u_\parallel$ is largest as the recoil is along the lepton direction. The soft contribution has the luminosity dependence shown in figure 4.2 (right) as the number of minimum-bias events increases with luminosity.
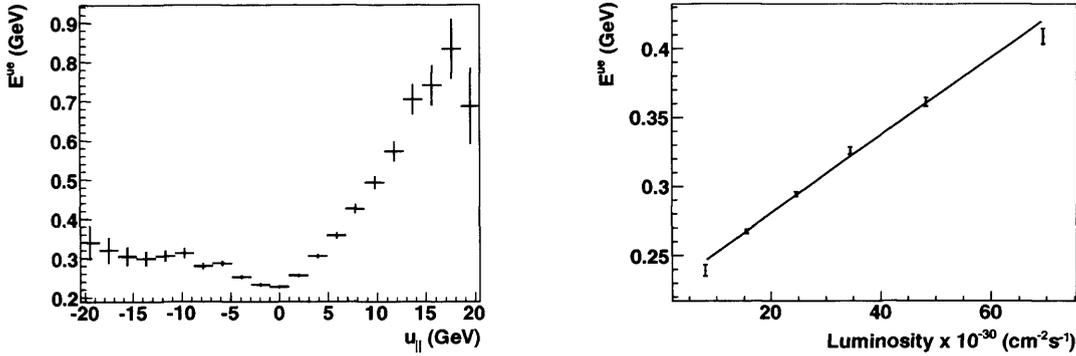
Figure 4.2: *Underlying event energy dependence the recoil component parallel to the lepton direction ($u_{\parallel}$), and luminosity, in* $\mathrm{W} \to e\nu$ *candidate events.*
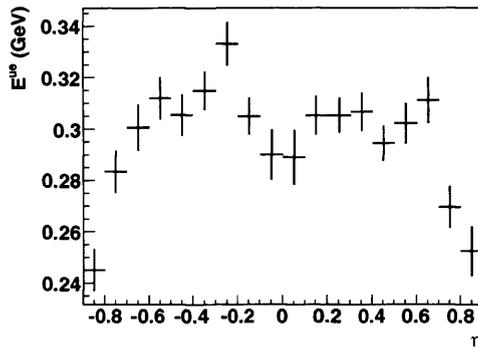
Figure 4.3: *The distribution of the average underlying event energy per tower as a function of lepton tower η. The energy is measured in a 7 tower region in the electromagnetic calorimeter, with a tower threshold of 100 MeV, in* $\mathrm{W} \to e\nu$ *candidate events.*

The underlying event energy also has a dependence on lepton η, shown in figure 4.3. For the recoil reconstruction, the underlying event energy is added back into each tower in the knockout region with the $u_{\parallel}$ and lepton η dependence obtained from sampling the distributions in figure 4.2 (left) and 4.3 respectively, and with the luminosity dependence obtained from the linear fit to the distribution in figure 4.2 (right).

4.4 Boson mass reconstruction

As the leptons used in this analysis to reconstruct the boson mass are highly relativistic, with a Lorentz factor greater than 240, their rest masses can be neglected. For muon candidates, the track momentum is used to calculate the invariant mass. For electron candidates the calorimeter energy ($\vec{E}$) is used, as it is known with greater accuracy than the track momentum, with the direction determined from the CES shower position and the track vertex.

4.4.1 W boson m_{T} reconstruction

The neutrino is not detected at CDF so its momentum cannot be directly reconstructed. Since there is energy flow, particularly from spectator parton QCD interactions, through uninstrumented regions at large rapidity, the only estimate of the neutrino momentum is the missing energy in the transverse plane ($\vec{\slashed{E}}_{\mathrm{T}}$), defined as

$$\vec{\slashed{E}}_{\mathrm{T}} = -(\vec{E}_{\mathrm{T}} + \vec{u}) \tag{4.2}$$

where $\vec{u}$ is the recoil vector described in section 4.3. For W $\rightarrow \mu\nu$ events, the muon $\vec{p_{\mathrm{T}}}$ is substituted for $\vec{E}_{\mathrm{T}}$.

For W boson candidate events, the mass in the transverse plane is reconstructed with equation 1.21 using $\vec{\slashed{E}}_{\mathrm{T}}$ for the neutrino transverse momentum and $\vec{E}_{\mathrm{T}}$ ($\vec{p_{\mathrm{T}}}$) for the lepton transverse momentum in W $\rightarrow$ eν (W $\rightarrow \mu\nu$) events.

4.4.2 Z boson mass reconstruction

The invariant mass is calculated using equation 1.20. In Z → $\mu\mu$ candidate events the invariant mass ($m_{\mu\mu}$) is calculated for the two highest p_T muon candidates using the muon $\vec{p_T}$. In Z → ee candidate events, the invariant mass (m_{ee}) is calculated for the two highest E_T electron candidates using the electron $\vec{E_T}$.

4.5 Boson selection

In addition to W boson candidate events selected for the measurement of Γ_W, Z bosons candidate events are selected with high purity and with a fully reconstructed boson mass. This facilitates the tuning of the event and detector simulation, described in chapters 5 and 6 respectively, and the determination of the background event distributions described in chapter 7, together with their associated systematic uncertainties.

Both W and Z boson candidate events are required to have a recoil magnitude ($|u|$) less than 20 GeV to reduce QCD background events in W candidate events, described in section 7.3. However, for Z boson candidates used in the boson p_T and recoil studies described in sections 5.2 and 6.6 respectively, the recoil requirement is replaced with a Z boson p_T (p_T^Z) requirement of less than 50 GeV.

W boson selection

W boson candidate events are single lepton events with $\not{E}_T$ greater than 25 GeV and no additional high p_T track with opposite charge. The latter 'Z veto' require-

ment rejects events that contain a Z boson where one of the leptons traverses a gap in the calorimeter or muon chamber.

p_T	> 20 GeV
Δz_0	< 5 cm
COT hits	present
opposite sign	true
W $\rightarrow$ eν candidates	
$\sum^{\Delta R < 0.4} p_T$	< 5 GeV
$|x_{\text{ces}}|$	> 18 cm
$|z_{\text{ces}}|$	< 9 cm
W $\rightarrow$ $\mu\nu$ candidates	
cosmic	not true
	and
$\sum^{\Delta R < 0.4} p_T$	< 10 GeV
	or
$\sum^{\Delta R < 0.4} p_T$	< 2 GeV
E_{em}	< 2 GeV
E_{had}	$< 5.6 + 0.014 \times p_T$ GeV

Table 4.4: *Z veto requirements for additional track.*

Z veto events have an additional track with COT hits, a p_T greater than 20 GeV, a distance between z_0 and that of the candidate track (Δz_0) less than 5 cm and no additional high p_T tracks nearby. The latter 'track isolation' requirement is met by demanding the p_T sum of all other tracks within a cone of $\Delta R = \sqrt{(\Delta\eta)^2 + (\Delta\phi)^2} = 0.4$ with Δz_0 less than 5 cm ($\sum^{\Delta R < 0.4} p_T$) to be less than 5 GeV for W $\rightarrow$ eν candidate events. For W $\rightarrow$ $\mu\nu$ candidate events, $\sum^{\Delta R < 0.4} p_T$ is required to be either less than 10 GeV if the calorimeter energy deposits are consistent with a muon or less than 2 GeV otherwise. These requirements are listed in table 4.4 and the requirements for W boson candidate events are listed in table 4.5.

The m_T distributions of the 108,808 W $\rightarrow$ eν candidate events and 127,432 W $\rightarrow$ $\mu\nu$ candidate events are used to measure the W boson decay width, described in

96

$\not{E}_T$	> 25 GeV
m_T	> 50 GeV and < 200 GeV
$|u|$	< 20 GeV
Z veto	false

Table 4.5: *W boson requirements.*

chapter 8.

4.5.1   Z boson selection

The yield of Z → $\mu\mu$ candidate events is increased without significant loss of purity, by requiring only a single 'tight' muon candidate which meets the full requirements listed in section 4.2. The other 'loose' muon candidate is required to meet only the track and calorimeter requirements listed in table 4.2. The data contain 6267 candidate Z → $\mu\mu$ events and 2903 candidate Z → ee events that meet the requirements listed in table 4.6.

$m_{\ell\ell}$	> 80 GeV and < 100 GeV
Lepton charge	Opposite sign
Recoil	< 20 GeV

Table 4.6: *Z boson requirements.*

Chapter 5

Event generation

The m_T distribution of W bosons has a Breit-Wigner component, from the propagator lifetime described in section 1.3, and a Gaussian component from the finite resolution of the detector. The Gaussian resolution component decreases faster with m_T than the Breit-Wigner component, rendering the high m_T region sensitive to Γ_W, shown in figure 1.11. Thus a measurement of Γ_W can be extracted by comparing the simulated m_T distribution to data in the high m_T region, after normalisation in the central region. This method was also used in the previous CDF measurement of Γ_W [23].

The simulation of the m_T distribution has three components; the event generation, described in this chapter, the detector simulation, described in chapter 6 and the simulation of the fraction and m_T distribution of 'background' processes that contaminate the candidate events, described in chapter 7.

The estimation of the systematic uncertainties associated with the event simulation, summarised in section 8.1, are also described, and are taken as the deviation

of the measured value of Γ_W when the particular simulation method is varied by an amount representing the 1σ confidence level. This is achieved by generating two sets of simulated 'pseudo-data', one with the standard parameterisation and the other with a change representing the 1σ deviation. The simulated m_T distribution is fitted to the two sets of pseudo-data to determine the shift in Γ_W.

The simulated m_T distribution is fitted to that of candidate events in the region $m_T^{\text{fit}} < m_T < 200$ GeV, and normalised in the region $50 < m_T < m_T^{\text{fit}}$ GeV. The value (m_T^{fit}) of the lower bound of the fit region affects the size of the systematic and statistical uncertainty associated with the measurement of Γ_W. Specifically, the larger the value of m_T^{fit}, the smaller the systematic uncertainty and the larger the statistical uncertainty. The systematic uncertainties are estimated for m_T^{fit} values of 80, 85, 90, 100, 110 GeV. The value of m_T^{fit} that minimises the combined systematic and statistical uncertainty is evaluated in section 8.1.

The Drell-Yan boson production process, described in section 1.2, has three components that need to be simulated; the QCD effects of the interacting partons (the PDFs and boson p_T), the QED radiative effects on the boson and final state leptons, and the decay kinematics of the boson (including the boson p_T and polarisation dependence). Since a combined NNLO calculation of the QCD and QED effects is not available, a leading-order event generator is used with NLO PDFs and NLO QED radiative corrections. A separate NLO calculation of $\frac{d\sigma^W}{dp_T}$ is used to simulated the QCD effects resulting in a non-zero boson p_T. This chapter describes the event generation and the associated systematic uncertainties.

5.1 Event generation

The simulated m_T distributions of W $\to$ eν and W $\to$ $\mu\nu$ events require a large number of events in the high m_T region to minimise the statistical uncertainty. To facilitate this, a weighted event generator is used and events are generated with a flat $\sqrt{\hat{s}}$ distribution in the high m_T region and reweighted to the Breit-Wigner distribution using equation 1.24. A leading-order 'Born level' Monte Carlo (MC) event generator is used to generate W $\to$ $\mu\nu$, W $\to$ eν, Z $\to$ ee and Z $\to$ $\mu\mu$ events with zero boson p_T using the CTEQ6M [45] PDFs according to equations 1.22 and 1.24. The scale is taken as the centre-of-mass energy ($Q = \sqrt{\hat{s}}$). The Berends and Kleiss (BK) [46, 47] algorithm is used to calculate the affect of a radiated photon, with the Feynman diagrams shown figure 1.3 for W bosons, and a virtual photon, with the Feynman diagrams shown in figure 1.4.

5.1.1 Electroweak corrections and uncertainties

The uncertainty on Γ_W from higher order contributions to final state QED radiation, not included in the BK calculation, is estimated by comparing the value of Γ_W obtained by using the PHOTOS [48, 49] event generator in the single photon mode and the two photon mode. In addition to the direct effect on Γ_W from generating an additional photon, there is an indirect effect on the $m_{\ell\ell}$ distributions in Z boson events from the subsequent change in the values for the calorimeter response (S^{cem}) and resolution (κ), described in section 6.4, and the tracking response (S^{mom}) and resolution (S^{res}) described in section 6.3. The change in Γ_W from the new response and resolution values are added to the change in Γ_W when using PHOTOS with an additional photon (denoted $1\gamma \to 2\gamma$), shown in table 5.1

for W $\to$ eν events and table 5.1 for W $\to$ $\mu\nu$ events.

$m_{\mathrm{T}}^{\mathrm{fit}}$	$1\gamma \to 2\gamma$	S^{cem}	κ	total
80	-17	$+9$	-7	15
85	-15	$+8$	-6	13
90	-9	$+5$	-4	8
100	-0.2	$+2$	-1	1
110	-2	$+1$	0	1

Table 5.1: *Systematic uncertainties for* W $\to$ eν *events, in MeV, from final state QED radiation.*

$m_{\mathrm{T}}^{\mathrm{fit}}$	$1\gamma \to 2\gamma$	S^{mom}	S^{res}	total
80	-10	$+28$	-14	4
85	-10	$+26$	-13	3
90	-7	$+16$	-10	1
100	-3	$+7.6$	-5.4	1
110	-1	$+4.8$	-2.4	1

Table 5.2: *Systematic uncertainties for* W $\to$ $\mu\nu$ *events, in MeV, from final state QED radiation.*

In addition to final state QED radiation, higher-order 'non-resonant' electroweak corrections to the LO cross-section, dominated by the 'box' diagrams shown in figure 5.1, have an effect on the m_{T} distribution, particularly in the high m_{T} region [50].
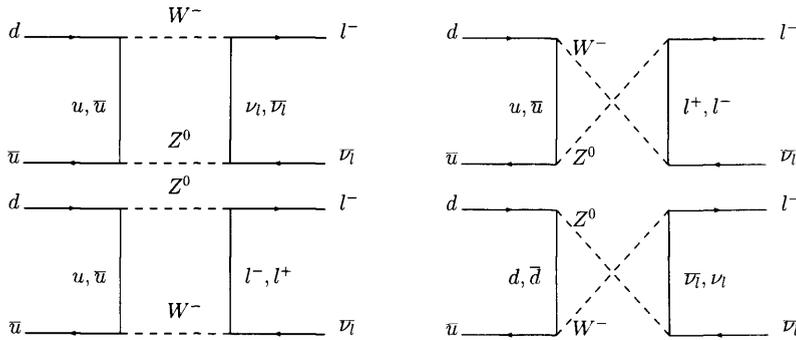
Figure 5.1: *Feynman diagram for non-resonant 'box' electroweak contributions to leading order W boson production.*

The effect of non-resonant electroweak correction on the m_T tail region is estimated using the WGRAD event generator [50]. A simplified detector simulation is used, and $\not{E}_T$ is parameterised using a linear response and Gaussian resolution, obtained from fits to the standard simulation. The fractional change S^{ewk} in the WGRAD m_T distribution from including non-resonant correction is

$$S^{ewk} = \begin{cases} 0.9986 & \text{for } m_T < 90\,\text{GeV} \\ 1.020 - 2.2 \times 10^{-4} \times m_T & \text{for } m_T > 90\,\text{GeV} \end{cases} \tag{5.1}$$

for $W \to e\nu$ events, shown in figure 5.2 (left), and

$$S^{ewk} = \begin{cases} 1.0026 - 3.9 \times 10^{-5} \times m_T & \text{for } m_T < 95\,\text{GeV} \\ 1.025 - 2.7 \times 10^{-3} \times m_T & \text{for } m_T > 95\,\text{GeV} \end{cases} \tag{5.2}$$

for $W \to \mu\nu$ events, shown in figure 5.2 (right).
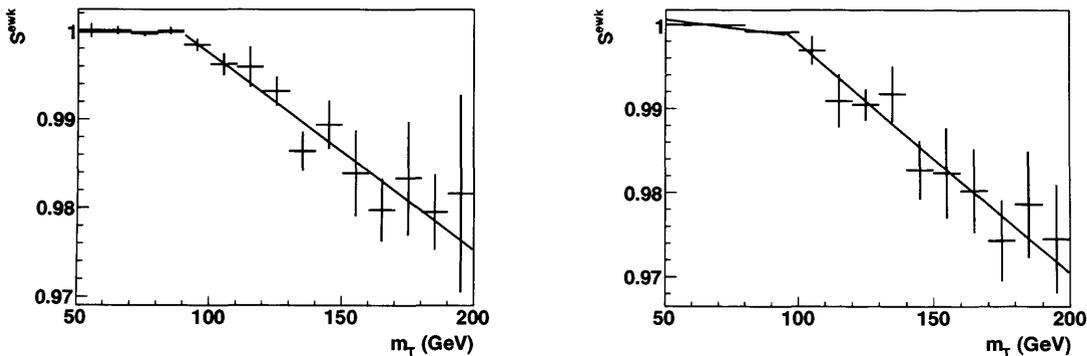
Figure 5.2: *Fractional change S^{ewk} in the m_T distribution when including non-resonant contributions using* WGRAD *for (left)* $W \to e\nu$ *and (right)* $\mu\nu$ *events.*

The shift in the measurement of Γ_W, shown in table 5.3, is added to the fitted value of Γ_W presented in chapter 8. The associated uncertainty is estimated as the change in the value of Γ_W from varying the Gaussian $\not{E}_T$ smearing by an amount

equivalent to the uncertainty on the resolution of the recoil model described in section 6.6.

m_T^{fit}	$W \to e\nu$ correction	$W \to e\nu$ uncertainty	$W \to \mu\nu$ correction	$W \to \mu\nu$ uncertainty
80	8	2	11	2
85	10	5	12	5
90	11	6	12	6
100	15	6	17	6
110	20	6	23	6

Table 5.3: *The correction to Γ_W and the associated systematic uncertainty, in MeV, from non-resonant electroweak corrections.*

The combined systematic uncertainty on Γ_W from higher order electroweak corrections, shown in table 8.1, is obtained by adding the QED and the non-resonant systematic uncertainties in quadrature.

5.1.2 PDF uncertainty

The CTEQ6M PDFs are defined by 20 orthogonal parameters with values and associated errors obtained by minimising the χ^2 of a fit to experimental data. The change in Γ_W from individually varying each of the parameters by their asymmetric uncertainty corresponding to a 90% confidence level, is obtained by fitting the simulated m_T distribution to pseudo-data simulated using the default values. Figure 5.3 shows the values of Γ_W for each of the PDF parameters for $m_T^{\text{fit}} = 90$ GeV.

The combined uncertainty on Γ_W from the PDF parameter uncertainty is estimated using

$$\Delta\Gamma_W = 0.5 \times \sqrt{\sum^{\text{all parameters}} (\Delta\Gamma_W^i)^2} \qquad (5.3)$$
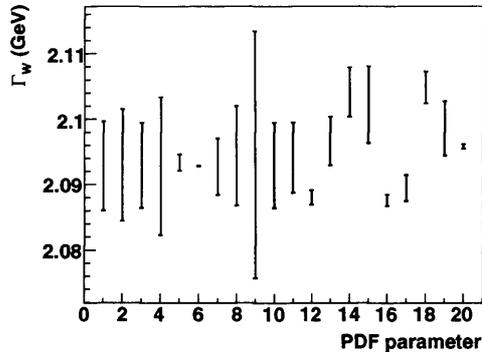
Figure 5.3: *Variation on* Γ_W *obtained by individually varying the* CTEQ6M *PDF parameters by their associated uncertainty for* $m_T^{\text{fit}} = 90$ *GeV.*

where $\Delta\Gamma_W^i$ is the variation on Γ_W from varying PDF parameter i by its 90% confidence level uncertainty. The result is then divided by 1.6 to give the 1σ variations, shown in table 5.4.

m_T^{fit}	$W \rightarrow e\nu$	$W \rightarrow \mu\nu$
80	15	16
85	17	18
90	16	16
100	19	21
110	24	25

Table 5.4: *Systematic uncertainties, in MeV, from varying the* CTEQ6M PDF *parameters.*

The CTEQ6M PDFs used in this analysis are calculated to NLO and are chosen since they provide a more conservative estimate of the uncertainty from the PDF parameters than the MRST 2004 PDFs [17]. As the latter provide PDFs calculated to both NLO and NNLO, the uncertainty on Γ_W from higher order QCD calculations is found by comparing the values of Γ_W obtained using the MRST 2004 NLO and NNLO PDFs, shown in table 5.5 for $W \rightarrow e\nu$ and $W \rightarrow \mu\nu$ events.

The combined systematic uncertainty on Γ_W from the PDFs is shown in table 8.1

104

m_T^{fit}	
80	14
85	14
90	12
100	10
110	9

Table 5.5: *Higher-order QCD systematic uncertainties, in MeV, obtained from comparing the NLO and NNLO* MRST *PDFs.*

and obtained by adding the two uncertainties in quadrature.

5.1.3   W boson mass uncertainty

The uncertainty on Γ_W from the W boson mass value used in the event generator, shown in table 5.6, is found by varying the mass value by its experimental uncertainty of 25 MeV [51] and finding the corresponding shift in the measured value of Γ_W.

m_T^{fit}	
80	18
85	17
90	9
100	4
110	2

Table 5.6: *Systematic uncertainties, in MeV, from the uncertainty on the W mass.*

5.2   Boson transverse momentum

Higher-order production processes result in a non-zero boson p_T, as the p_T of additional partons emitted from the initial states must be balanced. This happens in gluon radiation from the interacting quarks, shown in figure 1.9, and when one

or both of the interacting partons are gluons, shown in figure 1.7. The QCD calculation describing the boson p_T distribution diverges at low energies and a resummation is performed in the divergent region. The Collins-Soper-Sterman (CSS) [52] resummation calculation is used to describe the divergent region, and its transition to the perturbative region at higher p_T values. The Brock-Landry-Nadolsky-Yuan (BLNY) [53] parameterisation of the non-perturbative functional form in the CSS resummation is used.

The Z boson p_T (p_T^Z) distribution can be measured to relatively high precision compared to that of W bosons (p_T^W), since both decay products are fully reconstructed, and can be used to constrain the parameters of the non-perturbative functional form. As W and Z boson production properties are very similar, the ratio $\frac{d\sigma^W}{dp_T} / \frac{d\sigma^Z}{dp_T}$ can be calculated to NLO and is largely insensitive to the non-perturbative functional form and the associated parameter values [54]. The parameters obtained from the p_T^Z distribution can therefore be used to simulate the p_T^W distribution with only a small additional uncertainty incurred.

5.2.1 Z boson transverse momentum

In the CSS resummation, the p_T differential cross-section is obtained from a Fourier integral of the 'form factor' $\tilde{W}_{q\bar{q}}(b, Q, x_1, x_2)$ over impact parameter b, with the scale $Q = 1/b$ taken as the boson p_T. When $b \gtrsim 1$ GeV^{-1} the perturbative calculation of $\tilde{W}_{q\bar{q}}$ diverges so $\tilde{W}_{q\bar{q}}$ is replaced with

$$\tilde{W}_{q\bar{q}}(b) = \tilde{W}_{q\bar{q}}^{\text{pert}}(b_*) \, \tilde{W}_{q\bar{q}}^{\text{NP}}(b) \tag{5.4}$$

where $\tilde{W}_{q\bar{q}}^{\mathrm{pert}}(b_*)$ and $\tilde{W}_{q\bar{q}}^{\mathrm{NP}}(b)$ are the perturbative and non-perturbative form factors respectively. To ensure $\tilde{W}_{q\bar{q}}^{\mathrm{pert}}$ is not evaluated in the divergent region, b_* is defined as

$$b_* = \frac{b}{\sqrt{1 + (b/b_{\mathrm{max}})^2}} \tag{5.5}$$

so that $b_* \approx b$ below b_{max} and $b_* \approx b_{\mathrm{max}}$ above. The value for b_{max} determines the transition from the perturbative to the non-perturbative part and is chosen here to be 0.5 GeV^{-1} for consistency with other studies [53].

The BLNY form for $\tilde{W}_{q\bar{q}}^{\mathrm{NP}}$ is a Gaussian distribution defined as

$$\tilde{W}_{q\bar{q}}^{\mathrm{NP}} = \exp\left(-b^2\left[g_1 + g_2\ln(Q/2Q_0) + g_1g_3\ln(100x_1x_2)\right]\right) \tag{5.6}$$

where $Q_0 = 1.6$ GeV and the BLNY parameters g_1, g_2 and g_3 are determined from experimental data. The value for g_2 is obtained by minimising the χ^2 of the fits to the $p_{\mathrm{T}}^{\mathrm{Z}}$ distribution of Z $\to$ ee and Z $\to$ $\mu\mu$ candidate events. The parameters g_1 and g_3 are not well constrained by data taken at a single $\hat{s}$ value, such as the Z boson data. Instead, the parameter values obtained from low energy Drell-Yan data taken over a range of $\hat{s}$ values are used [53].

The simulated $p_{\mathrm{T}}^{\mathrm{Z}}$ distribution used to obtain g_2 includes the effect of the detector resolution and acceptance, described in chapter 6. As a single fit is made to data with an average rapidity of $|Y| = 0.3$, the $p_{\mathrm{T}}^{\mathrm{Z}}$ dependence on rapidity is simulated using a resummed NLO calculation of $\frac{d\sigma^{\mathrm{Z}}}{dp_{\mathrm{T}}}(\mathrm{Y} = 0.3)/\frac{d^2\sigma^{\mathrm{Z}}}{dYdp_{\mathrm{T}}}$ [55] using the CSS formalism. The contribution of the processes q$\bar{\mathrm{q}}$ $\to$ Zg with an additional real or virtual gluon, and gq $\to$ Zq are included in the perturbative calculation.

To obtain g_2, a parabola is fitted about the minimum values of the χ^2 obtained by varying the g_2 parameter. The best fit values for g_2, with fits shown in figure 5.4,

107

are 0.62 ± 0.08 GeV^2 with $\chi^2 = 50.8/48$ for Z $\rightarrow$ ee and 0.68 ± 0.05 GeV^2

with $\chi^2 = 51.4/48$ for Z $\rightarrow \mu\mu$. Both values are consistent with a single model

describing the true p_T^Z distribution for both decay channels. A combined fit by

minimising the χ^2 from both decay channels gives $g_2 = 0.66 \pm 0.04$ GeV^2 with

$\chi^2 = 102.9/96$ and is used in this analysis. This value is consistent with the

BLNY value of $g_2 = 0.68^{+0.01}_{-0.02}$, obtained using the CTEQ3M PDFs.
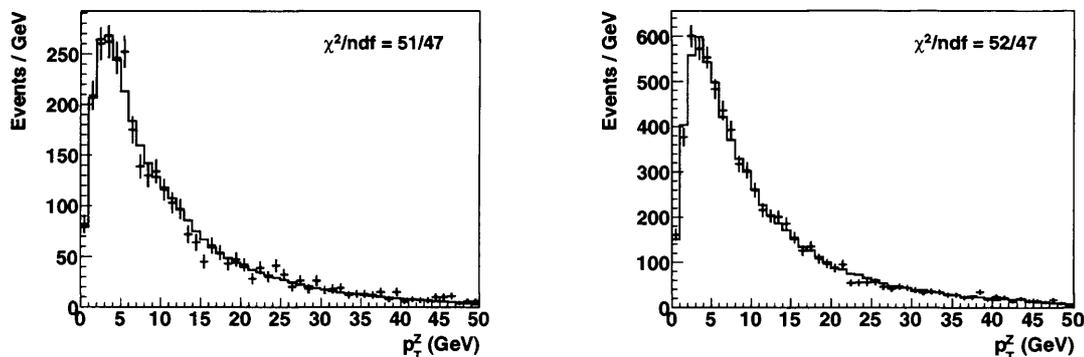
Figure 5.4: *The p_T^Z distributions for Z $\rightarrow$ ee (left) and Z $\rightarrow \mu\mu$ (right) candidate events, fitted to obtain g_2 for the $\tilde{W}_{q\bar{q}}^{NP}$ form factor used in the boson p_T parameterisation.*

The parameter values for the BLNY parameterisation of $\tilde{W}_{q\bar{q}}^{NP}$ used in this analysis

are shown in table 5.7.

g_1	0.21	$\pm$ 0.01	GeV^2
g_2	0.66	$\pm$ 0.04	GeV^2
g_3	-0.06	$\pm$ 0.05	
$b_{\max}$	0.5		GeV^{-1}

Table 5.7: *Parameter values for the $\tilde{W}_{q\bar{q}}^{NP}$ form factor used in the boson p_T parameterisation.*

5.2.2   W boson transverse momentum

To simulate the W boson p_T, a resummed NLO calculation of $\frac{d^3\sigma^W}{dY\,d\hat{s}\,dp_T} / \frac{d^2\sigma^Z}{dY\,dp_T}$ (which is part of the same calculation used for the p_T^Z rapidity dependence mentioned above) is used to model the p_T^W dependence on rapidity and $\hat{s}$. The inclusion of the $\hat{s}$ dependence, shown in figure 5.5 for on-mass and highly virtual W bosons, is necessary because Z bosons in the fit are produced near the Z pole, by requiring $80 < m_{\ell\ell} < 100$ GeV, whereas candidate W bosons are selected in the region $50 < m_T < 200$ GeV. Also the p_T^W cross-section dependence on $\hat{s}$ directly affects the W boson m_T distribution.
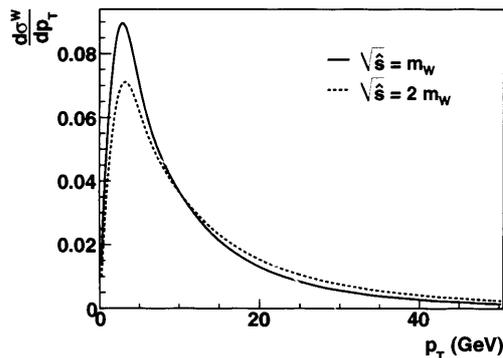
Figure 5.5: $\frac{d\sigma^W}{dp_T}$ for on mass-shell and highly virtual W bosons.

5.2.3   Boson transverse momentum uncertainty

When using the resummed CSS formalism with the BLNY parameterisation constrained by Z boson candidate events to simulate the p_T^W distribution, the estimate of the associated uncertainty has a number of components. These can be grouped into three categories; the uncertainty associated with the global fit values for the BLNY parameters which dominate the differential cross-section at

low p_T^W, the uncertainty in the differential cross-section lineshape over the full p_T^W range, and the uncertainty associated with the calculation of $\frac{d\sigma^Z}{dp_T}(Y = 0.3)/\frac{d^2\sigma^Z}{dY dp_T}$ and $\frac{d^3\sigma^W}{dY d\hat{s} dp_T}/\frac{d^2\sigma^Z}{dY dp_T}$.

Any skewness in the $\frac{d\sigma^Z}{dp_T}$ differential cross-section introduced from the CSS resummation and BLNY parameterisation, in particular from the transition between the non-perturbative to the perturbative region, is estimated by assuming an additional linear p_T dependent 'skew' parameter (B). The true cross-section can then be expressed as

$$\frac{d\sigma^Z}{dp_T} = \left(\frac{d\sigma^Z}{dp_T}\right)_{\text{BLNY}} \times (1 + B \times p_T) \qquad (5.7)$$

where $(\frac{d\sigma^Z}{dp_T})_{\text{BLNY}}$ is the differential cross-section calculated using the CSS resummation with the BLNY parameterisation.

The uncertainty on Γ_W from the BLNY parameter g_2 and the skew parameter B are estimated by simultaneously varying g_2 and B to minimise the χ^2 of the fits to the p_T^Z distribution of Z $\rightarrow$ ee and Z $\rightarrow$ $\mu\mu$ candidate events. The values $g_2 = 0.64$ GeV^2 and $B = -0.0014$ GeV^{-1} are obtained with the covariance matrix

$$\begin{pmatrix} 0.044^2 & -1.38 \times 10^{-7} \\ -1.38 \times 10^{-7} & 0.001^2 \end{pmatrix}$$

which has the corresponding 68% and 95% confidence level contours shown in figure 5.6 together with the BLNY global fit value. The value for g_2 is compatible with the combined fit values used in the simulation, and B is consistent with zero. The distribution of the Γ_W values, obtained by repeatedly sampling the covariance matrix to obtain sets of g_2 and B, are fitted with a Gaussian function and the

110

width is taken as the associated uncertainty on Γ_W, shown in table 5.8.
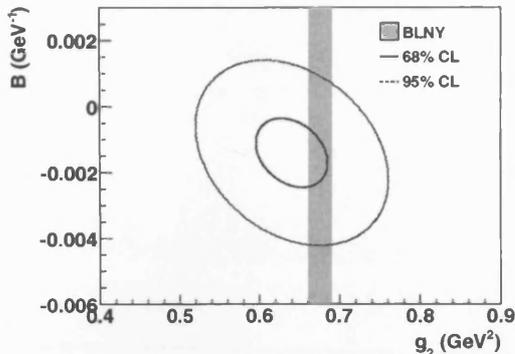
Figure 5.6: *The 68% and 95% confidence level contours for the g_2-B covariance matrix with the shaded region showing the BLNY global fit value for g_2.*

The uncertainty on Γ_W from the associated uncertainty on the g_1 and g_3 BLNY parameters is found by varying the parameter values by their 95% confidence level uncertainty to give the uncertainty on Γ_W shown in table 5.8.

The calculation of $\frac{d\sigma^Z}{dp_T}(Y=0.3)/\frac{d^2\sigma^Z}{dY\,dp_T}$ and $\frac{d^3\sigma^W}{dY\,d\hat{s}\,dp_T}/\frac{d^2\sigma^Z}{dY\,dp_T}$ has a negligible theoretical uncertainty as the uncertainty associated with the choice of interaction scale and resummation formalism cancel in the ratio. There is a weak PDF dependence affecting the value of Γ_W by less than 1.5 MeV. An additional uncertainty from the value of α_s, used in the PDFs when calculating the cross-section ratios, is found to be less than 1 MeV by comparing the value of Γ_W obtained using the MRS-R1 and MRS-R2 [56] PDFs, whose main difference is the value of α_s.

The uncertainty on Γ_W from the boson p_T simulation is shown in table 5.8.

$m_{\mathrm{T}}^{\mathrm{fit}}$	g_1	g_2, B	g_3	PDFs, α_s	total
80	2	7	2	2	8
85	2	7	2	2	8
90	2	6	2	2	7
100	2	6	2	2	7
110	2	5	2	2	6

Table 5.8: *Systematic uncertainties, in MeV, from the $p_{\mathrm{T}}^{\mathrm{W}}$ simulation.*

Chapter 6

Detector simulation

The broadening of the W boson m_T distribution that results from the detector effects, has three main components. These are the resolution of the lepton p_T or E_T measurement, the resolution of the recoil measurement, and the rapidity distribution of accepted W bosons. This chapter describes the simulation of these detector effects on the m_T distribution, with the generated events described in chapter 5 as input. The associated uncertainty on the measurement of Γ_W is also evaluated.

The effect of the detector response and resolution on generated leptons are simulated using a fast parameterised detector simulation, tuned by fitting simulated Z boson events to candidate events, augmented with input from a full `GEANT-3` [57] simulation of the detector geometry and material. The detector lepton acceptance is simulated using a combination of simulated detector geometry and a parameterisation of acceptance efficiencies obtained from the data. The recoil response and resolution is simulated using a fast parameterised simulation, also tuned by fitting simulated Z boson events to candidate events.

6.1 z vertex simulation

The primary interaction point varies between events, and the distribution of the longitudinal component of the interaction point, the z vertex, can be derived from the beam luminosity function ($\mathcal{L}$) in the z direction. This is proportional to

$$\frac{d\mathcal{L}}{dz} \propto \frac{e^{\frac{-z^2}{2\sigma_z^2}}}{4\pi\sigma_x(z)\sigma_y(z)} \tag{6.1}$$

where σ_x and σ_y are the transverse beam widths. The beam widths are proportional to

$$\beta_{x,y}(z) = \beta_{x,y}^*[1 + (\frac{z - z_{0x,0y}}{\beta_{x,y}^*})^2] \tag{6.2}$$

and the z vertex distribution can be expressed as

$$\frac{e^{\frac{-z^2}{2\sigma_z^2}}}{\sqrt{[1 + (\frac{z-z_{0x}}{\beta^*})^2][1 + (\frac{z-z_{0y}}{\beta^*})^2]}} \tag{6.3}$$

assuming $\beta^* = \beta_x^* = \beta_y^*$.

By fitting to minimum bias events over the period data were collected for this analysis, the values $\sigma_z = 40 \pm 0.08$ cm, $z_{0x} = 3.00 \pm 1.87$ cm, $z_{0y} = 3.36 \pm 1.87$ cm and $\beta^* = 43.19 \pm 0.17$ cm are obtained. The z vertex distribution, shown in figure 6.1 (left), is simulated by randomly sampling the distribution in equation 6.3, and is shown in figure 6.1 (right) for W $\rightarrow$ eν candidate events.
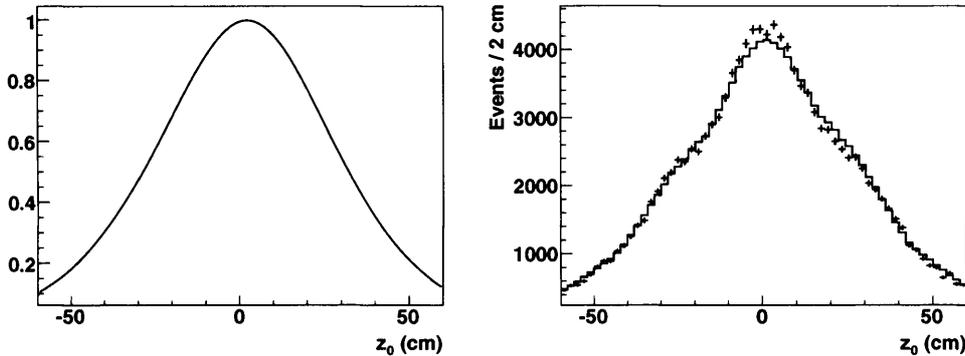
Figure 6.1: *The z vertex (left) functional form and (right) distribution for* W → eν *candidate and simulated events.*

6.2 Silicon tracker simulation

Leptons and final state QED photons from the hard collision traverse the silicon tracker before reaching the COT, interacting with the detector material. A description of the silicon tracker is provided by SiliMap, a lightweight parameterisation of the silicon tracker material based on the full GEANT-3 simulation of the CDF geometry and material (CdfSim), tuned to test-beam and collision data [58]. SiliMap is a 3 dimensional parameterisation of the geometry and properties of all the material up to the COT inner layer. SiliMap contains 32 radial layers, 999 layers in the z direction and a minimum of 120 layers in the φ direction, with the exact number depending on the level of detail required and the distance from the interaction point. The information necessary to simulate particle interactions with the material, described in section 2.1, is obtained for each cell using GEANT-3. Leptons, and final state QED photons from the event generator, are propagated through SiliMap where interactions with the detector material are simulated.

Bremsstrahlung radiation and pair-production produce secondary particles, which themselves propagate through the detector interacting with the detector material. Although the interaction of the secondary particles with the detector medium was also simulated, it was found that the effect on the measurement of Γ_W is negligible, and was therefore not included in the measurement of Γ_W.

Bremsstrahlung radiation is the dominant energy loss mechanism for electrons in the silicon tracker and is simulated using equation 2.3, with $y_{max} = 1.0$ and $y_{min} = 0.001$. The fractional radiation length is provided by SiliMap. The converted photons are distributed in y [20] using

$$\frac{d\sigma}{dy} = \frac{1}{y}\left(\frac{4}{3} - \frac{4y}{3} + y^2\right) \tag{6.4}$$

where y is the electron energy fraction converted into a photon.

Pair production is the dominant energy loss mechanism for photons in the silicon tracker and is simulated using equation 2.4 with the fractional radiation length provided by SiliMap. The converted photons are distributed in x [20] using

$$\frac{d\sigma}{dx} = 1 - \frac{4}{3}x(1 - x) \tag{6.5}$$

where x is the photon energy fraction converted into an electron or positron.

Ionisation is the dominant energy loss mechanism for muons, and is simulated for electrons and muons using equation 2.1 with Sternheimer's parameterisation of δ for silicon [20]. Values for K and I are provided by SiliMap.

6.2.1 Silicon tracker material scale

A multiplicative scale factor S^{mat} is applied to the fractional radiation lengths in SiliMap, and is found by fitting to the E/p distribution in W $\to$ eν candidate events in the region $0.8 < E/p < 2.0$. The E/p requirement for candidate electrons is removed so the E/p tail can be included in the fit, since it is sensitive to the amount of bremsstrahlung in the inner tracker. The resultant increase in QCD background, described in section 7.3, is reduced by increasing the $\not{E}_{\mathrm{T}}$ requirement to 30 GeV, giving a background of $(1.29 \pm 0.25)\%$ in this sample. The fitted E/p distribution with background events included in the simulation, shown in figure 6.2, gives

$$S^{\mathrm{mat}} = 1.033 \pm 0.007_{\mathrm{stat}} \pm 0.007_{\mathrm{background}} \tag{6.6}$$
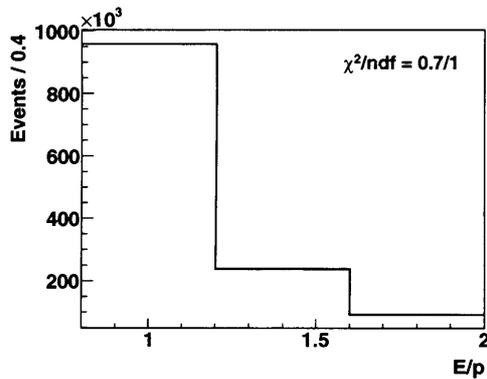
Figure 6.2: *The E/p distribution of* W $\to$ eν *candidate events fitted to obtain the* SiliMap *material scale factor, with background events added to the simulation.*

6.2.2 Silicon tracker simulation uncertainty

The uncertainty on Γ_W in $W \to e\nu$ events, from simulating only two iterations of particle interaction in the silicon tracker, is estimated as the maximum change in the value of Γ_W when simulating three and four iterations.

Bremsstrahlung radiation is suppressed below $y_{min} = E/E_M$ due to the Migdal effect [59], where E is the incident electron energy and $E_M = 72$ TeV for silicon. For electrons in the region of $25 < E_T < 100$ GeV, this corresponds to y_{min} in the region $0.0004 < y_{min} < 0.0014$. The uncertainty on Γ_W in $W \to e\nu$ events from simulating bremsstrahlung with $y_{min} = 0.001$ is estimated as the maximum change in the value of Γ_W using y_{min} values in the range $0.005 < y_{min} < 0.002$.

Compton scattering has a non-negligible cross-section for low energy photons, accounting for around 10% of the total cross-section for 100 MeV photons, rising to around 60% for 10 MeV photons. To estimate the systematic uncertainty from not including Compton scattering in the simulation, the latter is simulated in addition to pair production, according to the pair-production and Compton scattering cross-sections in silicon [60]. The Compton differential cross-section $(d\sigma/dy \propto 1/y + y)$ is obtained from the Klein-Nishina formula [61]. For $W \to e\nu$ events, the change in Γ_W from including Compton scattering is taken as the associated systematic uncertainty on Γ_W.

The uncertainties on Γ_W from the energy-loss simulation are shown in table 6.1 for $W \to e\nu$ events, and are negligible for $W \to \mu\nu$ events.

m_T^{fit}	iterations	bremsstrahlung	Compton	total
all	8	8	7	13

Table 6.1: *Systematic uncertainties for* $W \to e\nu$ *events, in MeV, from the energy-loss simulation.*

The systematic uncertainty on Γ_W from the material scale, shown in table 6.2, is obtained from the change in Γ_W from varying S^{mat} by the quoted uncertainty.

m_T^{fit}	
80	3
85	3
90	2
100	1
110	0

Table 6.2: *Systematic uncertainties for* W $\to$ eν *events, in MeV, from the silicon material scale.*

6.3   Central outer tracker simulation

The p_T of electrons and muons is determined from the track curvature in the COT. The measured p_T fluctuates about the true p_T from the quality of the reconstructed track and local variations in the magnetic field. Any difference in the overall magnetic field strength results in a p_T measurement that differs from the true p_T by a multiplicative scale factor, defined as the response.

6.3.1   Central outer tracker scale and resolution

The track curvature resolution is defined as

$$\Delta\rho = (\frac{q}{p_T})_{true} - (\frac{q}{p_T})_{measured} \tag{6.7}$$

where q is the lepton charge. The track curvature resolution is dependent on the length of the reconstructed track and subsequently on the number of hits. To account for this, the curvature resolution is found for the different hit combinations

using `CdfSim`. The COT response, and an additional global curvature resolution, are found using Z → $\mu\mu$ candidate events.

The $\Delta\rho$ distributions for the four possible N^{axial} and N^{stereo} combinations, which meet the requirements listed in section 4.2, are obtained from `CdfSim` W → $\mu\nu$ events, shown in figure 6.3 fitted with a Gaussian distribution.
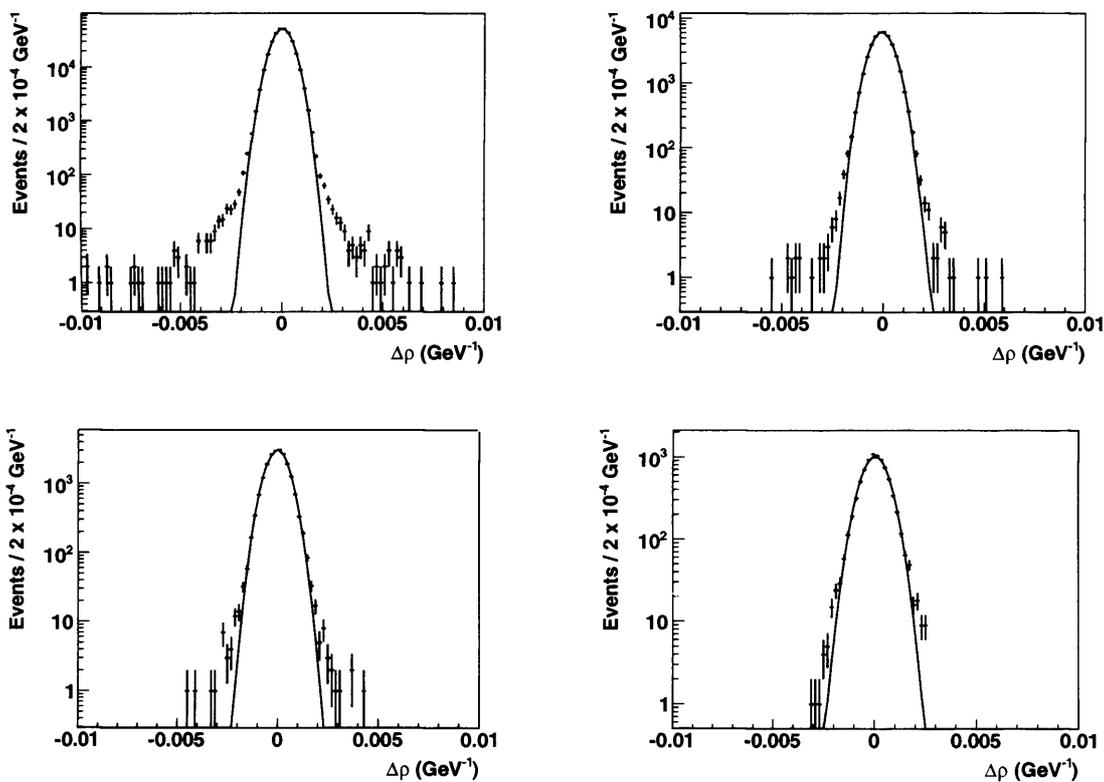
Figure 6.3: The $\Delta\rho$ distributions of `CdfSim` W → $\mu\nu$ events for muon tracks with (top) $N^{\text{axial}} = 4$, (bottom) $N^{\text{axial}} = 3$, (left) $N^{\text{stereo}} = 4$ and (right) $N^{\text{stereo}} = 3$.

The `CdfSim` $\Delta\rho$ distributions, with N^{axial} and N^{stereo} distributed according to Z → $\mu\mu$ candidate events, are sampled to simulate the p_T resolution. The sampled value of $\Delta\rho$ is multiplied by S^{res} to account for a global difference in the p_T resolution between the data and `CdfSim`. The resultant p_T value is multiplied

by S^{mom}, the COT response. The values of $S^{\mathrm{res}} = 1.100 \pm 0.039$ and $S^{\mathrm{mom}} =$ 0.9989 ± 0.0004 are obtained by minimising the χ^2 of fits to the $m_{\mu\mu}$ distribution of $Z \rightarrow \mu\mu$ candidate events, shown in figure 6.4. The linearity of the p_T response is confirmed to within 1 σ of the quoted uncertainty, since a combined measurement of the response using $J/\Psi \rightarrow \mu\mu$ and $\Upsilon \rightarrow \mu\mu$ events, which have an invariant mass of 3.1 GeV and 9.5 GeV respectively, gives $S^{\mathrm{res}} = 0.9985 \pm 0.0002$ [61].
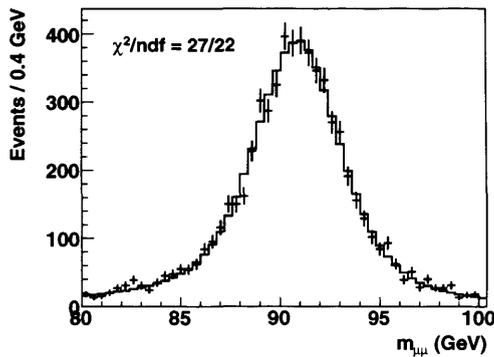
Figure 6.4: *The $m_{\mu\mu}$ distribution of* $Z \rightarrow \mu\mu$ *candidate events fitted to obtain the COT scale and global curvature resolution.*

The angular resolution of the track is simulated by smearing ϕ and $\cot(\theta)$ with Gaussian distributions of widths $\sigma_\phi = 0.002$ and $\sigma_{\cot(\theta)} = 0.011$ respectively, obtained by fitting to the $\phi_{\mathrm{true}} - \phi_{\mathrm{measured}}$ and $\cot(\theta_{\mathrm{true}}) - \cot(\theta_{\mathrm{measured}})$ distributions of `CdfSim` $W \rightarrow \mu\nu$ events.

6.3.2 Central outer tracker simulation uncertainty

The uncertainties on Γ_W for $W \rightarrow \mu\nu$ events from S^{res} and S^{mom} are estimated by varying the values individually by $-4\sigma, -2\sigma, +2\sigma$ and $+4\sigma$ from their nominal values. The 1σ uncertainty is obtained by interpolation.

The uncertainty associated with the `CdfSim` $\Delta\rho$ distribution is obtained by scaling the 'central' region of the $\Delta\rho$ distribution with respect to the 'tail' regions, both defined below, and fitting the E/p distribution of W $\to$ eν candidate events to obtain the scale factor. The central region of the $\Delta\rho$ distributions is defined as $|\Delta\rho| < 0.001$, and is fitted with a Gaussian. The tail region is defined as $|\Delta\rho| > 0.001$, and is scaled by $S^{\Delta\rho}$, which has a corresponding affect on overall resolution of $S^{\mathrm{res}} = 1.14 - 0.04 \times S^{\Delta\rho}$, so the latter is scaled accordingly. The value for $S^{\Delta\rho}$ is obtained by fitting to the E/p distribution of W $\to$ eν candidate events, shown in figure 6.5, with $E_{\mathrm{T}} > 35$ GeV and $E_{\mathrm{had}}/E_{\mathrm{em}} < 0.04$ to reduce the number of electrons with large hadronic leakage in the low E/p region. Large binning is chosen to decouple the track curvature resolution from the calorimeter resolution.
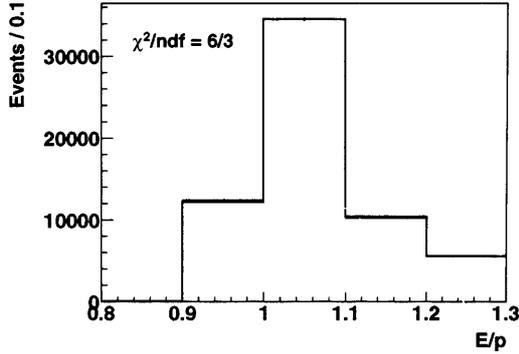
Figure 6.5: *The E/p distribution of* W $\to$ eν *candidate events fitted to obtain the scale factor applied to the region* $|\Delta\rho| > 0.001$ *of the* $\Delta\rho$ *distribution.*

The fitted value is

$$S^{\Delta\rho} = 1.03 \pm 0.28_{\mathrm{stat}} \pm 0.34_{\kappa} \pm 0.01_{S^{mat}} \pm 0.08_{\mathrm{background}} \qquad (6.8)$$

with the uncertainties evaluated for the fit (stat), calorimeter resolution (κ), silicon material scale (S^{mat}) and background.

The systematic uncertainties on Γ_W from the track curvature resolution distributions are obtained by varying $S^{\Delta\rho}$, which is consistent with unity, by its associated uncertainty and taking the change in the value of Γ_W. This, together with the uncertainty from the global resolution and response, is shown in table 6.3.

m_T^{fit}	S^{mom}	S^{res}	$S^{\Delta\rho}$
80	29	29	17
85	27	27	17
90	17	21	16
100	8	11	13
110	5	5	10

Table 6.3: *Systematic uncertainties for* W $\rightarrow$ $\mu\nu$ *events, in MeV, from the COT scale (S^{mom}), the global COT resolution (S^{res}) and COT track curvature resolution distributions ($S^{\Delta\rho}$).*

6.4   Calorimeter simulation

After exiting the COT, electrons and photons traverse the Time-of-Flight detector (ToF) and solenoid, interacting with the material before reaching the calorimeter towers. Also, constituents of the electromagnetic shower in the CEM may pass out of the back of the CEM and into the CHA. In addition to the 'extrinsic' calorimeter energy loss processes mentioned above, there is an 'intrinsic' energy loss from variations in light yield that depend on the depth of the electromagnetic shower. Both the extrinsic and intrinsic energy loss processes are simulated for individual electrons and photons, which are assigned to CEM towers providing they do not traverse the central gap at $|z| < 4.2$ cm or the gap between the wedges at $|x| > 23.1$ cm from the wedge centre.

The calorimeter resolution parameterises fluctuations in the measured tower energy about the true constituent electron and photon energy sum, and is simulated

together with the response, which parameterises the intrinsic energy loss. Lastly, the electron E_T and E_{had}/E_{em} measurement, and the muon E_{em} measurement are simulated.

6.4.1   ToF, solenoid and leakage energy loss simulation

The total electron and photon energy loss in the ToF and solenoid, and the energy leakage out the back of the CEM into the CHA, is parameterised using `CdfSim`. This takes into account any correlation between the energy loss in the ToF and solenoid, and energy leakage into the CHA. The detected energy fraction of incident electrons and photons as a function of their energy, shown in figure 6.6, is sampled in the simulation.

Any deficiencies associated with the parameterisation of the extrinsic calorimeter energy loss are absorbed into the non-linear calorimeter resolution parameterisation, described below, and the E_{had}/E_{em} electron selection efficiency parameterisation described in section 6.5.3.

6.4.2   Calorimeter response non-linearity

The intrinsic calorimeter energy loss has a dependence on E_T, resulting in a different response to incident electrons and photons of different energies. The reconstructed electron E_T is simulated by adding the E_T of the constituent electrons and photons ($E_T^{e,\gamma}$) after scaling by $a + b \times E_T^{e,\gamma}$ to account for the non-linear response. The tower E_T,

$$E_T = \sum (a + b \times E_T^{e,\gamma}) E_T^{e,\gamma} \tag{6.9}$$
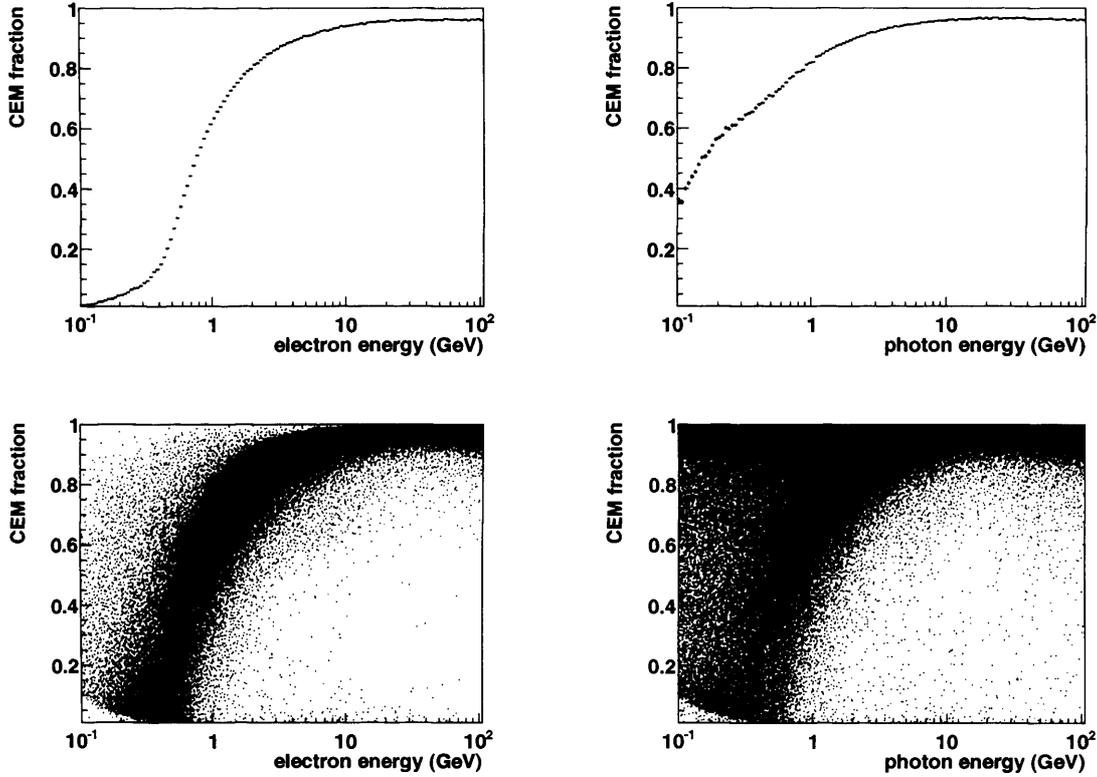
Figure 6.6: *The average energy fraction (top) deposited in the CEM as a function of incident energy and (bottom) the distribution of energy fractions, sampled in the simulation for each (left) electron and (right) photon exiting the COT.*

can be expressed as

$$E_{\mathrm{T}} = a \sum E_{\mathrm{T}}^{e,\gamma} + b \sum (E_{\mathrm{T}}^{e,\gamma})^2 \qquad (6.10)$$

showing the decoupling of the CEM response into a linear and a quadratic (non-linear) component. The latter is determined from fitting to the data and is included in the simulation. The linear response parameter (a) is measured after the inclusion of the non-linear part and is described in section 6.4.3.

Since the p_{T} response is linear, see section 6.3.1, the non-linear CEM response (b) is determined by fitting to the E/p distribution. The fit is performed in the

region $0.9 < E/p < 1.1$ to minimise the effect from the material scale. In W $\to$ eν events, the background is reduced to a negligible level by requiring $\not{E}_T > 30$ GeV. Simultaneous fits are made to W $\to$ eν candidate events in the region $25 < E_T < 50$ GeV in 2.5 GeV ranges, shown in figure 6.7, and to Z $\to$ ee candidate events in the range $30 < E_T < 55$ GeV. The fits have a χ^2/ndf of 180/193 and give the value of $b = (267 \pm 50) \times 10^{-6}$ GeV. By fitting to W $\to$ eν candidate events in 2.5 GeV ranges of E_T, the affect of the linear part of the response is largely decoupled from the non-linear part.

The uncertainty on Γ_W from the calorimeter response non-linearity, shown in table 6.4, is obtained by varying the non-linear part b by its uncertainty to give the subsequent change in the value of Γ_W.

m_T^{fit}	
80	12
85	13
90	12
100	10
110	6

Table 6.4: *Systematic uncertainties for* W $\to$ eν *events, in MeV, from the calorimeter response non-linearity.*

6.4.3 Calorimeter response and resolution

The measured CEM tower energy is simulated by smearing the true tower energy, after correcting for a non-linear response, and scaling by a linear response (S^{cem}). While the CEM resolution quoted in section 2.5.1 is sufficient for most analyses, this analysis requires a more sophisticated treatment. The constant term (κ) is from variations in response, and can be split into a correlated (κ^{corr}) and an uncorrelated (κ^{uncorr}) component to describe variations in response over time and
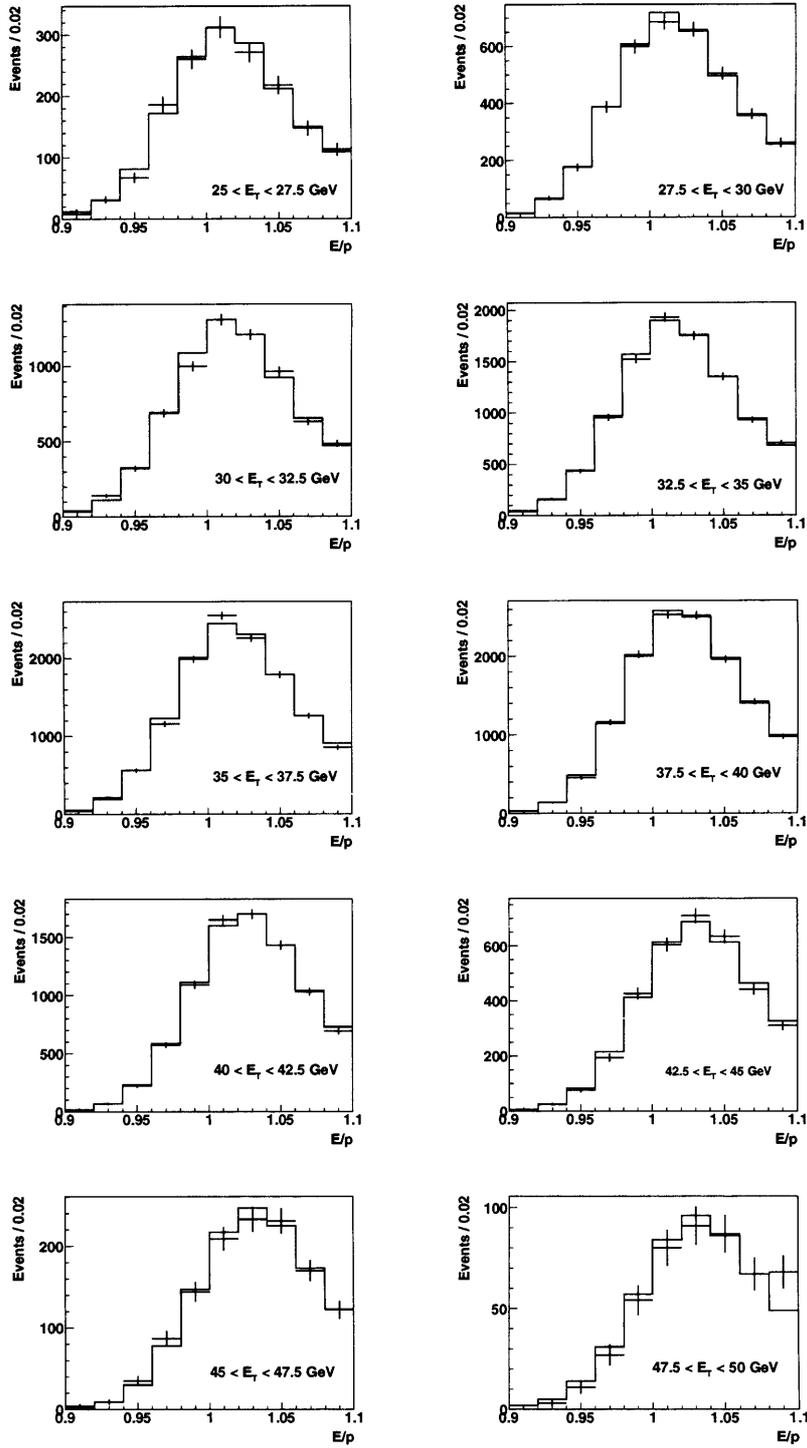
Figure 6.7: *The E/p distributions of* W → eν *candidate events in 2.5 GeV ranges of electron* E_T, *fitted to obtain the calorimeter response non-linearity.*

127

across towers respectively. The resolution is parameterised as

$$\frac{\sigma_E}{E} = \frac{13.5\%}{\sqrt{E_T}} \oplus \kappa^{\text{uncorr}} \oplus \kappa^{\text{corr}} \tag{6.11}$$

with κ^{corr} and κ^{uncorr} obtained from data.

Figure 6.8 shows the variation in the mean E/p ($<$E/p$>$) over time, which is from residual changes in the response after the offline electron reconstruction. The root-mean-square deviation from the mean value is taken as the correlated contribution to the resolution, as all electrons in an event are equally affected, giving $\kappa^{\text{corr}} = 0.29\%$. The correlated contribution to the resolution is simulated by randomly sampling a normalised Gaussian distribution for each event, with width $\sigma = \kappa^{\text{corr}}$, to obtain the multiplicative change in energy, and is applied to all electrons in the event.
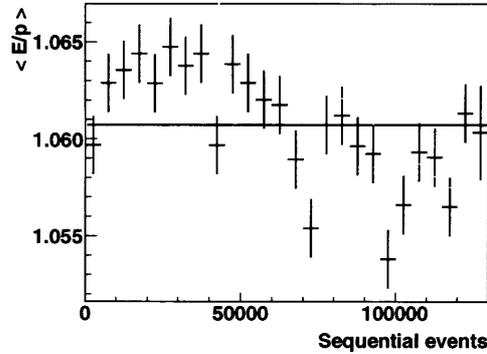
Figure 6.8: *The $<E/p>$ distribution as a function of time in* W $\rightarrow$ eν *candidate events used to obtain the correlated calorimeter resolution.*

The uncorrelated contribution to the resolution and the associated response correction, are determined by varying κ^{uncorr} and S^{cem} and independently minimising the χ^2 of a fit to the E/p distribution of W $\rightarrow$ eν candidate events, and the m_{ee} distribution of Z $\rightarrow$ ee candidate events.

The fit to the E/p distribution of W $\rightarrow$ eν candidate events, with the background events described in chapter 7 included, in the region $0.9 < E/p < 1.1$ gives

$$\kappa^{\mathrm{uncorr}} = (0.947 \pm 0.049_{\mathrm{stat}} \pm 0.147_{\mathrm{track}} \pm 0.056_{S^{\mathrm{mat}}})\% \qquad (6.12)$$

and

$$S^{\mathrm{cem}} = 1.02356 \pm 0.00021_{\mathrm{stat}} \pm 0.00044_{\mathrm{track}} \pm 0.00017_{S^{\mathrm{mat}}} \qquad (6.13)$$

where, in addition to the statistical uncertainty, the uncertainty has contributions from the track momentum scale and resolution, described in section 6.3.1, and the material scale S^{mat}, described in section 6.2.1. Choosing an alternate fit region of $0.96 < E/p < 1.1$ gives $\kappa^{\mathrm{uncorr}} = (0.64 \pm 0.11_{\mathrm{stat}})\%$.
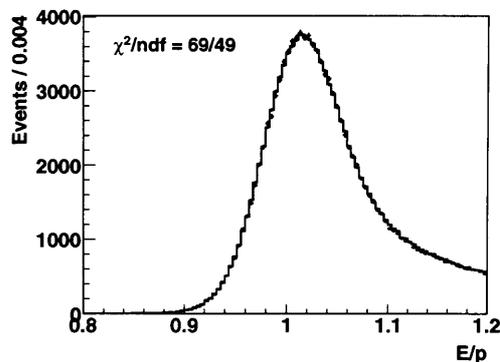
Figure 6.9: *The E/p distribution in* W $\rightarrow$ eν *candidate events fitted to obtain the uncorrelated calorimeter resolution.*

The fit to the m_{ee} distribution of Z $\rightarrow$ ee candidate events for $86 < m_{\mathrm{ee}} < 96$ GeV, shown in figure 6.10, gives $\kappa^{\mathrm{uncorr}} = (1.49 \pm 0.29)\%$ and $S^{\mathrm{cem}} = 1.02439 \pm 0.00078$.

The values for the response and resolution are combined in a weighted average using $a = \Sigma(a_i/\sigma_i^2)/\Sigma(1/\sigma_i^2)$ where a is the weighted average of individual measurements a_i with uncertainty σ_i. The combined uncertainty (σ) is given by
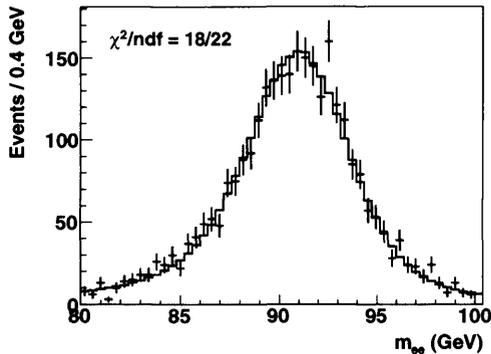
Figure 6.10: *The m_{ee} distribution of $Z \to$ ee candidate events fitted to obtain the calorimeter response and uncorrelated resolution.*

$1/\sigma^2 = \Sigma(1/\sigma_i^2)$. The values obtained for S^{cem} are consistent, and combine to give $S^{\mathrm{cem}} = 1.02382 \pm 0.00043$.

The three values for κ^{uncorr} are combined, but as the individual values differ by more than their uncertainty, the two extreme central values are used as the uncertainty bounds, giving $\kappa^{\mathrm{uncorr}} = 1.08^{+0.41}_{-0.44}\%$.

The uncorrelated and E_{T} dependent contribution to the resolution is simulated by randomly sampling a normalised Gaussian distribution with $\sigma = 13.5\%/\sqrt{E_{\mathrm{T}}} \oplus \kappa^{\mathrm{corr}}$ for each electron. The simulated electron energies are then scaled by S^{cem}.

6.4.4 Calorimeter response and resolution uncertainty

The uncertainties on Γ_{W} from the calorimeter resolution and response to electrons, shown in table 6.5, are obtained by individually varying the values by -4σ, -2σ, $+2\sigma$ and $+4\sigma$ from their nominal values. The 1σ uncertainty is obtained by interpolation. As κ^{uncorr} has an asymmetric uncertainty, the largest change in the value of Γ_{W} from the nominal value is taken as the uncertainty.

130

m_T^{fit}	S^{cem}	κ
80	29	46
85	27	43
90	17	31
100	7	11
110	4	4

Table 6.5: *Systematic uncertainties for* W $\to$ eν *events, in MeV, from the calorimeter response (S^{cem}) and resolution (κ).*

6.4.5 Electron E_T simulation

Individual electrons and photons are assigned to towers, and their energy is summed using equation 6.9, and smeared to simulate the CEM resolution. The electron clustering algorithm, described in section 2.8.2, is then performed on the simulated tower E_T deposits to determine the two towers used in the electron E_T simulation.

The E_T of electron candidates have a 'pedestal' from the contribution from the underlying event energy, described in section 4.3. Since the latter has a dependence on luminosity, shown in figure 4.2 (right), the electron pedestal also has this dependence. The luminosity dependence is parameterised as the calorimeter ΣE_T, described in section 6.6.1, and the average two-tower underlying event energy as a function of ΣE_T is sampled in W $\to$ eν candidate events, from a region at the same η and orthogonal in ϕ to the electron.

The simulated reconstructed electron E_T is the two-tower cluster and underlying event energy sum, and has the direction of the highest p_T electron track. Although this track is also used to determine the electron $\vec{p_T}$, it is not necessarily the generated electron track as a sufficiently energetic photon from bremsstrahlung in the silicon tracker may convert into an e$^+$e$^-$ pair.

6.4.6 Electron $E_{\text{had}}/E_{\text{em}}$ requirement simulation

The electron $E_{\text{had}}/E_{\text{em}}$ distribution, which is used to select electron candidates, is simulated using the two-tower cluster energy and the simulated hadronic energy. The latter is obtained by simulating the CHA response and resolution of the energy leakage out of the CEM into the CHA obtained from CdfSim. The CHA response is taken as 0.8, the mean E/p for the CEM and CHA energy sum for events containing a single high p_{T} track [37]. The CHA resolution is simulated as Gaussian distributed with a width of $\sigma = 20\%/\sqrt{\text{E}}$, with the stochastic term obtained from the best fit to the $E_{\text{had}}/E_{\text{em}}$ distribution of Z $\rightarrow$ ee candidate events, shown in figure 6.11. This parameterisation is augmented and the associated uncertainties are evaluated in section 6.5.3.
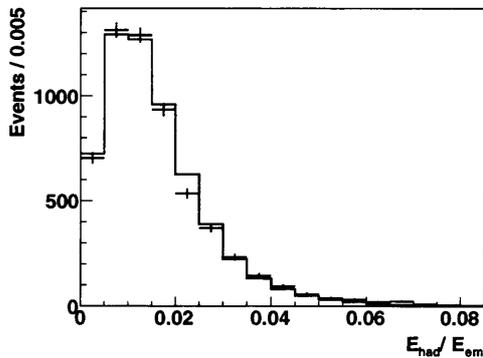
Figure 6.11: *The $E_{\text{had}}/E_{\text{em}}$ distribution of Z $\rightarrow$ ee events, fitted to obtain the CHA resolution for energy leakage out of the CEM.*

6.4.7 Muon E_{em} requirement simulation

The energy deposited by a muon in the CEM (E_{em}) is used to select muon candidates. This is simulated by adding the energy deposited in the CEM, taken

from a parameterisation of cosmic ray data, to the simulated underlying-event energy plus any energy from electrons, positrons and photons ending up in the same tower as the muon.

6.5   Lepton selection simulation

The geometric selection of leptons from the fiducial detector regions affects the lepton kinematic distributions, and subsequently the m_T distribution of W boson events. Additionally, the efficiency of lepton selection varies between different detector regions and as a function of the lepton kinematics. These efficiencies are included in the simulation and the associated uncertainty is estimated.

Selection efficiencies are obtained from a sample of N_{total} leptons and the subset of N_{pass} leptons that meet the lepton requirements, using $\epsilon = N_{pass}/N_{total}$ with the estimated binomial uncertainty given by $\sigma_\epsilon = \sqrt{\epsilon(1 - \epsilon)/N_{total}}$.

6.5.1   Lepton η and ϕ dependent selection simulation

Electron online selection simulation

At least one electron candidate in W $\rightarrow$ eν and Z $\rightarrow$ ee candidate events has passed the ELECTRON_CENTRAL_18 trigger path, described in section 2.8.3. The efficiency of the ELECTRON_CENTRAL_18 XFT requirement, described in section 2.8.1, varies with η and affects the lepton η distribution and subsequently the Γ_W measurement. The XFT efficiency as a function of η is found in W $\rightarrow$ eν candidate events that have additionally passed the W_NOTRACK trigger path, described in

section 2.8.3. This trigger has the same electron calorimetry requirements as the

ELECTRON_CENTRAL_18 trigger path and no track requirements.

The efficiency of the XFT requirement as a function of η is parameterised as

$$\epsilon(\eta) = a_0 + a_1 e^{-\eta^2/2\sigma_1^2} + a_2 e^{-\eta^2/2\sigma_2^2} \qquad (6.14)$$

with parameter values, shown in table 6.6, obtained by minimising the χ^2 of the fitted distribution shown in figure 6.12. The online selection is simulated by

a_0	0.988
a_1	-0.100
a_2	0.080
σ_1	0.266
σ_2	0.102

Table 6.6: *Parameter values for the XFT trigger efficiency as a function of η.*

weighting generated events in η according to the parameterised XFT efficiency.
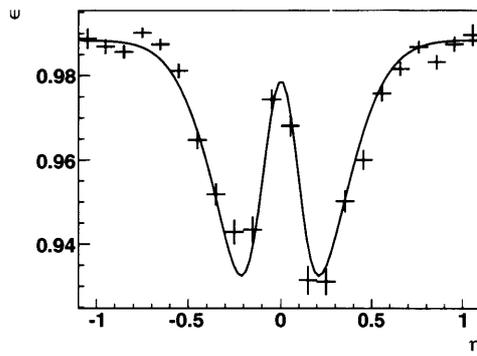
Figure 6.12: *The fitted XFT efficiency as a function of η_{trk}.*

134

Muon online selection simulation

Muon candidates have passed at least one of the MUON_CMX18 and MUON_CMUP18 trigger paths described in section 2.8.4. The efficiency of each trigger path can be measured in Z → $\mu\mu$ candidate events by selecting events containing two tight muons, where one is fiducial in the CMX chamber and the other in the CMUP. The trigger efficiencies are obtained from the sample that has further passed the other trigger path to the one being measured and the subset that have passed both. The obtained efficiencies are ϵ(MUON_CMX18) = 0.971 and ϵ(MUON_CMUP18) = 0.894 which are applied as an additional weight to generated events.

Muon chamber simulation

Muon trajectories are extrapolated to the simulated muon chamber geometry and rejected if they do not meet the fiducial requirement, described in section 4.2. The efficiency of a muon leaving a detectable track, or stub, in the muon drift chamber that matches a COT track, as defined in Table 4.3, is measured in Z → $\mu\mu$ candidate events for the CMX and CMUP subdetectors. For events that have two fiducial muons in the subdetector being measured, each muon with a stub is selected as a trigger leg. The muon stub reconstruction efficiencies are obtained from the sample comprising the other muon in the event, the test leg, and the subset which meet the stub requirement. The obtained efficiencies are ϵ(CMX) = 0.988 and ϵ(CMUP) = 0.870 which are applied as an additional weight to generated events.

Electron track requirement simulation

The efficiency of the electron track requirements as a function of track η is obtained from the sample of events passing the W_NOTRACK trigger path and the electron calorimeter requirements, and the subset that additionally pass the electron track requirements, both described in section 4.1. The efficiency distribution is fitted with equation 6.14, show in figure 6.13 (left), to obtain the parameter values shown in table 6.7. The parameterised efficiency is applied as an additional weight to generated events.

a_0	0.957
a_1	-3.000
a_2	2.991
σ_1	0.393
σ_2	0.395

Table 6.7: *Parameter values for the electron track selection efficiency as a function of track η.*

Muon track requirement simulation

The muon track selection efficiency is obtained from $Z \rightarrow \mu\mu$ candidate events since, unlike $W \rightarrow \mu\nu$ events, relaxing the track hit requirements does not result in a significant increase in background. The efficiency is obtained using all the tight muons, described in section 4.2, as 'reference legs' and dividing the other 'test legs' into a sample that meet all but the track requirements, and the subset that additionally meet the track requirements. The efficiency is parameterised as a third order polynomial with parameter values, shown in table 6.8, obtained by minimising the χ^2 of the fitted efficiency distribution shown in figure 6.13. The parameterised efficiency is applied as an additional weight to generated events.
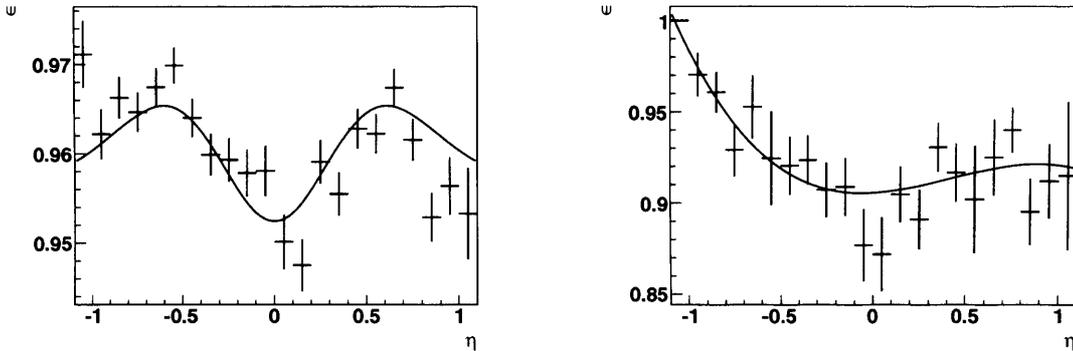
Figure 6.13: *The fitted (left) electron and (right) muon track hit efficiency as a function of track η.*

p_0	0.907
p_1	0.013
p_2	0.047
p_3	-0.047

Table 6.8: *Parameter values for muon track hit efficiency as a function of η.*

Lepton η and ϕ distributions

The lepton η and ϕ distributions are shown in figure 6.14 for $W \rightarrow e\nu$ and $W \rightarrow \mu\nu$ candidate events, with error bars representing the statistical uncertainty only.

The uncertainty on Γ_W associated with the η and ϕ lepton acceptance simulation, shown in table 6.9, is obtained from the change in Γ_W when the simulated events are weighted so that the η and ϕ distributions are identical to the data.
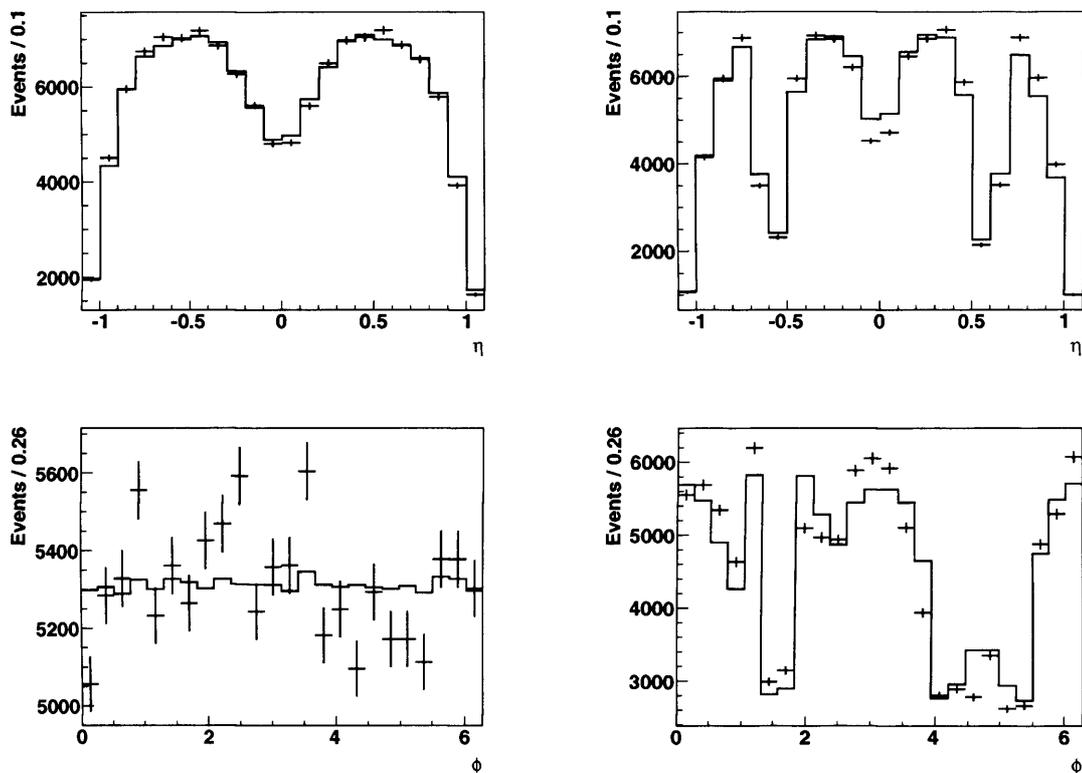
Figure 6.14: *The (top) η and (bottom) ϕ distributions for (left) W $\to$ eν and (right) W $\to$ $\mu\nu$ candidate events.*

m_T^{fit}	W $\to$ eν			W $\to$ $\mu\nu$		
	η	ϕ	total	η	ϕ	total
80	2	1	3	2	3	4
85	2	1	3	2	3	4
90	2	1	3	2	3	4
100	2	1	3	3	3	5
110	2	1	3	3	3	5

Table 6.9: *Systematic uncertainties, in MeV, from the lepton η and ϕ acceptance simulation.*

6.5.2 Lepton $u_{||}$ dependent selection simulation

The efficiency of the lepton selection decreases as proximate event activity increases. It is highest when the recoil component parallel to the lepton ($u_{||}$) is

138

zero, and lowest when the recoil is in the same direction of the lepton ($u_{||} = |u|$). The efficiency is parameterised as a linear function of $u_{||}$ as

$$
\epsilon(u_{||}) = \begin{cases} 1 + A \times u_{||} & \text{for } u_{||} < 0 \\ 1 + B \times u_{||} & \text{for } u_{||} > 0 \end{cases} \tag{6.15}
$$

with $\epsilon(u_{||} = 0) = 1$.

The parameters A and B, shown in table 6.10, are obtained from W boson events in CdfSim, shown in figure 6.15, and also from Z boson events in both CdfSim and data.
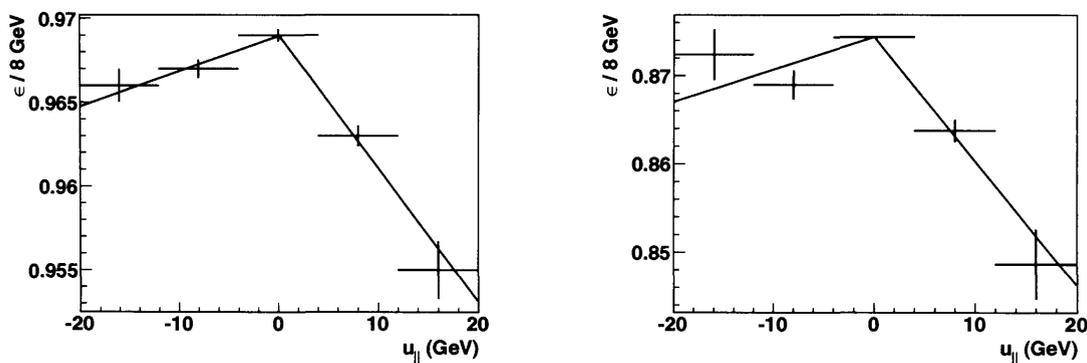
Figure 6.15: *Lepton selection efficiency as a function of $u_{||}$ for* CdfSim *(left)* W $\rightarrow$ eν *and (right)* W $\rightarrow$ $\mu\nu$ *events.*

The values obtained from CdfSim W boson events are applied as an additional weight to generated events. The values obtained from Z boson events are used to confirm that CdfSim is consistent with the data. The statistical limitation of this check, estimated as the interval between the W boson value and the furthest bound of the combined Z boson values, is taken as the systematic uncertainty on the W boson parameter values.

		A ($\times 10^{-4}$)	B ($\times 10^{-4}$)
Z → ee	data	7.1 ± 7.8	-5.6 ± 8.6
Z → ee	CdfSim	5.5 ± 1.6	-8.6 ± 1.8
W → eν	CdfSim	$3.4 \pm 1.0_{\text{stat}} \pm 3.7_{\text{sys}}$	$-8.7 \pm 4.6_{\text{stat}} \pm 13.4_{\text{sys}}$
Z → $\mu\mu$	data	2.6 ± 8.0	-26.0 ± 9.3
Z → $\mu\mu$	CdfSim	1.3 ± 1.4	-17.2 ± 1.8
W → $\mu\nu$	CdfSim	$4.8 \pm 2.9_{\text{stat}} \pm 14.8_{\text{sys}}$	$-16.0 \pm 5.8_{\text{stat}} \pm 5.7_{\text{sys}}$

Table 6.10: *Parameter values for lepton selection efficiency as a function of $u_{\parallel}$.*

The uncertainty on Γ_{W}, shown in table 6.11, is obtained from the change in Γ_{W} when varying parameters A and B by their combined uncertainty.

$m_{\text{T}}^{\text{fit}}$	W → eν	W → $\mu\nu$
80	2	7
85	2	7
90	2	6
100	1	2
110	0	1

Table 6.11: *Systematic uncertainties, in MeV, from $\epsilon(u_{\parallel})$ simulation.*

6.5.3 Electron E_{T} dependent selection simulation

The E_{T} dependence of the electron selection, excluding the $E_{\text{had}}/E_{\text{em}}$ requirement, is taken from CdfSim W → eν events, shown in figure 6.16 (left). It is parameterised as

$$\epsilon(E_{\text{T}}) = \begin{cases} C + D \times (E_{\text{T}} - 42) & \text{for } E_{\text{T}} < 42\,\text{GeV} \\ C & \text{for } E_{\text{T}} > 42\,\text{GeV} \end{cases} \quad (6.16)$$

with parameter values shown in table 6.12 together with parameter values obtained from Z → ee events in both CdfSim and data.

Equation 6.16, with the value for D obtained from CdfSim W boson events and
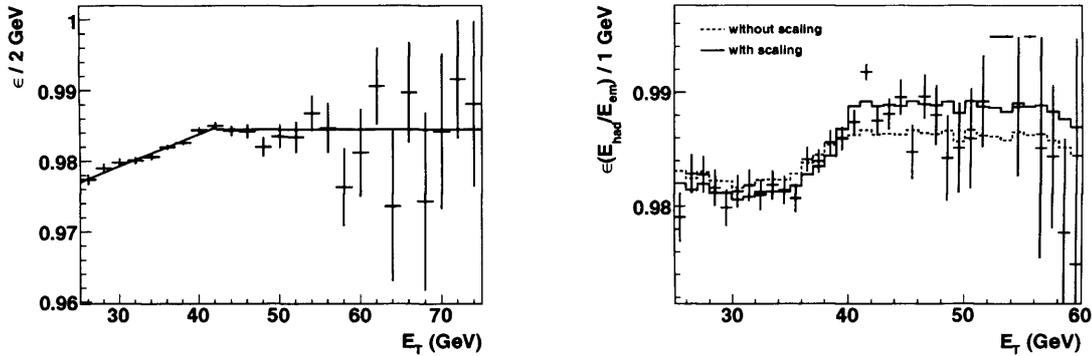
Figure 6.16: *Electron selection efficiency as a function of E_T excluding the E_{had}/E_{em} requirement (left) and for only the E_{had}/E_{em} requirement (right), with the simulated E_{had}/E_{em} efficiencies normalised so the average efficiency is equal for all three distributions.*

		D $\times 10^{-4}$ GeV^{-1}	C
$Z \to ee$	data	7.1 ± 5.6	0.98
$Z \to ee$	CdfSim	7.2 ± 0.1	0.9789
$W \to e\nu$	CdfSim	$4.6 \pm 0.4_{stat} \pm 3.6_{sys}$	0.9845

Table 6.12: *Parameter values for $\epsilon(E_T)$ simulation.*

C set to untiy, is applied as an additional weight to generated events. The values for D obtained from Z boson events are used to confirm that CdfSim is consistent with the data. The statistical limitation of this check, estimated using the same method as in section 6.5.2, is taken as the systematic uncertainty on the W boson parameter values.

The uncertainties on Γ_W associated with the E_T dependent selection efficiency, excluding the E_{had}/E_{em} requirement, are shown in table 6.13. They are obtained from the change in Γ_W from varying parameter D by its combined uncertainty.

The E_{had}/E_{em} requirement is excluded from the parameterisation of the electron selection efficiency as it is included in the calorimeter simulation, described in

section 6.4.6. However, an additional E_T dependent scale factor ($S^{\text{had/em}}$) is applied to simulated $W \rightarrow e\nu$ events to match the simulated $E_{\text{had}}/E_{\text{em}}$ distribution to that of candidate events, after applying a normalisation factor that preserves the average efficiency. The $E_{\text{had}}/E_{\text{em}}$ distribution of $W \rightarrow e\nu$ candidate events is shown in figure 6.16 (right), together with the $E_{\text{had}}/E_{\text{em}}$ distribution simulated both with and without applying the $S^{\text{had/em}}$ scale factor, and normalised so the average efficiency is equal in all three distributions. The values of $S^{\text{had/em}}$ obtained are

$$
S^{\text{had/em}} = \begin{cases} 0.9964 & \text{for } E_T < 39\,\text{GeV} \\ 1.0 & \text{for } E_T > 40\,\text{GeV} \\ 0.9964 + 0.0036 \times (E_T - 39) & \text{otherwise} \end{cases} \tag{6.17}
$$

and are applied as an additional weight to generated events.

The uncertainties on Γ_W associated with scaling $E_{\text{had}}/E_{\text{em}}$ by the E_T dependent factor $S^{\text{had/em}}$, shown in table 6.13, is estimated as the change in Γ_W simulated with and without including the $S^{\text{had/em}}$ scale factor. The $E_{\text{had}}/E_{\text{em}}$ distribution in the region $E_T \gtrsim 50$ GeV is not constrained by $W \rightarrow e\nu$ candidate events, and no scaling is applied. The associated uncertainty on Γ_W is estimated as the shift in Γ_W obtained when applying a linear scale factor in the '$E_{\text{had}}/E_{\text{em}}$ tail' region of $50 < E_T < 100$ GeV, determined by matching the simulated $E_{\text{had}}/E_{\text{em}}$ distribution to that of CdfSim.

$m_{\mathrm{T}}^{\mathrm{fit}}$	$\epsilon(E_{\mathrm{T}})$	$S^{\mathrm{had/em}}$	$E_{\mathrm{had}}/E_{\mathrm{em}}$ tail	total
80	6	12	1	13
85	6	12	1	13
90	4	9	1	10
100	3	7	2	8
110	3	7	3	8

Table 6.13: *Systematic uncertainties for* W $\to$ eν *events, in MeV, from* $\epsilon(E_{\mathrm{T}})$ *simulation.*

6.5.4 Muon p_{T} dependent selection simulation

The muon selection, described in section 4.2, has a p_{T} dependent E_{had} threshold resulting in a p_{T} independent selection efficiency, shown in figure 6.17 (left). The p_{T} dependent E_{had} threshold is obtained from the muon $\langle E_{\mathrm{had}} \rangle$ distribution as a function of p_{T} in CdfSim W $\to$ $\mu\nu$ events, which has a linear fit, shown in figure 6.17 (right), of $E_{\mathrm{had}} = 5.6 + 0.014 \times p_{\mathrm{T}}$ GeV.

The systematic uncertainty on Γ_{W} is taken as the change in Γ_{W} from varying the slope of the E_{had} requirement by its statistical uncertainty, giving an uncertainty of 1 MeV.
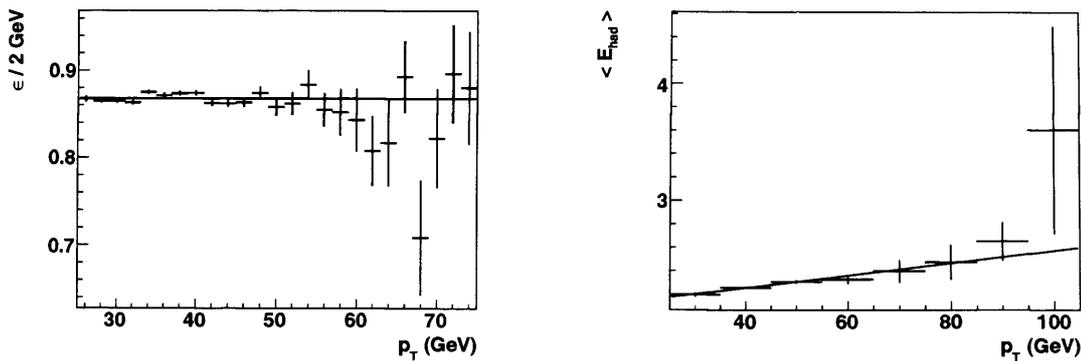
Figure 6.17: *Muon selection efficiency as a function of* p_{T} *(left) for* W $\to$ $\mu\nu$ *candidate events and (right) muon* $\langle E_{\mathrm{had}} \rangle$ *as a function of* p_{T} *for CdfSim events.*

6.6 Recoil simulation

The recoil, described in section 4.3, has a 'hard' component from QCD radiation from the boson production, and a 'soft' component from the spectator parton interactions and minimum bias events. The hard recoil component is primarily the detector response to the radiation balancing the boson p_T. Hence the hard recoil component shows a strong correlation with boson $\vec{p_T}$, increasing with the p_T and predominantly directed anti-parallel to it. The soft recoil component is strongly correlated with luminosity since it is dependent on the rate of $p\bar{p}$ interactions.

In order to decouple the hard and soft recoil contributions, the recoil ($\vec{u}$) is parameterised in terms of a parallel component (u_1) and a perpendicular component (u_2) with respect to the boson $\vec{p_T}$. As the latter is not well measured for W boson candidates, the parameters of the recoil model are determined from Z boson candidate events, since p_T^Z is well measured. The recoil simulation is parameterised in terms of the true boson p_T, described in section 5.2.

6.6.1 ΣE_T simulation

Both the recoil and the simulated electron E_T, described in section 6.4.5, have a dependence on luminosity that is included in the simulation. As the luminosity and the calorimeter ΣE_T, defined in section 4.3, are highly correlated, shown in figure 6.18, the latter is simulated as it is an explicit measure of calorimeter activity.

To include correlations between the boson p_T and the ΣE_T distribution, the latter
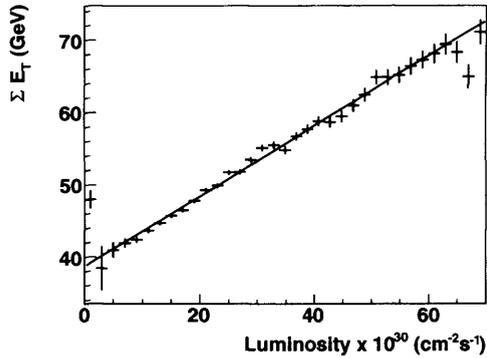
Figure 6.18: ΣE_T *as a function of luminosity for* W $\rightarrow$ eν *candidate events.*

is parameterised as

$$\Sigma E_T = (Q_1 + Q_2 \times p_T) \times \Gamma(Q_3 + Q_4 \times p_T) \qquad (6.18)$$

where Γ is the gamma function and p_T is the simulated true boson p_T. The parameters are obtained by minimising the χ^2 sum of simultaneous fits to the ΣE_T distribution and the mean ΣE_T ($\langle \Sigma E_T \rangle$) as a function of p_T^Z, shown in figure 6.19. The value of the parameters is determined separately for Z $\rightarrow$ ee and Z $\rightarrow$ $\mu\mu$ candidate events, and shown in table 6.14.

	Z $\rightarrow$ ee	Z $\rightarrow$ $\mu\mu$
Q_1	20.700	19.351
Q_2	-0.154	-0.141
Q_3	2.055	2.051
Q_4	0.085	0.100

Table 6.14: *Parameter values for the* ΣE_T *parameterisation.*
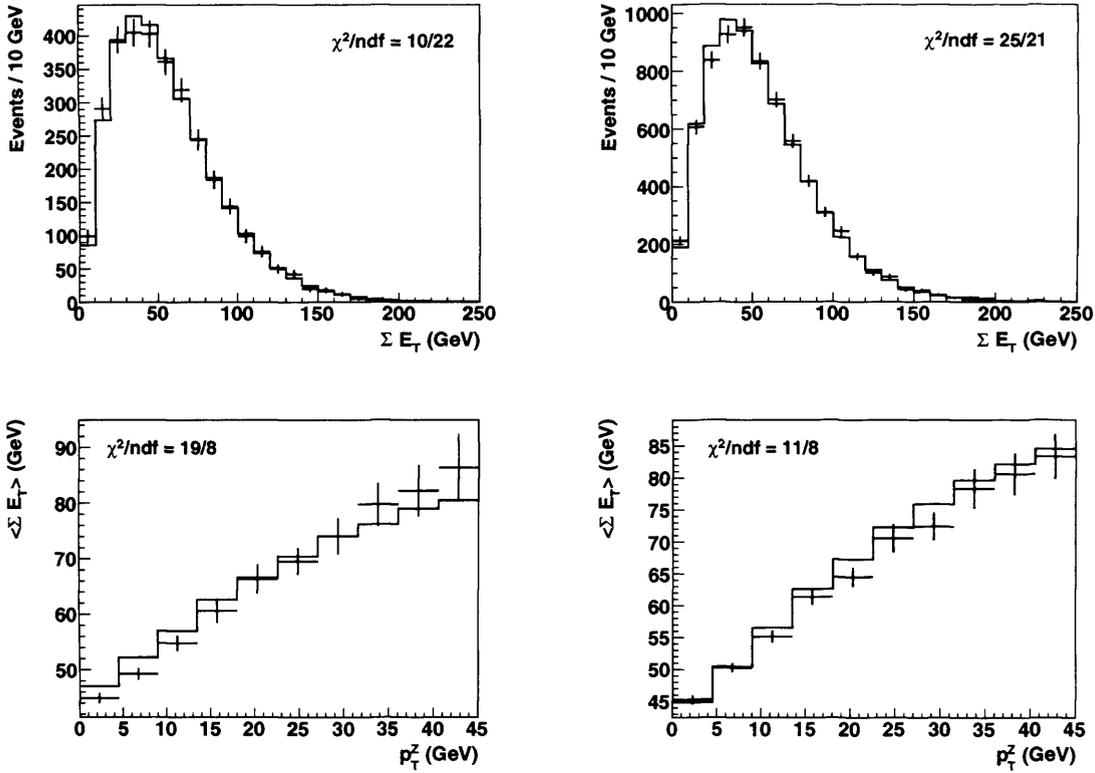
Figure 6.19: *The (top)* ΣE_T *distribution and (bottom)* $\langle \Sigma E_T \rangle$ *as a function of* p_T^Z, *fitted to obtain the* ΣE_T *parameters for (left)* Z $\rightarrow$ ee *and (right)* Z $\rightarrow$ $\mu\mu$ *candidate events.*

6.6.2 Soft recoil resolution simulation

The direction of the soft recoil components is defined along the x and y axis (u_x and u_y respectively). The components are parameterised as Gaussian distributed quantities with $\langle u_{x,y} \rangle = 0$ and with a resolution (σ) parameterised as

$$\sigma(u_{x,y}) = R_1 \times (\Sigma E_T)^{R_2} \tag{6.19}$$

with parameters R_1 and R_2 obtained from minimum bias events with a tower threshold of 100 MeV. By simultaneously minimising the χ^2 of the fits to $\sigma(u_{x,y})$

as a function of ΣE_T, shown in figure 6.20, a combined soft recoil resolution (σ_{MB}) with parameters $R_1 = 0.3384$ and $R_2 = 0.5589$ is obtained.
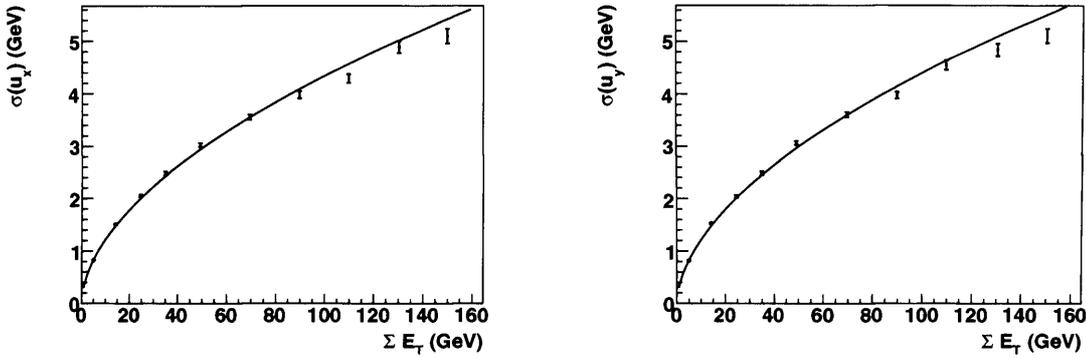
Figure 6.20: *The soft recoil resolution along the (left) x axis and the (right) y axis as a function of ΣE_T in minimum bias events, fitted to obtain the soft recoil parameter values.*

6.6.3 Recoil resolution and response simulation

The recoil components u_1 and u_2 are parameterised as Gaussian distributed quantities. Since u_2 is primarily sensitive to the soft recoil contribution, which has a uniform azimuthal distribution, the mean response of u_2 ($\langle u_2 \rangle$) is zero in the parameterisation. Conversely, u_1 is primarily sensitive to the hard recoil contribution which is strongly correlated with boson p_T, and the mean response of u_1 ($\langle u_1 \rangle$) is parameterised in terms of the true boson p_T as

$$\langle u_1 \rangle = (P_1 + P_2 \times p_T) \times (1 - e^{-p_3 \times p_T}) \tag{6.20}$$

with the parameters $P_{1,2,3}$ determined from fits to Z boson candidate events.

The resolutions (σ) of u_1 and u_2 are defined as the widths of their Gaussian

distributions, and are parameterised in terms of the true boson p_T and σ_{MB}, as

$$\sigma(u_1) = \sigma_{MB} \times (P_4 + P_5 \times p_T) \qquad (6.21)$$

and

$$\sigma(u_2) = \sigma_{MB} \times (P_6 + P_7 \times p_T) \qquad (6.22)$$

with the parameters $P_{4,5,6,7}$ also determined from fits to Z boson candidate events.

The recoil parameters, shown in table 6.15, are obtained separately for Z $\rightarrow$ ee and Z $\rightarrow$ $\mu\mu$ candidate events by minimising the total χ^2 of simultaneous fits to $\langle u_1 \rangle$, $\sigma(u_1)$ and $\sigma(u_2)$ distributions as a function of p_T^Z shown in figure 6.21. The uncertainties quoted are taken from the diagonal elements of the 7×7 covariance matrix. The total χ^2 of the fits is 26/24 for Z $\rightarrow$ ee candidate events and 29/24 for Z $\rightarrow$ $\mu\mu$ candidate events.

	W $\rightarrow$ eν		W $\rightarrow$ $\mu\nu$	
P_1	-12.7	$\pm$ 1.1	-13.1	$\pm$ 1.5
P_2	-0.589	$\pm$ 0.02	-0.586	$\pm$ 0.02
P_3	0.043	$\pm$ 0.003	0.042	$\pm$ 0.004
P_4	0.93	$\pm$ 0.03	0.97	$\pm$ 0.02
P_5	0.019	$\pm$ 0.003	0.016	$\pm$ 0.002
P_6	1.025	$\pm$ 0.03	1.064	$\pm$ 0.02
P_7	0.0002	$\pm$ 0.002	-0.002	$\pm$ 0.001

Table 6.15: *Parameter values for the recoil response and resolution, with their statistical uncertainties obtained from the fits to the Z data.*

Figure 6.22 shows the comparison between simulation and data of the distributions of u, u_1 ,u_2 and the angle $(\Delta\phi)$ between the boson p_T direction and the recoil for Z boson candidate events.

148

6.6.4 Recoil simulation for W boson events

Since the production processes for W and Z bosons are very similar, the recoil model and parameters, obtained for Z boson events, are used to simulate the recoil for W boson events. The lepton and neutrino travel in opposite directions in the boson rest frame, so the boson m_{T} is given by $m_{\mathrm{T}} \approx 2E_{\mathrm{T}} + u_{||}$ and
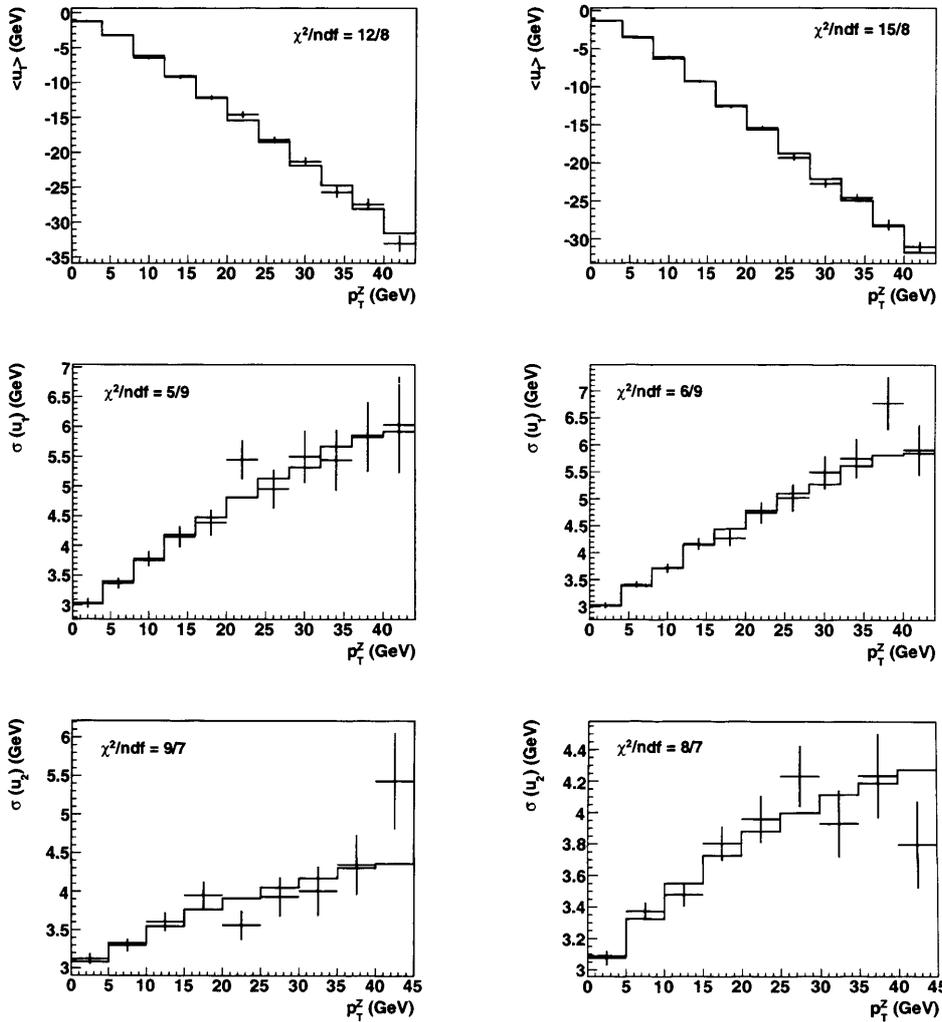
Figure 6.21: *The $\langle u_1 \rangle$, $\sigma(u_1)$ and $\sigma(u_2)$ distributions (rows 1-3 respectively) as a function of p_{T}^Z for (left) $Z \to ee$ and (right) $Z \to \mu\mu$ candidate events, fitted to obtain the recoil parameter values.*
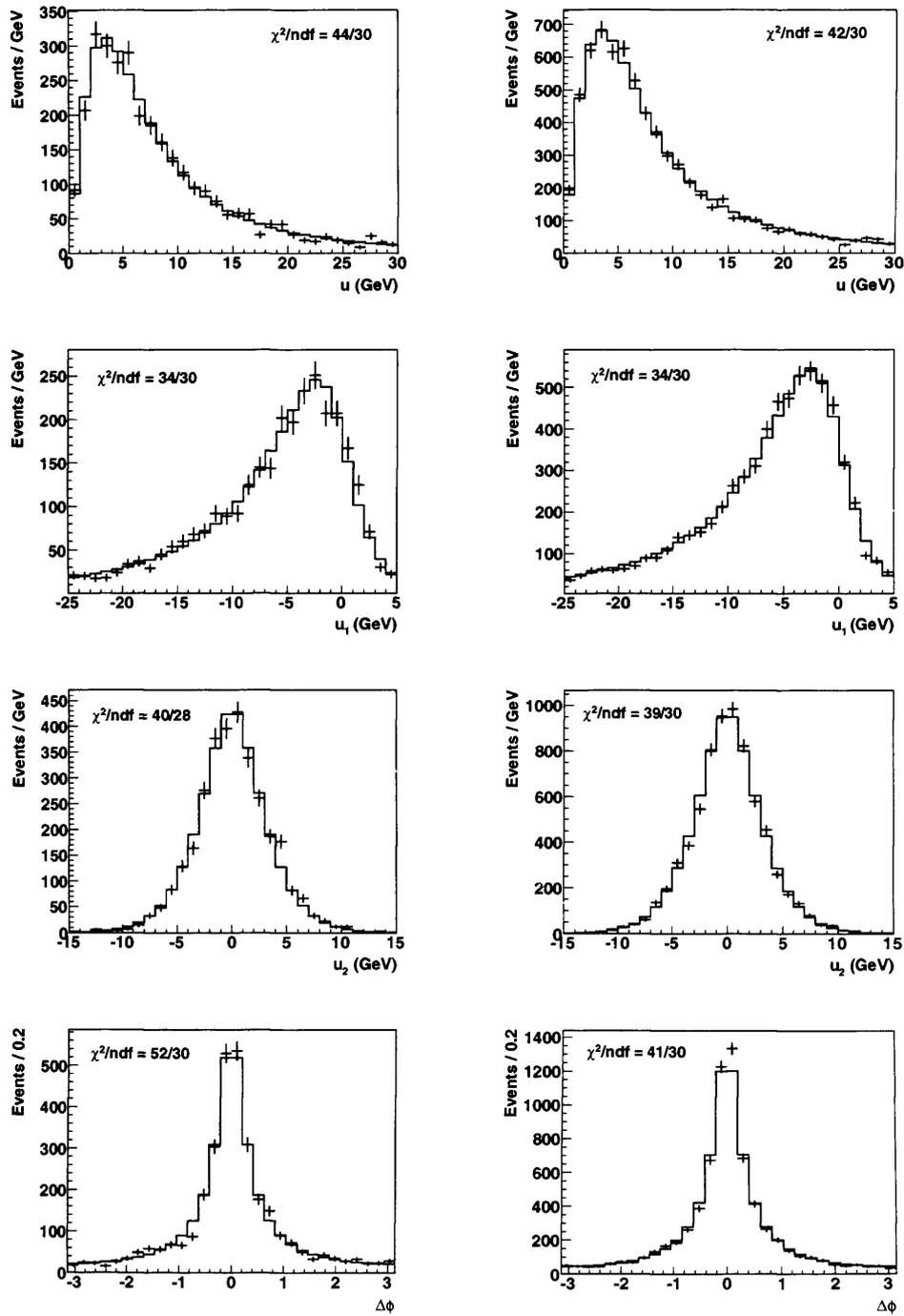
Figure 6.22: *The distributions of u, u_1, u_2 and the angle $\Delta\phi$ between u and p_T^Z (rows 1-4 respectively) for (left) $Z \to ee$ and (right) $Z \to \mu\mu$ candidate events.*

is directly affected by $u_{||}$. Consequently, it is essential that the simulated $u_{||}$ distributions provide a good description of the data. The mean values of $u_{||}$, shown in table 6.16, are consistent between data and simulation.

The $\not{E}_T$, u, $u_{||}$ and $u_\perp$ distributions are shown in figure 6.23 for $W \to e\nu$ and $W \to \mu\nu$ events with the background contributions, described in chapter 7, added to the simulation. Additionally, the distribution of $\langle u_{||} \rangle$ as a function of m_T, u and the angle ($\Delta\phi$) between the recoil direction and the lepton direction, together with $\sigma(u_\perp)$ as a function of u, are shown in figure 6.24.

	data	simulation
$W \to e\nu$	-0.53 ± 0.02	-0.52
$W \to \mu\nu$	-0.48 ± 0.02	-0.48

Table 6.16: *Mean $u_{||}$, in GeV, for data and simulation.*

6.6.5 Recoil simulation uncertainty

Although the correlation between the parameters used to simulate u_1 ($P_{1,..,5}$) and those used to simulate u_2 ($P_{6,7}$) is negligible, there is strong correlation between the u_1 response parameters ($P_{1,2,3}$) and between the individual resolution parameters ($P_{4,5}$ and $P_{6,7}$). Consequently, the systematic uncertainty on Γ_W is evaluated by sampling the recoil parameter covariance matrix to obtain 250 sets of recoil parameters. The corresponding distribution of Γ_W values, shown in figure 6.25 for $m_T^{\text{fit}} = 90$ GeV, is obtained by fitting the multiple m_T distributions, simulated using the 250 sets of recoil parameters, to pseudo-data simulated using the default recoil parameters shown in table 6.17. The width of the best fit Gaussian distribution is taken as the uncertainty on Γ_W.

151

$m_{\mathrm{T}}^{\mathrm{fit}}$	W $\to$ eν	W $\to$ $\mu\nu$
80	60	53
85	59	51
90	54	49
100	38	30
110	19	14

Table 6.17: *Systematic uncertainties, in MeV, from the recoil simulation.*
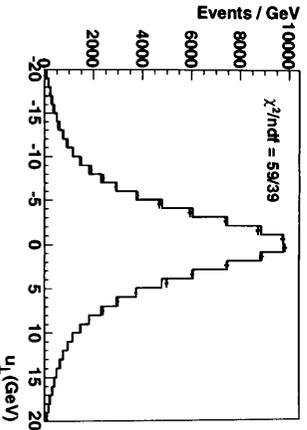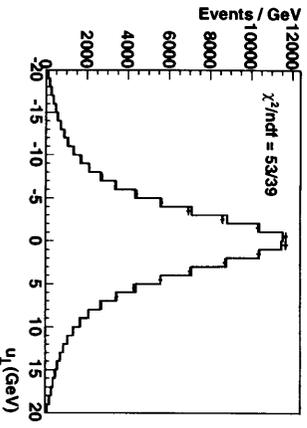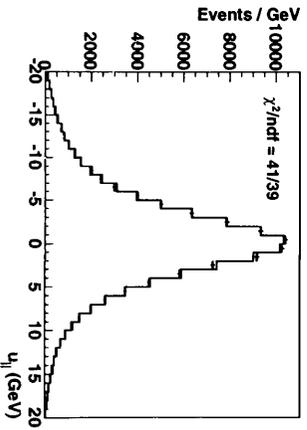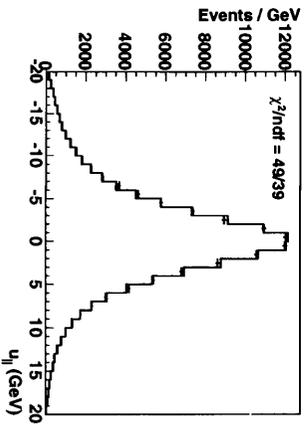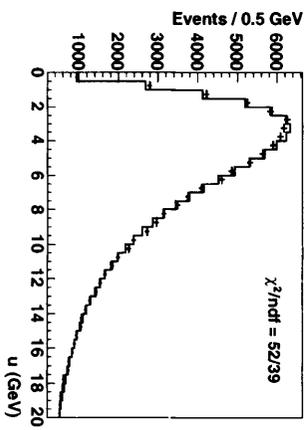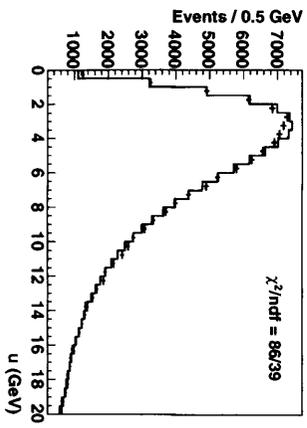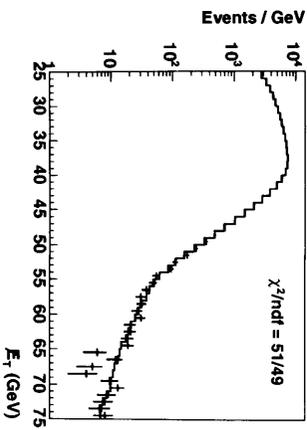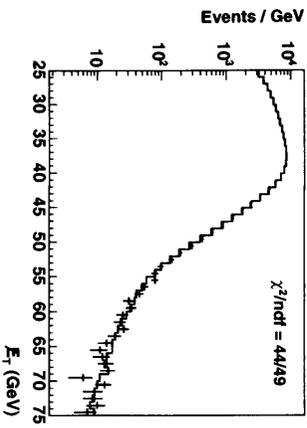
Figure 6.23: The $\not{E}_T$, u, $u_{\parallel}$ and $u_\perp$ distributions (rows 1-4 respectively) for for simulated and candidate (left) $W \to e\nu$ and (right) $W \to \mu\nu$ events.

153
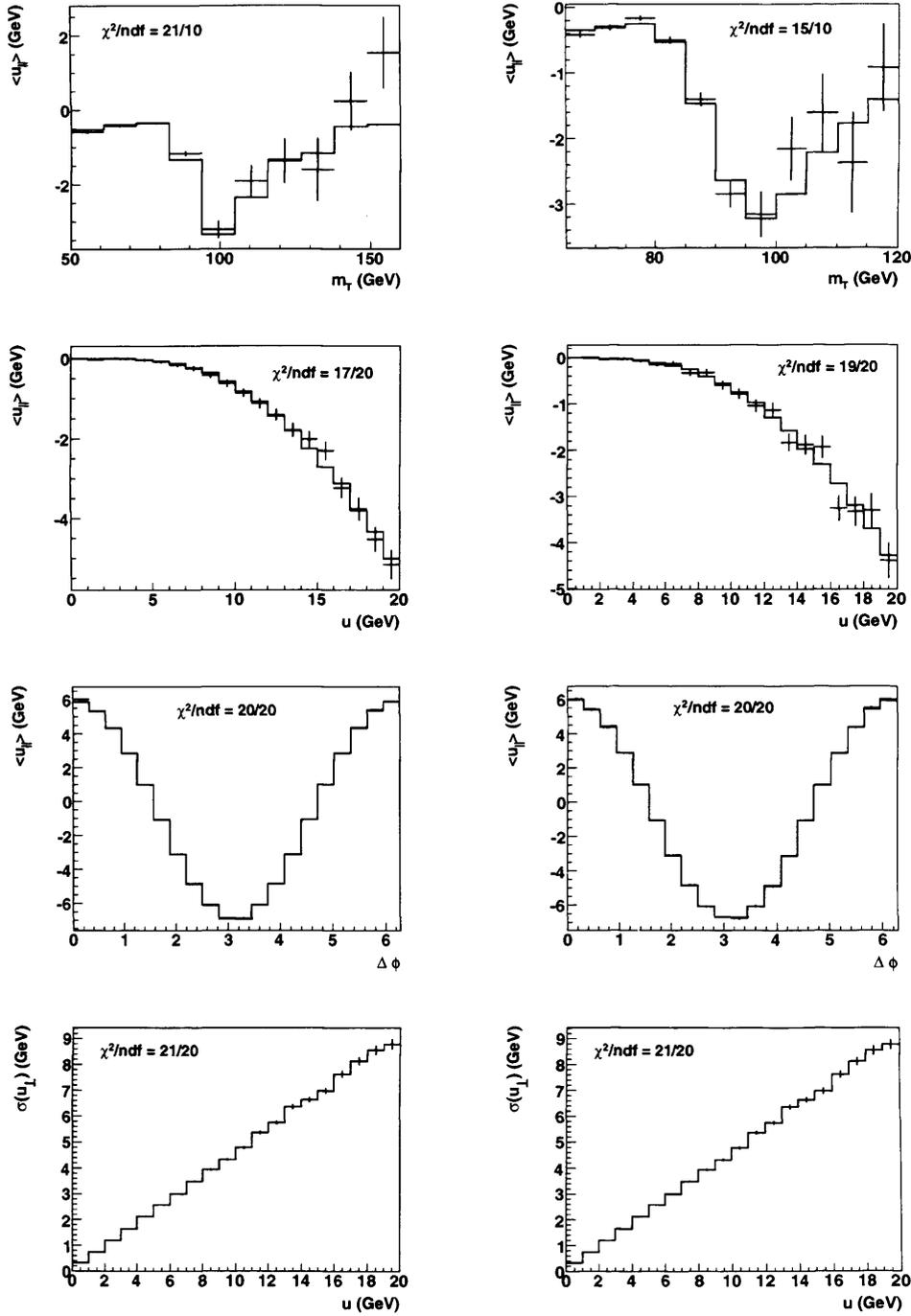
Figure 6.24: *Comparison of* $\langle u_{\parallel} \rangle$ *as a function of* m_T, u, *and* $\Delta\phi$ *(rows 1-3 respectively) and* $\sigma(u_{\perp})$ *as a function of* u *(row 4) for simulated and candidate (left)* $W \to e\nu$ *and (right)* $W \to \mu\nu$ *events.*

154
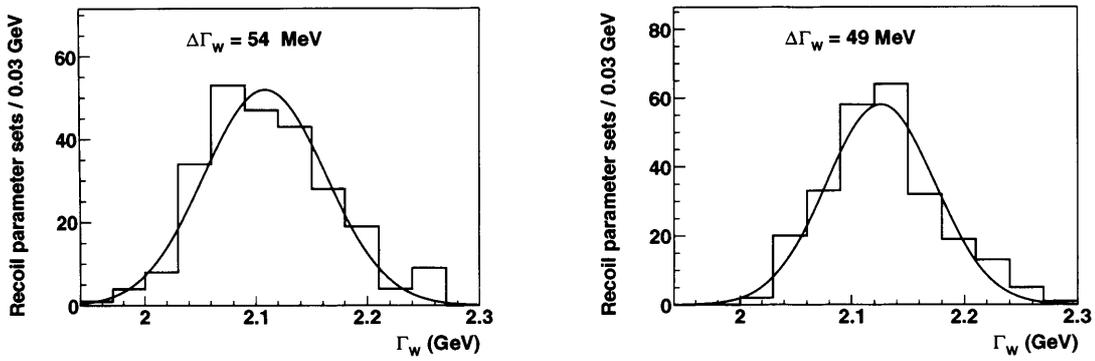
Figure 6.25: *Values of* Γ_W *obtained from sampling the recoil parameter covariance matrix for to obtain the recoil parameter values for (left)* $W \rightarrow e\nu$ *and (right)* $W \rightarrow \mu\nu$ *events and fitting to pseudo-data simulated using the default recoil parameter values.*

Chapter 7

Background events simulation

Candidate W boson events have significant 'background' event contributions from other electroweak and non-electroweak processes which affect the m_T distribution and subsequently the measurement of Γ_W. This chapter describes the determination of the event fraction and m_T distribution of background events relevant to this analysis, and the evaluation of their associated systematic uncertainty. The background event m_T distributions, normalised using the background fraction, are added to the simulated m_T distribution, described in chapter 6.

When describing the background event processes, leptons are not explicitly differentiated from antileptons. Also, neutrino flavours are not explicitly given and are implied by the context. When the charged lepton flavour is not indicated, the electron and muon are implied and, depending on the context, the tau lepton also.

7.1 Electroweak background events

The electroweak background events for $W \to e\nu$ candidate events are $W \to \tau\nu$ and $Z/\gamma^* \to \tau\tau$ events, where a τ decays to $e\nu\nu$, and $Z/\gamma^* \to ee$, events where one of the electrons is not identified. Similarly, the electroweak background events for $W \to \mu\nu$ candidate events are $W \to \tau\nu$ and $Z/\gamma^* \to \tau\tau$ events, where a τ decays to $\mu\nu\nu$, and $Z/\gamma^* \to \mu\mu$, events where one of the muons is not identified. The background and signal ($W \to e\nu$ and $W \to \mu\nu$) processes are simulated using CdfSim. The background fraction is obtained from the ratio of background to signal events passing the W event selection, described in chapter 4.

7.1.1 $W \to \tau\nu$ background

The $W \to \tau\nu$ background event fractions, shown in table 7.1, are obtained using events simulated with both CdfSim and the 'standard' simulation, described in chapters 5 and 6. The combined values are used, and the associated uncertainty on Γ_W is obtained from the change in Γ_W when varying the background fraction by its associated uncertainty. It is found to be negligible in both cases.

	$W \to e\nu$	$W \to \mu\nu$
CdfSim	2.04 ± 0.01	1.98 ± 0.01
standard	2.01	1.98
combined	2.04 ± 0.03	1.98 ± 0.01

Table 7.1: *The* $W \to \tau\nu$ *background event fraction in percent.*

The background m_T distributions are taken from the standard simulation, shown in figure 7.1, as they have more events than CdfSim. The systematic uncertainty from the shape is obtained from the change in Γ_W between using the m_T distri-

bution from `CdfSim` and the standard simulation. It is found to be negligible for
$W \to \mu\nu$ events and has the values shown in table 7.2 for $W \to e\nu$ events.
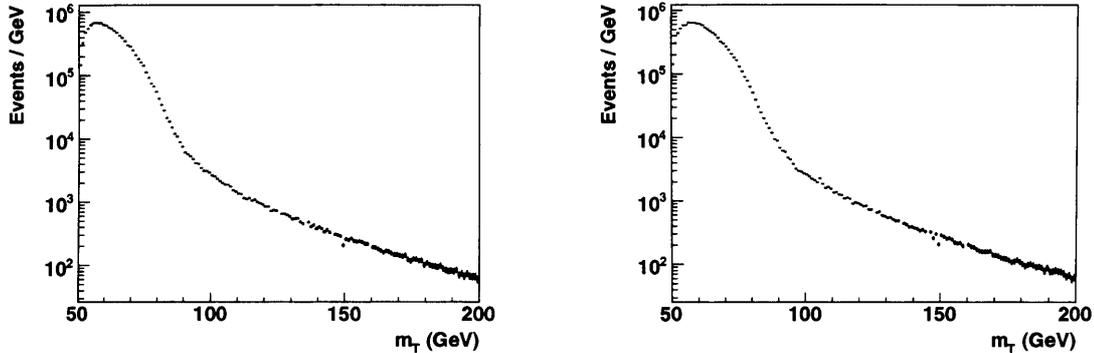
Figure 7.1: *The m_T distributions of* $W \to \tau\nu$ *background events in (left)* $W \to e\nu$
and (right) $W \to \mu\nu$ *events simulated using the standard simulation.*

m_T^{fit}	
80, 85, 90	3
100	5
110	8

Table 7.2: *Systematic uncertainties, in MeV, from* $W \to \tau\nu$ *background events in*
$W \to e\nu$ *candidate events.*

7.1.2 $Z/\gamma^* \to \ell\ell$ background events

The $Z/\gamma^* \to \ell\ell$ background event fractions, where the lepton is an electron, muon
or tau lepton, are obtained from the acceptance ratio of $Z/\gamma^* \to \ell\ell$ to signal
$W \to \ell\nu$ events, generated in equal numbers, divided by the cross-section ra-
tio $R = \sigma(W \to \ell\nu)/\sigma(Z/\gamma^* \to \ell\ell)$. Since the cross-section ratio for Z/γ^* pro-
duction is the same as that for pure Z production in the region $66 < m_{Z/\gamma^*}$
< 116, the numerator of the background fraction only includes events gen-
erated in this region. This allows the use of the NNLO cross-section ratio

158

$\sigma(\mathrm{W} \to \ell\nu)/\sigma(\mathrm{Z} \to \ell\ell) = 10.67 \pm 0.15$ [62].

W boson events with an additional reconstructed track are rejected (Z veto events described in section 4.5). Since CdfSim has a higher tracking efficiency than candidate events in the region $|\eta| > 1$, the number of Z veto events excluded from the signal W boson events is over-estimated. A scale factor of

$$S^{\mathrm{veto}} = \begin{cases} 0.166 \pm 0.013 & \text{for} \quad r_{\mathrm{cot}} < 83\,\mathrm{cm} \\ 0.754 + (0.0017 \pm 0.0006) \times r_{\mathrm{cot}} & \text{for } 83 < r_{\mathrm{cot}} < 132\,\mathrm{cm} \end{cases} \tag{7.1}$$

determined from data is applied to the number of Z veto events.

The $\mathrm{Z}/\gamma^* \to \ell\ell$ background event fractions are shown in table 7.3, with subscripts R and S^{veto} to denote the uncertainty associated with the cross-section ratio and CdfSim Z veto scale factor respectively.

$\mathrm{W} \to e\nu$	
$\mathrm{Z}/\gamma^* \to ee$	$0.167 \pm 0.002_R \pm 0.002_{\mathrm{stat}} \pm 0.005_{S^{\mathrm{veto}}}$
$\mathrm{Z}/\gamma^* \to \tau\tau$	$0.115 \pm 0.002_R \pm 0.001_{\mathrm{stat}}$
$\mathrm{W} \to \mu\nu$	
$\mathrm{Z}/\gamma^* \to \mu\mu$	$5.66 \pm 0.08_R \pm 0.02_{\mathrm{stat}} \pm 0.18_{S^{\mathrm{veto}}}$
$\mathrm{Z}/\gamma^* \to \tau\tau$	$0.123 \pm 0.001_R \pm 0.001_{\mathrm{stat}}$

Table 7.3: *The $\mathrm{Z}/\gamma^* \to \ell\ell$ background event fraction in percent.*

The $\mathrm{Z}/\gamma^* \to \ell\ell$ background event m_{T} distributions are obtained from CdfSim events generated for $m_{\mathrm{Z}/\gamma^*} > 20$ GeV, shown in figure 7.2. Due to the low number of events in the high m_{T} region, the m_{T} distributions are parameterised as a Gaussian function in the low m_{T} region, except for $\mathrm{Z}/\gamma^* \to \mu\mu$ which is sampled from the distribution, and a Landau function in the high m_{T} region,

with the regions defined in table 7.4.
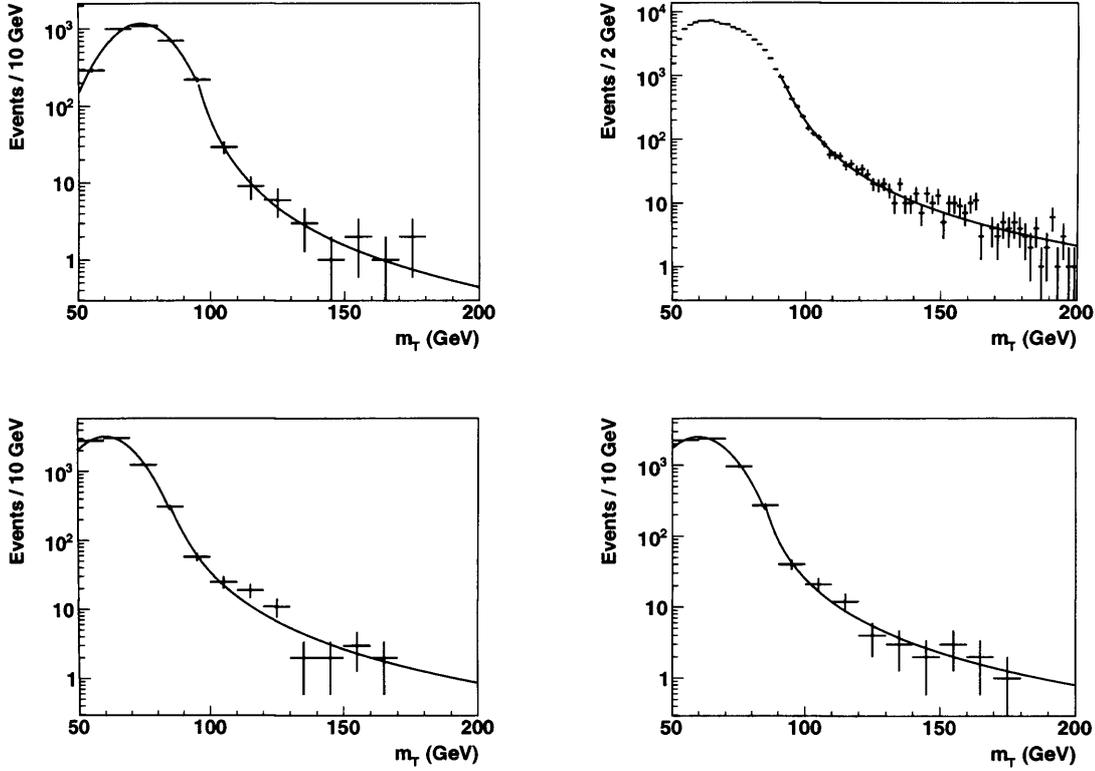
Figure 7.2: *The fitted* m_{T} *distributions of (top left)* $Z/\gamma^* \to ee$, *(top right)* $Z/\gamma^* \to \mu\mu$ *and (bottom)* $Z/\gamma^* \to \tau\tau$ *background events in (left)* $W \to e\nu$ *and (right)* $W \to \mu\nu$ *events.*

	Gaussian	Landau
	$W \to e\nu$	
$Z/\gamma^* \to ee$	$50 < m_{\mathrm{T}} < 95$	$95 < m_{\mathrm{T}} < 200$
$Z/\gamma^* \to \tau\tau$	$50 < m_{\mathrm{T}} < 83$	$83 < m_{\mathrm{T}} < 200$
	$W \to \mu\nu$	
$Z/\gamma^* \to \mu\mu$	none	$90 < m_{\mathrm{T}} < 200$
$Z/\gamma^* \to \tau\tau$	$50 < m_{\mathrm{T}} < 85$	$85 < m_{\mathrm{T}} < 200$

Table 7.4: *Parameterisation of the* $Z/\gamma^* \to \ell\ell$ *background event* m_{T} *distribution, with the associated* m_{T} *regions in GeV.*

The systematic uncertainty from the $Z/\gamma^* \to \ell\ell$ background event fraction is esti-

mated as the change in Γ_W from varying the background fraction by its combined uncertainty, and is found to be negligible for all cases except for the $Z \to \mu\mu$ background fraction in $W \to \mu\nu$ events, which has the values shown in table 7.5. The systematic uncertainty from the shape is obtained by varying the fit parameters by their uncertainty, and is found to be negligible in all cases.

m_T^{fit}	
80	16
85	17
90	14
100	5
110	3

Table 7.5: *Systematic uncertainties for* $W \to \mu\nu$ *events, in MeV, from* $Z \to \mu\mu$ *background events.*

7.2   Decay-in-flight background events

Charged pions and kaons from the hard collision decay into $\mu\nu$. Due to their lifetimes, these decays can occur in the COT. Although the p_T of muons from pion and kaon decays are usually much lower than that of muons from $W \to \mu\nu$ events, the 'kink' in the track from the decay in the COT can result in a fake high p_T measurement, and subsequently a large $\not{E}_T$ measurement. As the $\mu\nu$ branching ratio is large (63.4% for kaons and 99.99% for pions) they contribute a significant background to $W \to \mu\nu$ events.

Due to the kink in the meson-muon track, the track has a different $\chi^2_{\mathrm{track}}/\mathrm{ndf}$ distribution compared to true $W \to \mu\nu$ muons, with a larger average value. The 'decay-in-flight' background event fraction is found by fitting the $\chi^2_{\mathrm{track}}/\mathrm{ndf}$ distribution of true $W \to \mu\nu$ muons added to decay-in-flight muons, to that of $W \to \mu\nu$

candidate muons. The amount of background is varied to minimise the χ^2 of the fit. The background fraction is found separately for tracks with and without hits in the silicon tracker. The χ^2_{track}/ndf distribution of true W $\rightarrow \mu\nu$ muons is taken from Z $\rightarrow \mu\mu$ events, which have a negligible level of background. Since the decay-in-flight muons tend to have a large d_0 distribution, a sample of decay-in-flight muons is obtained by removing the χ^2_{track}/ndf requirement and requiring $0.15 < |d_0| < 1.25$ cm for tracks with hits in the silicon tracker ($0.25 < |d_0| < 1.25$ without silicon hits). The upper d_0 limit is required to provide a sample of decay-in-flight muons with χ^2_{track}/ndf independent of d_0, shown in figure 7.3, since the χ^2_{track}/ndf distribution as a function of d_0 is not consistent with flat above this value.
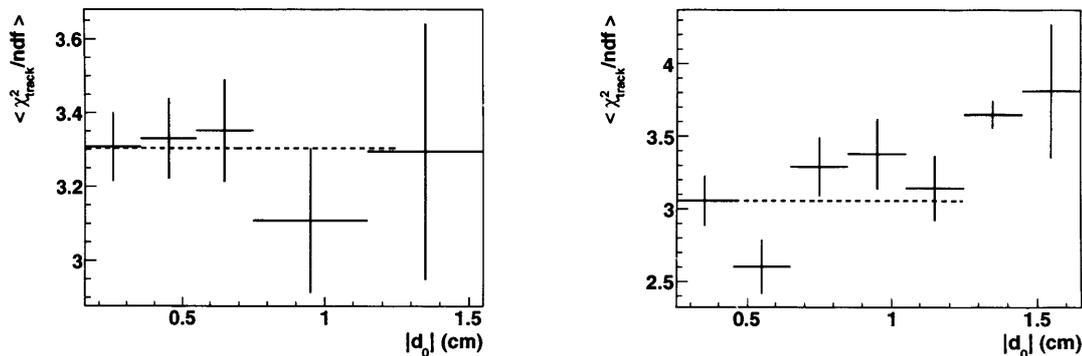
Figure 7.3: *The χ^2_{track}/ndf distributions as a function of $|d_0|$ for decay-in-flight muons for tracks (left) with silicon hits and (right) without. The dashed line delineates the decay-in-flight $|d_0|$ range and its $< \chi^2_{\text{track}}$/ndf $>$ value.*

The background fraction fits to the χ^2_{track}/ndf of W $\rightarrow \mu\nu$ candidate events, shown in figure 7.4, gives a background fraction of (0.113±0.047)% for tracks with silicon hits, and (0.46 ± 0.17)% without silicon hits. Since 6.2% of W $\rightarrow \mu\nu$ candidate events do not have tracks with silicon hits, and the other backgrounds comprise 8.045%, the total decay-in-flight background is (0.146 ± 0.049)%.
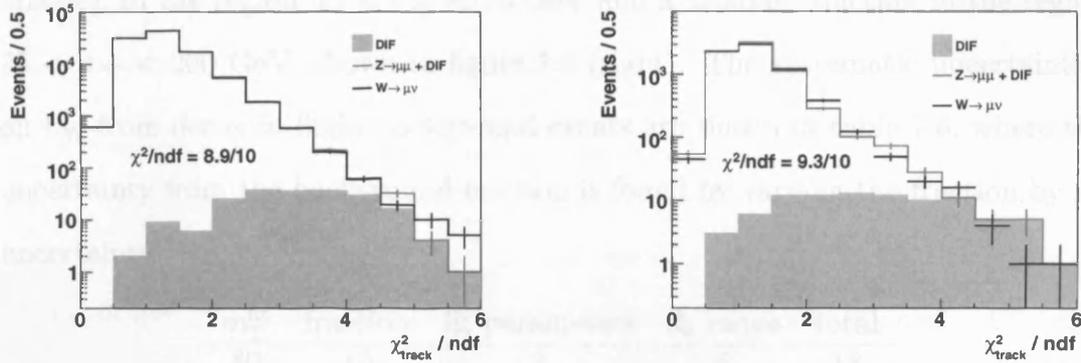
Figure 7.4: *The* Z $\to \mu\mu$ *plus decay-in-flight (DIF) track* $\chi^2_{\text{track}}/$ndf *distribution fitted to* W $\to \mu\nu$ *candidate event, for tracks (left) with silicon hits and (right) without, to obtain the background fraction.*

The decay-in-flight m_T distribution, shown in figure 7.5 (left), is parameterised as a Landau distribution, and obtained from W $\to \mu\nu$ candidate events without the Δx_{cmu}, Δx_{cmp} and Δx_{cmx} requirements and with $0.25 < |d_0| < 0.6$ cm.
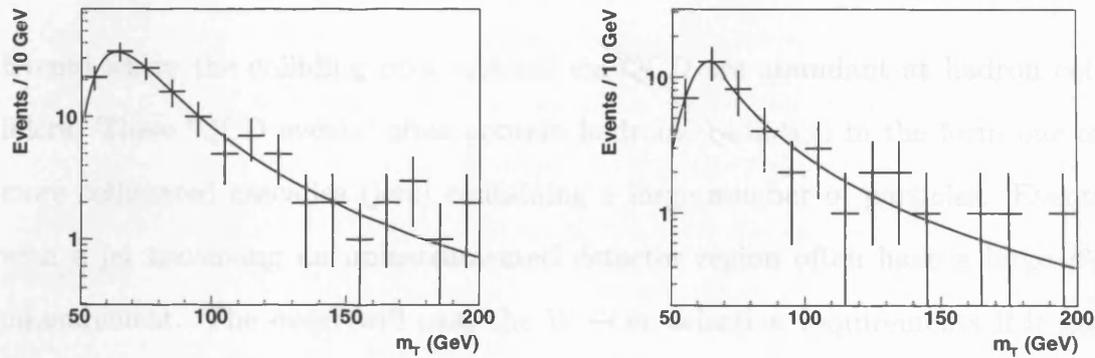
Figure 7.5: *The decay-in-flight* m_T *distribution obtained from* W $\to \mu\nu$ *candidate events using (left)* $0.25 < |d_0| < 0.6$ *cm and (right)* $0.6 < |d_0| < 1.2$ *cm.*

The systematic uncertainty from the shape is obtained from the change in Γ_W when varying the fit parameters by their uncertainty, and also by using a m_T distribution obtained with $0.6 < |d_0| < 1.2$ cm, parameterised as a Gaussian

163

function in the region $50 < m_T < 75$ GeV and a Landau function in the region $75 < m_T < 200$ GeV, shown in figure 7.5 (right). The systematic uncertainties on Γ_W from decay-in-flight background events are shown in table 7.6, where the uncertainty from the background fraction is found by varying the fraction by its uncertainty.

m_T^{fit}	fraction	fit parameters	d_0 range	total
80	15	8	6	18
85	18	9	10	22
90	21	10	13	27
100	29	15	23	40
110	38	20	37	57

Table 7.6: *Systematic uncertainties, in MeV, from decay-in-flight background events in* W $\to \mu\nu$ *candidate events.*

7.3 QCD background events

Events where the colliding $p\bar{p}$'s interact via QCD are abundant at hadron colliders. These 'QCD events' often contain hadronic radiation in the form one or more collimated cascades (jets) containing a large number of particles. Events with a jet traversing an uninstrumented detector region often have a large $\not{E}_T$ measurement. The event will pass the W $\to$ eν selection requirements if it has sufficient $\not{E}_T$, and a jet containing a charged pion meeting the electron track requirements, and a neutral pion that decays into photons meeting the calorimeter requirements. Additionally, kaons and B mesons, from heavy quark radiation, may decay semi-leptonically with a eν or $\mu\nu$ in the final state that passes the W boson selection requirements. Since QCD events are common, they contribute a significant background to W $\to$ eν candidate events.

The QCD background fraction is estimated by fitting the $\not{E}_T$ distribution of QCD events, added to true $W \to \ell\nu$ and electroweak background events, to that of $W \to \ell\nu$ candidate events, without the $\not{E}_T$ and m_T requirements. The amount of QCD background is varied to minimise the χ^2 of the fit, performed in the region $5 < m_T < 60$ GeV. The QCD background fraction is obtained from the number of events remaining after the $\not{E}_T$ requirement is applied. The $\not{E}_T$ distributions of true $W \to \ell\nu$ events and electroweak background events are obtained from the standard simulation and CdfSim respectively. QCD events are obtained from data.

7.3.1 $W \to \mu\nu$ QCD background events

Since true $W \to \mu\nu$ muons have low levels of proximate calorimeter and track activity, QCD muons are obtained using the muon selection requirements, described in section 4.2, without the E_{had} and E_{em} requirements, and the W boson selection requirements, described in section 4.5. The track isolation requirement is reversed to only select muons with other tracks nearby. This 'anti-isolation' requirement is fulfilled by muon tracks that fail the track isolation requirement of $\sum^{\Delta R < 0.4} p_T < 5$ GeV. Decay-in-flight background events are reduced by requiring the muon track to have hits in the silicon tracker.

The $\not{E}_T$ distribution of QCD events is corrected for $W \to \mu\nu$, $W \to \tau\nu$ and $Z \to \mu\mu$ contamination, with their fractions and $\not{E}_T$ distributions obtained from CdfSim. The overall electroweak contamination fraction is obtained from the $W \to \mu\nu$ acceptance ratio of CdfSim to candidate events, using the standard selection requirements and correcting for the other background events. The $\not{E}_T$ distribution of anti-isolation muons before and after correcting for electroweak

and decay-in-flight contamination is shown in figure 7.6 (left) for an anti-isolation value of 4 GeV ($\sum^{\Delta R<0.4} p_T > 4$ GeV).

Since the QCD background in $Z \to \mu\mu$ candidate events is negligible, the number of accepted $Z \to \mu\mu$ events in CdfSim and data, after requiring an anti-isolation muon, should be equal. The fractional deviation and its associated uncertainty is taken as the uncertainty on the electroweak background fraction in anti-isolation events.

The QCD background fraction is obtained by fitting the $\not{E}_T$ distribution of simulated $W \to \mu\nu$ events, with QCD, electroweak and decay-in-flight background events added, to the $\not{E}_T$ distribution of $W \to \mu\nu$ candidate events.
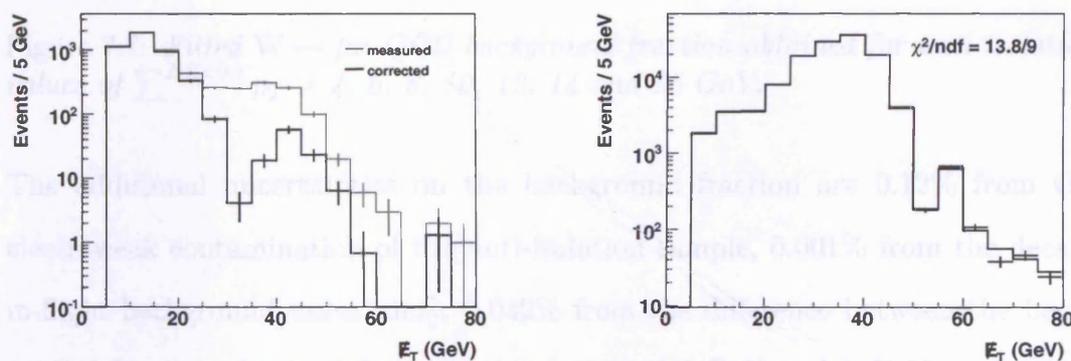
Figure 7.6: *The $\not{E}_T$ distribution of (left) the anti-isolation sample before and after the subtraction of electroweak and decay-in-flight contamination and (right) $W \to \mu\nu$ candidate events fitted with simulated events added to background events.*

Since $\not{E}_T$ and anti-isolation may be correlated in QCD events, the background fraction is determined for QCD event samples obtained with anti-isolation values of $\sum^{\Delta R<0.4} p_T > 4$, 6, 8, 10, 12, 14 and 16 GeV, shown in figure 7.7. The uncertainty for each anti-isolation value is the combined uncertainty of the fit to the $\not{E}_T$ distribution, and the electroweak contamination uncertainty. The mini-

mum of the fitted quadratic function occurs at an anti-isolation value of 4 GeV. A background fraction of $(0.294 \pm 0.008_{\text{fit}})\%$ is obtained from the fit to the $\not{E}_T$ distribution using an anti-isolation of 4 GeV, shown in figure 7.6 (right), and is taken as the QCD background fraction in W $\to \mu\nu$ events.
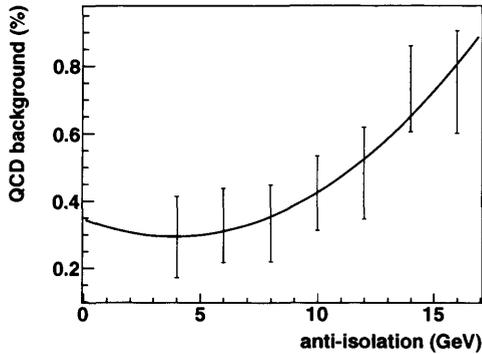
Figure 7.7: *Fitted* W $\to \mu\nu$ *QCD background fraction obtained for anti-isolation values of* $\sum^{\Delta R < 0.4} p_T >$ *4, 6, 8, 10, 12, 14 and 16 GeV.*

The additional uncertainties on the background fraction are 0.12% from the electroweak contamination of the anti-isolation sample, 0.001% from the decay-in-flight background uncertainty, 0.042% from the difference between the background fraction obtained for an anti-isolation of 4 GeV and 8 GeV, and 0.02% from comparing CdfSim with the standard simulation for the $\not{E}_T$ distribution of true W $\to \mu\nu$ events. An additional uncertainty on the background fraction of 0.06%, from removing the $m_T > 50$ GeV, is estimated as the subsequent fractional increase in the number of W $\to \mu\nu$ candidate events. The uncertainties are combined to give a QCD background fraction of $(0.29 \pm 0.13)\%$.

The QCD m_T distribution, shown in figure 7.10 for an anti-isolation of 4 GeV, is corrected for electroweak and decay-in-flight contamination and parameterised as a Gaussian function in the region $50 < m_T < 90$ GeV and a Landau function

167

in the region $90 < m_T < 200$ GeV.
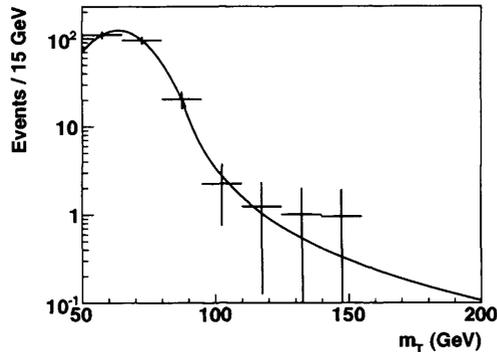
Figure 7.8: *The fitted QCD m_T distribution obtained with an anti-isolation requirement of 4 GeV.*

The uncertainty on Γ_W from QCD background events in $W \to \mu\nu$ candidate events, shown in table 7.7, is estimated as the change in Γ_W from varying the background fraction by its uncertainty, and the shape of the m_T distribution. The parameterised shape of the m_T distribution is varied by each fit parameters' uncertainty, the electroweak contamination uncertainty and the anti-isolation value.

m_T^{fit}	fraction	fit parameters	anti-isolation	EWK	total
80	3	5	3	3	7
85	3	5	5	3	8
90	4	5	10	2	12
100	7	7	13	3	17
110	9	9	16	4	21

Table 7.7: *Systematic uncertainties for $W \to \mu\nu$ events, in MeV, from QCD background events.*

7.3.2 $W \to e\nu$ QCD background events

Since true $W \to e\nu$ electrons have low levels of proximate hadronic calorimeter activity, QCD electrons are obtained using the electron selection require-

ments, described in section 4.1, without the E/p requirement and with the E_{had}/E_{em} requirement modified to $E_{had}/E_{em} < 0.125$. To reduce non QCD electron background events, such as true $W \rightarrow e\nu$ events, three 'anti-electron' subsets are obtained using the following anti-electron requirements; $E_{had}/E_{em} > 0.07$, $|\Delta z| > 0.5$ cm and $\chi^2_{strip} > 10$, where χ^2_{strip} is the comparison of the shape of the charge distribution in the 11 CES cluster strips to test beam data, taking the total cluster energy into account. The 'standard' anti-electron sample is obtained by requiring two of the three anti-electron requirements. The 'E_{had}/E_{em}' and 'χ^2_{strip}' anti-electron samples are obtained by demanding only the E_{had}/E_{em} or χ^2_{strip} anti-electron requirement respectively (the sample obtained by demanding only the Δz anti-electron requirement contains too few events to be meaningful).

The $\not{E}_T$ distributions of the anti-electron samples are corrected for $W \rightarrow e\nu$, $W \rightarrow \tau\nu$, $Z \rightarrow ee$ and $Z \rightarrow \tau\tau$ contamination, with their fractions and $\not{E}_T$ distributions obtained from CdfSim. The overall electroweak contamination fraction is obtained from the $W \rightarrow e\nu$ acceptance ratio of CdfSim and candidate events, using the standard selection requirements and corrected for other background events. A further correction is applied to the $W \rightarrow e\nu$ and $Z \rightarrow ee$ contamination fraction, and accounts for the difference in the ratios of anti-electrons to candidate electrons. This ratio is obtained from $Z \rightarrow ee$ events in CdfSim and data, which has negligible QCD background, and is shown in table 7.8.

anti-electron	R^{data}	R^{cdfsim}	R^{data}/R^{cdfsim}
Standard	$(0.17 \pm 0.05)\%$	$(0.068 \pm 0.009)\%$	2.50 ± 1.25
E_{had}/E_{em}	$(1.20 \pm 0.11)\%$	$(2.32 \pm 0.05)\%$	0.52 ± 0.05
χ^2_{strip}	$(4.66 \pm 0.28)\%$	$(2.88 \pm 0.06)\%$	1.62 ± 0.10

Table 7.8: *The ratio of anti-electrons to standard electrons in data (R^{data}) and CdfSim (R^{cdfsim}) and the ratio of the two (R^{data}/R^{cdfsim}).*

Since the contamination from $W \rightarrow \tau\nu$ and $Z \rightarrow \tau\tau$ events is predominantly from

hadronic τ decay, the anti-electron ratio correction is not applied. The W $\to \tau\nu$ and Z $\to \tau\tau$ contamination fraction uncertainty is taken as twice the uncertainty on the anti-electron ratio correction. The $\not{E}_T$ distribution of anti-electrons before and after correcting for electroweak contamination is shown in figure 7.9 (left).

The QCD background fraction is obtained by fitting the $\not{E}_T$ distribution of simulated W $\to$ eν events, with QCD and electroweak background events added, to the $\not{E}_T$ distribution of W $\to$ eν candidate events, shown in figure 7.9 (right) using standard anti-electrons as the QCD electron sample.
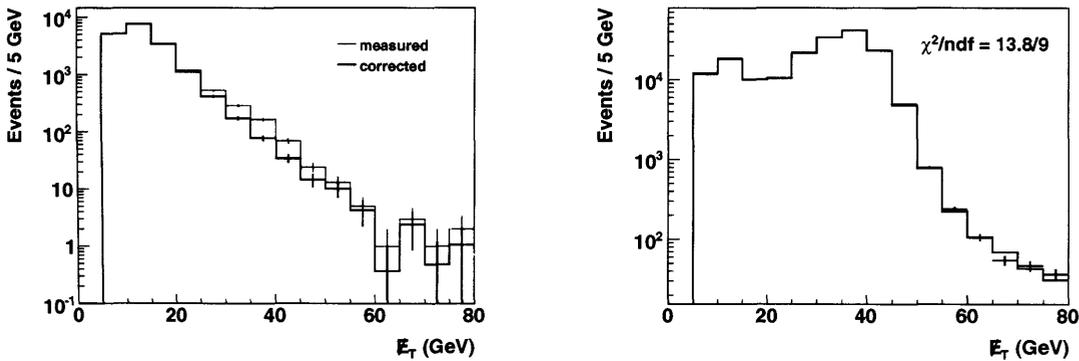
Figure 7.9: *The $\not{E}_T$ distribution of (left) the standard anti-electron sample before and after the subtraction of the electroweak contamination and (right)* W $\to$ eν *candidate events fitted with simulated events added to background events.*

The QCD background fractions obtained for the three anti-electron samples are shown in figure 7.9 together with the uncertainty from the fit and the electroweak contamination.

The uncertainty on the QCD background fraction from the anti-electron definition is taken as 0.22%, which is the greatest difference between the two extreme central values. The additional uncertainties on the QCD background fraction are 0.01% from using CdfSim for the 'true' $\not{E}_T$ distribution instead of the standard

anti-electron	background fraction
Standard	$1.35 \pm 0.01_{\mathrm{fit}} \pm 0.17_{\mathrm{ewk}}$
$E_{\mathrm{had}}/E_{\mathrm{em}}$	$1.49 \pm 0.01_{\mathrm{fit}} \pm 0.14_{\mathrm{ewk}}$
χ^2_{strip}	$1.13 \pm 0.01_{\mathrm{fit}} \pm 0.17_{\mathrm{ewk}}$

Table 7.9: *The QCD electron background event background fraction, in percent, obtained using the different anti-electron definitions.*

simulation, and 0.05% from removing the m_{T} requirement of 50 GeV, estimated as the subsequent fractional increase in the number of W $\rightarrow \mu\nu$ candidate events. The standard anti-isolation sample is used to obtain the QCD background event fraction in W $\rightarrow$ eν events, and the uncertainties are combined to give a background fraction of $(1.35 \pm 0.28)\%$.

The QCD m_{T} distribution, shown in figure 7.10, is obtained from the standard anti-electron sample with the additional requirement of $E/p < 3$, since QCD events in the E/p tail have a different m_{T} distribution. The m_{T} distribution is corrected for electroweak contamination, and fitted with a Gaussian function in the region $50 < m_{\mathrm{T}} < 70$ GeV and a Landau function in the region $70 < m_{\mathrm{T}} < 200$ GeV.
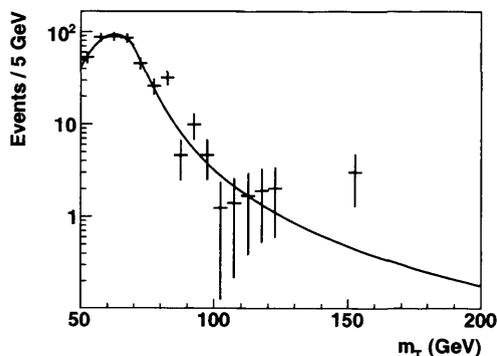
Figure 7.10: *The fitted W $\rightarrow$ eν multi-jet m_{T} distribution obtained with two of $E_{\mathrm{had}}/E_{\mathrm{em}} > 0.07$, $|\Delta z| > 0.5$ cm and $\chi^2_{\mathrm{strip}} > 10$ requirements.*

The uncertainty on Γ_W from QCD background events in $W \to e\nu$ candidate events, shown in table 7.10, is estimated as the change in Γ_W from varying the background fraction by its uncertainty and the shape of the m_T distribution. The parameterised shape is varied by each fit parameters' uncertainty, the electroweak contamination uncertainty and the anti-electron definition. In addition to the three anti-electron definitions described above, the standard anti-electron sample with the additional E/p requirement of candidate electrons ($E/p < 1.3$) is used to evaluate the shape uncertainty.

m_T^{fit}	fraction	fit parameters	EWK	anti-electron	total
80	11	14	5	25	31
85	11	14	5	25	31
90	15	16	6	22	32
100	22	21	12	25	41
110	26	27	10	30	49

Table 7.10: *Systematic uncertainties for* $W \to e\nu$, *in MeV, from QCD background events.*

Chapter 8

Results

The value for Γ_W is extracted from the m_T distribution of W $\rightarrow$ eν and W $\rightarrow$ $\mu\nu$ candidate events, described in chapter 4, by varying the Γ_W input value for the event generator, described in chapter 5, and minimising the negative binned log likelihood [63] of the simulated m_T distribution, described in chapter 6, added to the background events, described in chapter 7. The simulated m_T distribution is normalised to that of candidate events in the region $50 < m_T < m_T^{\mathrm{fit}}$ GeV and fitted in the region $m_T^{\mathrm{fit}} < m_T < 200$ GeV. The systematic uncertainty associated with the event simulation and background estimation are determined for the region $m_T^{\mathrm{fit}} < m_T < 200$ GeV, for m_T^{fit} values of 80, 85, 90, 100 and 110 GeV. The value of m_T^{fit} used in the measurement of Γ_W is chosen to minimise the combined systematic and statistical uncertainty associated with the fit to the m_T distribution in the region $m_T^{\mathrm{fit}} < m_T < 200$ GeV. The evaluation of m_T^{fit} and the subsequent Γ_W measurement is described below.

8.1 Fit region

The systematic uncertainties associated with the event generation, detector simulation and background event estimation are summarised in table 8.1.

m_T^{fit}	W → eν					W → μν				
	80	85	90	100	110	80	85	90	100	110
PDFs	21	22	20	21	26	21	23	20	23	27
electroweak corrections	15	14	10	6	6	4	6	6	6	6
W boson mass	18	17	9	4	2	18	17	9	4	2
energy-loss simulation	13	13	13	13	13	-	-	-	-	-
silicon material scale	3	3	2	1	0	-	-	-	-	-
electron E_T selection	13	13	10	8	8	-	-	-	-	-
lepton $u_{\|\|}$ selection	2	2	2	1	0	7	7	6	2	1
lepton η and ϕ selection	3	3	3	3	3	4	4	4	5	5
electroweak background	3	3	3	5	8	16	17	14	5	3
QCD background	31	31	32	41	49	7	8	12	17	21
decay-in-flight background	-	-	-	-	-	18	22	27	40	57
COT scale	-	-	-	-	-	29	27	17	8	5
COT global resolution	-	-	-	-	-	29	27	21	11	5
COT resolution distribution	-	-	-	-	-	17	17	16	13	10
calorimeter scale	29	27	17	7	4	-	-	-	-	-
calorimeter resolution	46	43	31	11	4	-	-	-	-	-
calorimeter non-linearity	12	13	12	10	6	-	-	-	-	-
recoil	60	59	54	38	19	53	51	49	30	14
W boson p_T	8	8	7	7	6	8	8	7	7	6
total	96	93	79	65	62	80	78	71	62	70

Table 8.1: *Summary of all systematic uncertainties, in MeV.*

Table 8.2 shows the total systematic uncertainty, the statistical uncertainty obtained from the negative binned log likelihood fit, and their combined uncertainty. The value of $m_T^{fit}=$ 90 GeV gives the lowest combined uncertainty for both W → eν and W → μν events, and is used to obtain the value of Γ_W.

The total number of background events in W → eν and W → μν and the number in the fit region 90 < m_T < 200 GeV, are shown in table 8.3 with their m_T distributions shown in figure 8.1.

$m_{\rm T}^{\rm fit}$	W → eν			W → μν		
	systematic	statistical	total	systematic	statistical	total
80	96	54	110	80	60	100
85	93	54	107	78	61	99
90	79	60	99	71	67	98
100	65	78	101	62	90	109
110	62	103	120	70	116	135

Table 8.2: *Combined systematic and statistical uncertainties, in MeV.*

$m_{\rm T}$ region	W → μν		W → eν	
	total	fit	total	fit
all events	108808	2619	127432	3426
W → τν	2021	17	2557	21
Z → ℓℓ	6003	216	205	17
Z → ττ	115	2	151	3
QCD	291	10	1680	99
decay-in-flight	145	40		

Table 8.3: *The number of background events in* W → μν *and* W → eν *candidate events.*
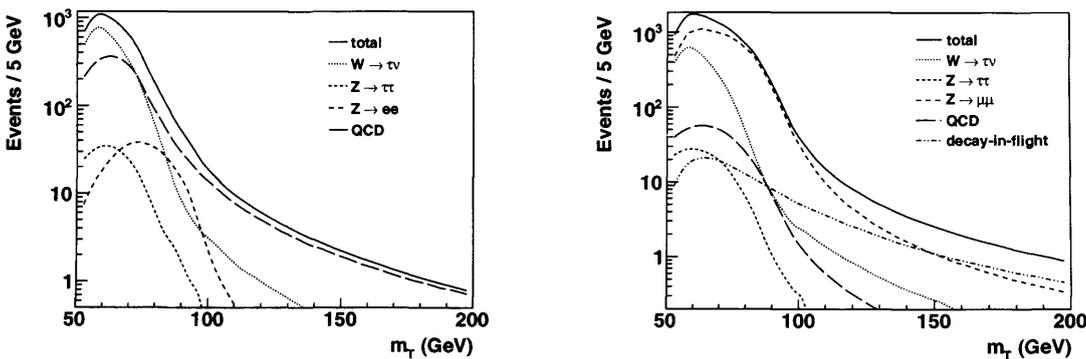
Figure 8.1: *The* $m_{\rm T}$ *distribution of background events for (left)* W → eν *and (right)* W → μν *events.*

8.2 Fit results

The simulated $m_{\rm T}$ distribution is normalised to that of W → eν and W → μν candidate events in the region $50 < m_{\rm T} < 90$ GeV and fitted in the region

$90 < m_T < 200$ GeV. The negative binned log likelihood fit, shown in figure 8.2, gives

$$\Gamma_W = 2118 \pm 60_{\text{stat}} \pm 71_{\text{sys}} \text{ MeV} \tag{8.1}$$

and

$$\Gamma_W = 1948 \pm 67_{\text{stat}} \pm 79_{\text{sys}} \text{ MeV} \tag{8.2}$$

for $W \to e\nu$ and $W \to \mu\nu$ candidate events respectively.
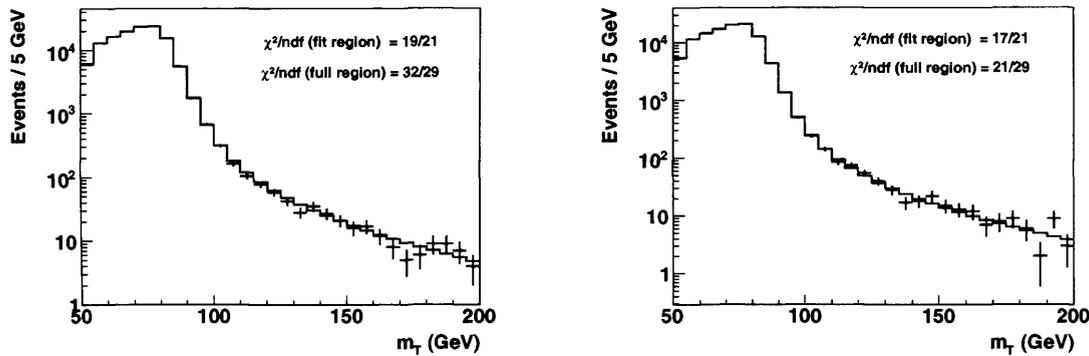
Figure 8.2: *The m_T distribtion of (left) $W \to e\nu$ and (right) $W \to \mu\nu$ candidate events fitted to obtain Γ_W.*

Although separate measurements of Γ_W are made from $W \to e\nu$ and $W \to \mu\nu$ candidate events, the systematic uncertainties associated with the event generation described in chapter 5 are correlated. Biases in the estimate of the combined value result if the two measurements are combined using the weighted average. Instead, the results are combined using the Best-Linear-Unbiased-Estimator (BLUE) method [64], with the correlations of the systematic uncertainties between the decay channels shown in table 8.4.

	W → eν	W → μν	correlation
lepton E_T or p_T scale	21	17	12
lepton E_T or p_T resolution	30	26	
electron energy loss simulation	13		
recoil model	54	49	
W boson p_T	7	7	7
backgrounds	32	33	
PDFs	20	20	20
W boson mass	9	9	9
electroweak corrections	10	6	6
lepton selection	10	7	
total systematic	79	71	27
statistical	60	67	
total combined	99	98	27

Table 8.4: *Summary of uncertainties, in MeV, evaluated for $m_T^{fit} = 90$ GeV for W → μν and W → eν events, together with their correlations between decay channels.*

This gives a combined result of

$$\Gamma_W = 2033 \pm 73 \text{ MeV} \tag{8.3}$$

which is in good agreement with the theoretical prediction of 2093 ± 2 MeV presented in section 1.3.1, and the world average of 2147 ± 60 MeV [25], with the measurement presented in this thesis excluded.

8.3 Related measurements

8.3.1 W boson lifetime

From equation 1.23, the proper lifetime of the W boson is determined to be

$$\tau_W = 3.24 \pm 0.11 \times 10^{-25} \text{ s} \tag{8.4}$$

where the reduced Plank constant $\hbar = 6.582 \times 10^{-16}$ eV·s.

8.3.2   CKM matrix unitarity

The total W boson decay width is the sum of the partial decay widths to leptons
and quarks, described in section 1.3.1, and can be expressed as

$$\Gamma_{\mathrm{W}} = \Gamma(W \to l\nu) \left(3 + 3(1 + \delta^{\mathrm{QCD}}) \sum_{\mathrm{no\ top}} |V_{ij}|^2 \right) \tag{8.5}$$

where the sum is over $i = $ u, c and $j = $ d, s, b. This assumes 3 generations of
fermions. The W boson decay width measurement can therefore be used to test
the unitarity of the CKM matrix, described in section 1.1.4, giving

$$\sum_{\mathrm{no\ top}} |V_{ij}|^2 = 1.91 \pm 0.10 \tag{8.6}$$

using the values for $\Gamma(W \to l\nu)$ and δ^{QCD} presented in section 1.3.1. This is
consistent with the unitarity requirement of 2, and the LEP2 value of $\Sigma |V_{ij}|^2 =$
1.993 ± 0.025 obtained from the LEP2 measurement of the branching ratio of
$Br(W \to l\nu) = (10.84 \pm 0.09)\%$ [25].

8.4   Conclusion

A direct measurement of the W boson decay width is obtained with a precision
of 3.6% by fitting the transverse mass distribution of W $\to$ eν and W $\to$ $\mu\nu$ can-
didate events with an integrated luminosity of 350 pb^{-1}. The measurement of
2033 ± 73 MeV is obtained by combining the separate measurements from the

$W \rightarrow e\nu$ and $W \rightarrow \mu\nu$ decay channels, accounting for correlated systematic uncertainties.

This measurement is currently the best single direct W boson decay width measurement. This measurement is in good agreement with the theoretical prediction of 2093 ± 2 MeV presented in section 1.3.1, and the previous world average of 2147 ± 60 MeV [25]. Combining this measurement with other direct measurements gives a current world average of 2098 ± 48 MeV [21]. In addition, this measurement is also in agreement with the indirect measurement of 2079 ± 41 MeV [26], described in section 1.3.2.

The measurements of the W boson decay width, both direct and indirect, demonstrate the consistency of the standard model, although the constraint on the theoretical prediction of Γ_W from the uncertainty on the m_W measurement is not tested at the current precision of Γ_W measurements.

Bibliography

[1] S. L. Glashow. Partial-symmetries of weak interactions. *Nucl. Phys.*, 22:579, 1961.

[2] S. Weinberg. A Model of Leptons. *Phys. Rev. Lett.*, 19:1264, 1967.

[3] A. Salam and J. Strathdee. A Renormalizable Gauge Model of Lepton Interactions. *Nuovo Cimento*, 11A:397, 1972.

[4] R. Keith Ellis, W. J. Stirling, and B. R. Webber. QCD and Collider Physics. *Cambridge University Press*, 1996.

[5] R. Brandelik, W. Braunschweig, K. Gather, and V. Kadansky. Evidence for planar events in e^+ e^- annihilation at high energies. *Phys. Lett. B*, 86:243, 1979.

[6] G. Arnison *et al.* Experimental observation of isolated large transverse energy electrons with associated missing energy at $\sqrt{s} = 540$ GeV. *Phys. Lett. B*, 122:103, 1983.

[7] M. Banner *et al.* Observation of single isolated electrons of high transverse momentum in events with missing transverse energy at the CERN $p\bar{p}$ collider. *Phys. Lett.*, B122:476, 1983.

[8] G. Arnison *et al.* Experimental observation of lepton pairs of invariant mass around 95 GeV/c^2 at the CERN SPS collider. *Phys. Lett. B*, 126:398, 1983.

[9] P. Bagnaia *et al.* Evidence for $Z^0 \rightarrow e^+e^-$ at the CERN $\bar{p}p$ collider. *Phys. Lett. B*, 129:130, 1983.

[10] D. G. Michael *et al.* Observation of Muon Neutrino Disappearance with the MINOS Detectors in the NuMI Neutrino Beam. *Phys. Rev. Lett.*, 97:191801, 2006.

[11] P. Higgs. Broken Symmetries and the Masses of Gauge Bosons. *Phys. Rev. Lett.*, 13:508, 1964.

[12] Throughout this thesis energy is expressed in electronvolts (eV), the energy gained by an electron accelerated across an electric potential of one volt. Momentum and mass are also expressed in units of energy by defining $\hbar = c = 1$ where $\hbar$ is the reduced Plank constant and c is the velocity of light *in vacuo*.

[13] A. Abulencia *et al.* Search for W' boson decaying to electron-neutrino pairs in $p\bar{p}$ collisions at $\sqrt{s} = 1.96$ TeV. *Phys. Rev. D*, 75:091101, 2007.

[14] CDF collaborations. A Combination of CDF and DØ Results on the Mass of the Top Quark. arXiv:0803.1683, 2008.

[15] F. Halzin and A. Martin. Quarks and Leptons. *Wiley*, 1984.

[16] L. Ryder. Quantum Field Theory. *Cambridge University Press*, 1996.

[17] A.D. Martin, R.G. Roberts, W.J. Stirling, and R.S. Thorne. Parton distributions: a new global analysis. *Eur. Phys. J. C.*, 4:463, 1998.

[18] U. Baur and D. Zeppenfeld. Finite Width Effects and Gauge Invariance in Radiative W Production and Decay. *Phys. Rev. Lett.*, 75:1002, 1995.

[19] J. L. Rosner and M. P. Worah. Oblique corrections to the W Width. *Phys. Rev. D*, 49:1363, 1994.

[20] W. M. Yao *et al.* Review of Particle Physics. *J. Phys. G*, 33, 2006.

[21] Tevatron Electroweak Working Group. Combination of CDF and D0 results on the W boson mass and width. *arXiv:0808.0147v1*, 2008.

[22] C. Albajar *et al.* Studies of intermediate vector boson production and decay in UA1 at the CERN proton-antiproton collider. *Z. Phys.*, C44:15, 1989.

[23] T. Affolder *et al.* Direct Measurement of the W Boson Width in $p\bar{p}$ Collisions at $\sqrt{s} = 1.8$ TeV. *Phys. Rev. Lett.*, 85, 2000.

[24] V. Abazov *et al.* Direct measurement of the W boson decay width. *Phys. Rev. D*, 66:32008, 2002.

[25] The LEP Collaborations. A Combination of Preliminary Electroweak Measurements and Constraints on the Standard Model. arXiv:hep-ex/0612034v2, 2007.

[26] D. Acosta *et al.* First Measurements of Inclusive W and Z Cross Sections from Run II of the Fermilab Tevatron Collider. *Phys. Rev. Lett.*, 94:091803, 2005.

[27] The CDF Collaboration. The CDF II Detector Technical Design Report. *FERMILAB-Pub-96/390-E*, 1996.

[28] A Abulencia *et al.* Observation of $B_s^0 - \overline{B_s^0}$ Oscillations. *Phys. Rev. Lett.*, 97:242003, 2006.

[29] R. Gilmor. Single Particle Detection and Measurement. *Taylor & Francis*, 1992.

[30] S. Cabrera, J. Fernández, G. Gomez, and J. Piedra. The CDF-II time-of-flight detector. *Nuclear Inst. and Meth. A*, 494:416, 2002.

[31] D. Acosta, S. Klimenko, J. Konigsberg, and A. Korytov. The CDF Cherenkov luminosity monitor. *Nuclear Inst. and Meth. A*, 485:249, 2001.

[32] K. Goulianos, M. Gallinaro, K. Hatakeyama, and S. Lami. The CDF Mini-Plug calorimeters at the Tevatron. *Nuclear Inst. and Meth. A*, 518:42, 2004.

[33] T. Nelson. The CDF-II silicon tracking system. *Nuclear Inst. and Meth. A*, 485:381, 2002.

[34] T. Affolder, D. Allspach, D. Ambrose, and J. Bialek. CDF Central Outer Tracker. *Nuclear Inst. and Meth. A*, 526:249, 2004.

[35] To describe the detector, the cylindrical coordinate system (θ,ϕ,z) is used with the origin at the nominal interaction point and the z axis pointing along the beampipe in the proton direction. The azimuthal angle ϕ lies in the xy plane and is measured upwards from the z axis.

[36] L. Balka *et al.* The CDF central electromagnetic calorimeter. *Nuclear Inst. and Meth. A*, 267:272, 1988.

[37] A. Bhatti *et al.* Determination of the jet energy scale at CDF. *Nuclear Inst. and Meth. A*, 566:375, 2006.

[38] S. Bertolucci *et al.* The CDF central and endwall hadron calorimeter. *Nuclear Inst. and Meth. A*, 267:301, 1988.

[39] G. Gomez-Ceballos *et al.* Event Builder and Level 3 at the CDF experiment. *Nuclear Inst. and Meth. A*, 518:522, 2004.

[40] A. Baranovski, D. Benjamin, G. Cooper, and S. Farrington. CDF II Production Farm Project. *Nuclear Inst. and Meth. A*, 572:399, 2007.

[41] A. Abulencia *et al.* The CDF II extremely fast tracker upgrade. *Nuclear Inst. and Meth. A*, 572:249, 2007.

[42] The standard CDF 'good run' requires all the necessary detector subsystems and the data acquision and logging systems to be fully operational.

[43] Alan Beaulieu. Learning sql. *O'Reilly Media, Inc*, 2005.

[44] F. Abe *et al.* Measurement of the ratio $\sigma B(p\bar{p} \to W \to e\nu)/\sigma B(p\bar{p} \to Z^0 \to ee)$ in $p\bar{p}$ collisions at $\sqrt{s} = 1800$ GeV. *Phys. Rev. D*, 52:2624, 1995.

[45] J. Pumplin, D.R. Stump, J. Huston, H.L. Lai, P. Nadolsky, and W.K. Tung. New generation of parton distributions with uncertainties from global QCD analysis. *JHEP*, 207:12, 2002.

[46] F. A. Berends and R. Kleiss. Hard photon effects in W and Z decay. *Z. Phys.*, 27:365, 1985.

[47] F. A. Berends, R. Kleiss, J. P. Revol, and J. P. Vialle. QED radiative corrections and radiative decays of the intermediate weak bosons produced in proton-antiproton collisions. *Z. Phys.*, 27:1155, 1985.

[48] E. Barberio, B. van Eijik, and Z. Was. Photos - a universal Monte Carlo for QED radiative corrections in decays. *Comput. Phys. Comm.*, 66:115, 1991.

[49] E. Barberio and Z. Was. Photos - a universal Monte Carlo for QED radiative corrections: version 2.0. *Comput. Phys. Comm.*, 79:291, 1994.

[50] U. Baur and D. Wackeroth. Electroweak radiative corrections to $p\bar{p} \rightarrow W^{\pm} \rightarrow l^{\pm}\nu$ beyond the pole approximation. *Phys. Rev. D*, 70:073015, 2004.

[51] F. Abe *et al.* First Measurement of the W-Boson Mass in Run II of the Tevatron. *Phys. Rev. Lett.*, 99:151801, 2007.

[52] J. Collins, D. Soper, and G. Sterman. Transverse momentum distribution in Drell-Yan pair and W and Z boson production. *Nucl. Phys. B*, 250:199, 1985.

[53] F. Landry, R. Brock, P. Nadolsky, and C. Yuan. Fermilab Tevatron run-1 Z boson data and the Collins-Soper-Sterman resummation formalism. *Phys. Rev. D*, 50:4239, 2003.

[54] W. Giele and S. Keller. Determination of W-boson properties at hadron colliders. *Phys. Rev. D*, 57:4433, 1998.

[55] P. Arnold and R. Kauffman. W and Z production at next-to-leading order: From large q_T to small. *Nucl. Phys. B*, 349:381, 1991.

[56] A.D. Martin, R.G. Roberts, and W.J. Stirling. Parton Distributions: a Study of the New HERA Data, α_s, the Gluon and $\bar{p}p$ Jet Production. *Phys. Lett. B*, 4:419, 1996.

[57] GEANT 3 Detector Description and Simulation Tool. *CERN Program Library Long Writeup W5013*, 1993.

[58] M. Paulini E. Gerchtein. CDF detector simulation framework and performance. arXiv:physics/0306031v1, 2003.

[59] A. B. Migdal. Bremsstrahlung and Pair Production in Condensed Media at High Energies. *Phys. Rev*, 103:1811, 1956.

[60] J. H. Hubbell *et al.* Atomic form factors, incoherent scattering functions, and photon scattering cross sections. *Int. J. Appl. Radiat. Isol*, 4:471, 1975.

[61] F. Abe *et al.* First run II measurement of the W boson mass at the Fermilab Tevatron. *Phys. Rev. D*, 77:112001, 2008.

[62] W. L. van Neerven and E. B. Zijlstra. The $O(\alpha_s^2)$ corrected Drell-Yan K-factor in the DIS and $\overline{MS}$ schemes. *Nucl. Phys. B*, 382:11, 2002.

[63] L. Lyons. Statistics for nuclear and particle physicists. *Cambridge University Press*, 1986.

[64] P. Clifford L. Lyons, D. Gibaut. How to combine correlated estimates of a single physical quantity. *Nuclear Inst. and Meth. A*, 270:110, 1988.